Effects of Borehole Stability on Well Log Data

by

Samantha Grandi Karam

Submitted to the Department of Earth Atmospheric and Planetary Sciences
in partial fulfillment of the requirements for the degree of

Master of Science

at the

MASSACHUSETTS INSTITUTE OF TECHNOLOGY

[September 2003]
August 2003

Author .....
Department of Earth Atmospheric and Planetary Sciences
August 20, 2003

Certified by .....
M. Nafi Toksöz
Professor
Thesis Supervisor

Accepted by .....
Maria T. Zuber
Head, Department of Earth, Atmospheric & Planetary Sciences

Effects of Borehole Stability on Well Log Data

by

Samantha Grandi Karam

Submitted to the Department of Earth Atmospheric and Planetary Sciences
on August 20, 2003, in partial fulfillment of the
requirements for the degree of
Master of Science

Abstract

In this thesis we analyze the effects of borehole irregularities on well logs and develop methods to obtain reliable formation properties from such logs. Data from a well in eastern Venezuela are analysed. Borehole irregularities in this well consist mainly of borehole enlargements perpendicular to the borehole axis due to rock failure under high horizontal stresses. They are observed in three forms: as small scale irregularities of the borehole wall, as-near elliptical shapes oriented along the minimum in situ stress direction, and as an increase of borehole diameter at all azimuths due to large scale failure. Breakout data suggest that maximum stress is oriented NNW-SSE.

The suite of logs analyzed include lithology, density, dipmeter and full waveform acoustic logs. The standard log processing and interpretation methods fail because of the effects of irregularities. The analysis of the density log indicates that standard corrections are not enough when diameter is severly elongated. Similarly, acoustic logs processed commercially give unreasonable formation velocities. Guided by theoretical models we evaluate the effects of irregularities on different wave types recorded by full waveforms acoustic logs, i.e refracted P and S, pseudo Rayleigh, Stoneley, flexural etc. We obtain P and S wave velocities from the least affected waves. The density profile is derived from P wave data (V_p-ρ correlation), with the aid of lithology logs. From the above parameters we obtain the dynamic elastic moduli and then, through known empirical relationships, the static quantities. These values will be used in the next phase of this study as input to finite element models to determine the magnitude of the in situ stress that caused the borehole failures.

Thesis Supervisor: M. Nafi Toksöz
Title: Professor

Acknowledgments

I would like to thank my advisor, Prof. Nafi Toksöz for his guidance and particularly for his humanity. I appreciate and thank his solidarity when my family and my country went through difficult times.

Franklin Ruíz, my PDVSA advisor and friend, has been an invaluable support, technical and emotional. He provided me with all the important inputs for this work: data, general understanding of the problem and how it fitted in the chain of processes of our industry. I deeply thank him for that, and for reminding me constantly to take vitamins and exercise.

I would like to acknowledge the old Exploration Division of *Petróleos de Venezuela*, PDVSA, for allowing me to use and publish these data, but above all, for believing in me. Besides the privilege of working for almost five years with the tools of excellency, PDVSA granted me with a scholarship to complete this Master.

During the development of this thesis, and in these years, I came across with many people who directly or indirectly helped me complete this work. My sincere thanks to Dr. Rama Rao, for his advise organising this research, to Xiaojun Huang for sharing her knowledge and to Jonathan Kane, my office mate and friend. I would also like to thank Victoria Briggs, Sudipta Sarkar, Dr. Dan Burns, Dr. Randolph Martin, Sue Turbak, Liz Henderson, Carol Sprague and Joe Hankins.

Last but not least I express my gratitute to my two dearest friends: JK and Fabio, without whom I would have simply returned home long time back. Their friendship is the best reward I got after these years at MIT.

I dedicate this work to my mom and family, and to my friends all around the world.

Contents

List of Figures

List of Tables

Chapter 1

Introduction

The issue of wellbore stability has gained particular importance in the last 10 years because of increased hydrocarbon exploration in complex areas. Wellbore stability refers collectively to several possible problems encountered while drilling or producing an oil well. The one addressed in this thesis is related to mechanical rock failure, during or after drilling, due to stress concentrations around the borehole. Conversely, during drawdown, depletion of fluids alters pressures significantly and, depending on the kind of lithology supporting the reservoir, the casing could suffer damage leading to total loss of the wellbore (Frederick et al., 1988). A third problem considered as wellbore instability is sand production.

Severe hole enlargement has a long list of consequences, from reducing the drill bit life to stuck pipe, poor cementing, logging problems and the necesity of sidetracking (Last, 2001). An issue that is commonly underestimated in the oil industry concerns the uncertainties of well log data when the borehole environmental conditions are unusual, as in the presence of wellbore instabilities. Most tool designs and fundamental principles, assume ideal borehole conditions and often the consequences of departures from this normalcy are overlooked or simply unknown. However, the implications are relevant specially in the determination of rock properties, a key aspect in the definition of the exploratory model and later on, in the reservoir characterization.

1.1 Scope and Outline

The objective of this thesis is to evaluate the effects of borehole wall instabilities on well logs thus, in the conventional estimation of rock parameters derived from them. A particular well, hereinafter referred as well M, represents a typical example of a damaged borehole, therefore it provides a convenient set of data, fitting the purpose of this study.

The thesis is divided into 4 chapters. In the rest of this chapter we introduce the problem and review some topics on the stress state in the crust.

Chapter 2 describes some of the well data, processing when needed, and interpretation of the consequences of borehole conditions. This chapter is devoted to some of the standard logging products. It also includes a description of the well geological-tectonical setting.

In Chapter 3 we analyse the more specialized information contained in acoustic logs. Again, the manifestation of the borehole conditions are evaluated. Once the uncertainties on the velocity are pinpointed, the main applications of these data are presented: derivation of formation porosity and density, formation elastic parameters and mechanical rock properties.

Finally, Chapter 4 summarizes the conclusions and further work steming from this thesis.

1.2 Description of the Problem

Well M is a wild-cat drilled on land, in a tectonically complex area of eastern Venezuela. Figure 1-1 shows two caliper measurements (C1 and C2), in a section of this well, recorded by a logging tool. The curves depict the borehole dimension at two perpendicular axes. From the figure, it is clear that the borehole has undergone significant failure below 8500 ft. In some cases, as in 10400 ft, the hole diameter reaches 22.3 inches, almost the double of the bit size (12.25 in).

Below 13000 ft the well has a near constant radius (not shown); rugosities and

caverns are non existent although there are some intervals where the hole is "tight" or diameter is reduced from its nominal (drilled) size (Ruiz and Graterol, 2002). This behaviour is generally associated with formations prone to creep, like salts or shales (Tare and Mody, 2002). We will concentrate on the region above 13000 ft where the main instabilities are characterised by hole enlargements.

When observing the deformations in well M walls, two issues call for attention. The first one is related to the interpretation of the log data and the necessity to correct for borehole size. This aspect constitutes the main objective of the thesis. The second one is related to the cause of the instabilities themselves. Regarding this, we only say that most of the instabilities here are related to stress concentration around the wellbore. Because a detailed analysis of the stress field in the area is out of the scope of this thesis we just review next some basic concepts.

1.3 State of Stress in the Earth

To describe the stress field completely in the Earth we need only to refer to the orientation and magnitudes of the principal stresses (see appendix A). For simplicity we refer to those stresses as S_1, S_2 and S_3:

$$\begin{aligned} S_1 &= (\lambda + 2G)\epsilon_1 + \lambda\epsilon_2 + \lambda\epsilon_3 \\ S_2 &= \lambda\epsilon_1 + (\lambda + 2G)\epsilon_2 + \lambda\epsilon_3 \\ S_3 &= \lambda\epsilon_1 + \lambda\epsilon_2 + (\lambda + 2G)\epsilon_3 \end{aligned} \tag{1.1}$$

where $\lambda = (\mathrm{E}\ \nu)/(1 - 2\ \nu)(1 + \nu)$, G is the shear modulus, E and ν are the Young's modulus and Poisson ratio respectively and ϵ_i are the principal strains.

Within the lithosphere, the principal axes appear to be oriented approximately horizontally and vertically (Zoback and Zoback, 1989). In general, $SHmax$ describes the maximum principal horizontal stress and $Shmin$, the minimun principal horizontal stress. Furthermore, the principal stress that is essentially vertical, Sv, can be described as the stress induced by the weight of the overlying rock.

Anderson's faulting theory (Anderson, 1951) predicts stress magnitudes at depth using criteria of failure based on simplified two-dimensional Mohr-Coulomb circles (see Appendix A). In that work, it is shown that in areas of normal faulting, $Sv \geq SHmax \geq Shmin$; in areas of strike slip faulting, $SHmax \geq Sv \geq Shmin$; and in areas of reverse faulting, $SHmax \geq Shmin \geq Sv$. Therefore, the tectonic environment dictates which kind of faults are more likely, hence, the maximum and minimum stresses.

1.3.1 Stress Concentration around Wells

When a borehole is drillled the initial Earth stress state is perturbed in the near field, normally by increasing the concentration of stresses around the borehole (Zoback, 2001).

Data from wells demostrate that spalled sections of well bores, termed breakouts in the petroleum industry, often occur. In those cases, the average azimuth of the long dimension is very consistent within a given well or oil field (Zoback et al., 1985). Breakouts are the results of localized shear failure around a borehole in response to horizontal compression. Stress-induced breakouts occur naturally and are common at large depths since stress magnitudes increase almost linearly with depth.

Stress-induced failures around a borehole can be explained in terms of the Hoop stress relative to the strength of the rock surrounding the well. The concept of Hoop stress originates in the equations describing the concentration of stresses in a plate with a circular hole under uniform tension at infinity, first derived by G. Kirsch in 1898 (Malvern, 1969). By modifying these equations to include effective minimum and maximum compressive stresses and the fluid pressure in the hole, the stresses around a circular hole in a homogeneous, isotropic elastic medium is given by (Jaeger

and Cook, 1979):

$$\begin{aligned}
\sigma_r &= \frac{1}{2}(SH^* + Sh^*)(1 - \frac{R^2}{r^2}) + \frac{1}{2}(SH^* - Sh^*)(1 - 4\frac{R^2}{r^2} + 3\frac{R^4}{r^4})\cos(2\theta) + \frac{\Delta P R^2}{r^2} \\
\sigma_\theta &= \frac{1}{2}(SH^* + Sh^*)(1 + \frac{R^2}{r^2}) - \frac{1}{2}(SH^* - Sh^*)(1 + 3\frac{R^4}{r^4})\cos(2\theta) - \frac{\Delta P R^2}{r^2} \qquad (1.2) \\
\tau_{r\theta} &= -\frac{1}{2}(SH^* + Sh^*)(1 + 2\frac{R^2}{r^2} - 3\frac{R^4}{r^4})\sin(2\theta)
\end{aligned}$$

where σ_r is the radial stress, σ_θ is the circumferential stress, $\tau_{r\theta}$ is the tangential shear stress, R is the radius of the hole, θ is the azimuth measured from the direction of SH^* and ΔP is the difference between the fluid pressure in the borehole and that in the formation (positive indicates excess pressure in the borehole); SH^* and Sh^* refer to the effective horizontal stresses, that is, the stresses supported by rock and pore fluid ($S^* = S - \alpha P_p$, where α is the Biot constant and P_p is the pore pressure).

Hoop stress, the stress around the hole, is defined by equations 1.2 when $r = R$. Figure 1-2 shows the variation of hoop stress as a function of azimuth for different values of $SHmax$ and $Shmin$ and $\alpha = 1$. Hoop stresses are maximum at 90° and minimun at 0°:

$$\begin{aligned}
\sigma_{0^\circ} &= 3Shmin - SHmax - 2\alpha P_p - \Delta P \\
\sigma_{90^\circ} &= 3SHmax - Shmin - 2\alpha P_p - \Delta P \qquad (1.3)
\end{aligned}$$

In general, failure occurs when the strength of the rock is exceeded by the concentrated stress. For instance, if the rock had a strength $C_0 = 150$ MPa, as shown in figure 1-2, failure around the borehole would be restricted to the angle range $\theta = -45°$ to -90° given $SHmax = 2.2Sv$ and $Shmin = 1.25Sv$. Not to have any failures under this stress field, the rock has to have a compressive strength larger than 250 MPa. On the contrary, if it is as weak as 25 MPa, it will fail at all azimuths. The function σ_θ steepens as the difference between $SHmax$ and $Shmin$ becomes large.

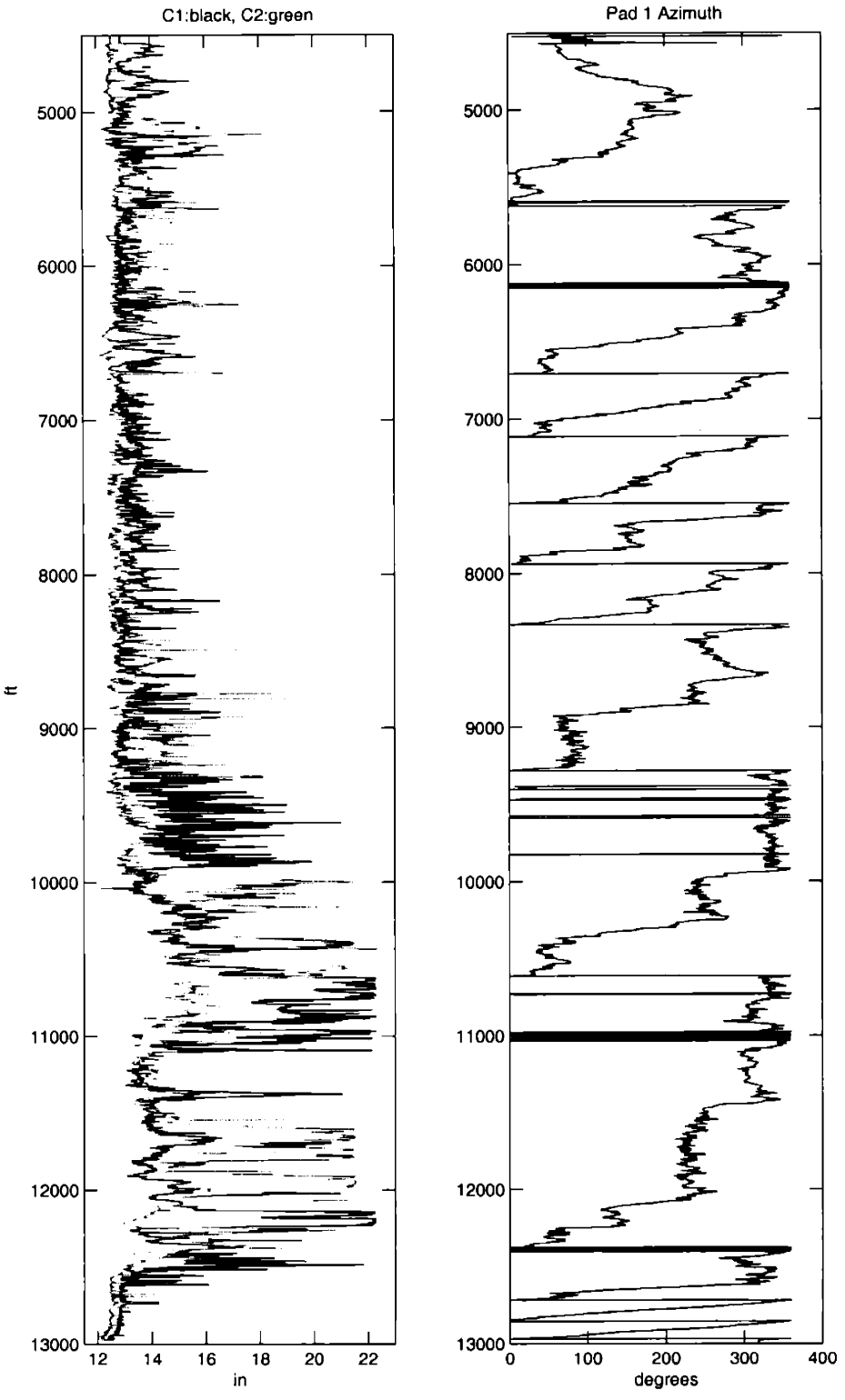

Figure 1-1: Caliper data showing perpendicular hole diameters at every depth level. In the right panel, the orientation of the tool with respect to magnetic north is plotted.

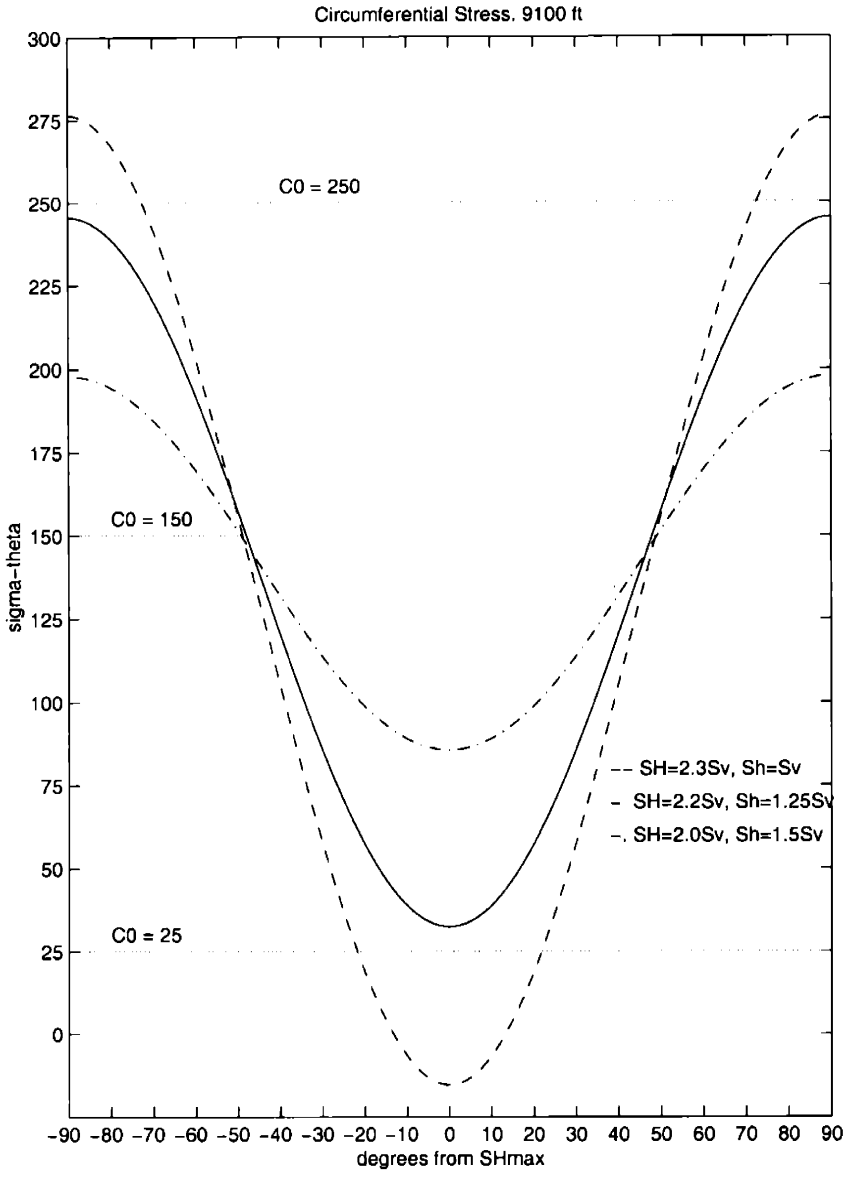

Figure 1-2: Hoop stress as a function of azimuth as described by equations 1.2 when $r = R$, P_p = 27.8 MPa and ΔP = -0.98 MPa. Three cases are shown and for all of them Sv is 56 MPa: (1) $SH = 2.3Sv$, $Sh = Sv$ (dashed line); (2) $SH = 2.2Sv$, $Sh = 1.25Sv$ (solid line); (3) $SH = 2.0Sv$, $Sh = 1.5Sv$ (dash-dotted line). When Hoop stress exceeds the rock mechanical resistance at a particular angle, failures are expected. Because Hoop stress is not constant everywhere around the hole, it is possible that the failures are localized. In this example, when the rock strength is 250 MPa failures only take place for case (1) and at azimuths -70° to -90°. When the rock strength is 150 MPa failures are observed at all cases but still localized between -45° and -90°. For a strength of 25 MPa failures occur at all azimuths for cases (2) and (3).

Chapter 2

Well Data and Formation Description

In this chapter some of the field data are described. The data consist of measurements obtained in a well and supporting geologic information. Well M is located in eastern Venezuela, north of Monagas state, at the foothills of the mountain chain known as "Serrania Oriental del Interior" (fig. 2-1). The area constitutes the north western border of the East Venezuelan Basin. Well data are available in the depth interval 4500 ft to 12989 ft.

The structural geology of the area suggests that the main compressional structures were formed in the late lower Miocene as a consequence of the still active oblique collision of the Caribbean plate and the South American plate. Several faults limit the area; to the north is the overthrust Cerro Corazón, to the south the reverse fault Pirital, to the east the normal fault San Francisco and to the west the system of ramps Urica (fig. 2-1). The main direction of the tectonic movement is towards the south. The structural model is still under discussion mainly in terms of the stress field. Reverse faulting with some strike slip component, seems to be dominant (Report: PEP Macal- Geología Structural, 2001), therefore horizontal stresses are expected to be high close to the N-S direction.

In the area, the expected stratigraphic column consists, from top to base, of

formations[1]: Mesa-Las Piedras, conglomerates and sandstones of age Pliocene to Pleistocene; Morichito, middle Miocene molasic sediments discordant over Querecual (Cretaceous- late Albian to early Coniacian), composed mainly of black calcites; Chimana/El Cantil (Aptian to Cenomanian), sandstones and limestones; and Barranquín (Barremian to early Aptian), that contains quartzites interlayered with shales, where illite is the predominant clay mineral.

Barranquín is normally followed by the Miocene shales of Carapita which are overthrusted by Pirital fault. Below the fault, lies the reservoir rock Naricual (Oligocene) and, after Eocene-Paleocene formations, the second repetition of the cretaceous is usually found. Well M penetrated the normal section, that is, until Barranquín (fig. 2-2). Pirital overthrust was not crossed and several modified models, generated after these findings, suggest that it may be located around 3000 ft below the final depth of well M (18020 ft). On top of that, well M found a different section between 13090 ft and final depth, that has been described as pre-Barranquín. Its age is uncertain by the lack of fossils; it is characterised by an important hematite content and thus the name "unit of red layers" is used (Report: PEP Macal- Estratigrafía, 2001).

Visually, rock cuttings in formation Barranquín present porosities on the order of 10% as a product of fracturing and cement dissolution. They have a high grade of compaction with diagenesis intermediate to intense, while the red layers underneath show intense diagenesis with high cementation and loss of all visual porosity (Report: PEP Macal- Estratigrafía, 2001). Several other characteristics of the formations around well M are next obtained from the log data.

2.1 Lithology

Figure 2-3 shows the gamma ray and density logs together with the maximum and minimum hole axes. Note that the two diameters are perpendicular although they are plotted in the same plane and that they might not be in the same orientation everywhere.

[1]this description is found at http://www.pdvsa.com/lexico/lexicoh.htm

The gamma ray log indicates the natural radioactivity of the formations. Gamma rays are electromagnetic radiations emitted from an atomic nucleous during radioactive decay. These radiations are characterised by frequencies ranging from 10^{19} - 10^{21} Hz (Serra, 1984a). In sedimentary rocks, the log normally reflects the shale content because radioactive elements tend to concentrate in clays. Unless the formation waters contain dissolved radioactive salts or other contaminant as volcanic ash, clean formations usually have low level of radioactivity. The depth of investigation of this log is about 1 ft (Schlumberger, 2002e).

In particular, the Natural Gamma Ray Spectrometry log (NGS[2]), measures the total radioactivity and the separate concentrations of potassium, thorium and uranium which are the elements that emit nearly all the gamma radiation encountered in the Earth. Besides the traditional application of lithology interpretation of the standard gamma ray tool, NGS allows one to differentiate further between shales and potassium salts, recognize mineral types present in the rock and evaluate their percentages, compute a better shale volume, distinguish carbonate series, detect unconformities and sometimes fractures, as well as for sedimentological applications like the recognition of depositional environments and level of diagenesis (Serra, 1984a). The NGS data for well M is presented in figure 2-4.

In general, we can say that rocks in this section must contain a high percentage of quartz in combination with a variable mineralogy. To start, we discard the presence of potassium evaporites or pure carbonates of chemical origin since the thorium concentrations are not negligible anywhere. Additionally, if there are clean sanstones (orthoquartzites), they still exhibit some radioactivity that could be related to mica or feldspars. However, the very low ratio Th/K (not shown), indicates that sandstones do not contain micas. The low concentrations of potassium also indicates that feldspars percentage must be low. If and most likely, there are shaly sandstones, then the concentrations of potassium should be associated with illite, indicating some level of diagenesis. Similarly, if carbonates are present, the concentrations of K and Th indicate that they should contain some clay and/or galuconite.

[2]Mark of Schlumberger

Gamma ray and NGS logging tools are sensitive to hole conditions (hole size, mud weight and composition). Usually the logs are corrected by these factors by means of calibration charts; in large boreholes and in heavy muds, corrections are quite significant when tool is centered (fig. 2-5). The curves shown in figures 2-3 and 2-4 are already corrected. The gamma ray tool used in well M was 3 3/8 inches in diameter and because off-centered, corrections were not significantly large in spite of the great variations of bore diameter. In figure 2-6, the mud weight, the borehole maximum axis and the gamma ray difference are shown for a particular depth range. It can be observed that corrections tend to be large when gamma ray readings are also large, that is, borehole size and mud weight matter more when the rock contains more radioactive minerals.

There are similar corrections for particular mud components as barite and bentonite, that can also alter the gamma ray measurement. Mud used for this section of well M was oil-based, but the actual composition was unavailable for this study. In summary, borehole conditions can significantly affect gamma ray measurements when certain tools are used; in other cases, as in well M, departures from ideal condition are negligible and gamma ray logs are reliable.

2.1.1 Sedimentological information

X-Ray Diffraction (DRX) was also performed in about 100 samples between 1740 ft and 18010 ft; the results are shown in table 2.1 (Report: PEP Macal- Estratigrafía, 2001).

Despite of the low resolution of DRX and large errors in the estimation of depth of cuttings, this analysis is useful, for instance, to distinguish calcium-content rocks from pure silica that have similar gamma ray responses. In addition, the mineralogical analysis provides information on the presence of other minerals, as iron compounds, and classifies further the clay minerals. In well M, below 7000 ft, the main clay is illite while above this depth, minerals like kaolinite, chlorite and smectite are also found in important proportions. The DRX results validate the interpretation of the NGS data.

Table 2.1: X-Ray Diffraction (from cuttings). Mineral weight percentage.

Depth[ft]	Quartz	K-Felds	Pl-Felds	Calcite	Dolomite	Hematite	Siderite	Pyrite	Clay Min.
4660	10	0	0	52	0	0	0	6	32
4850	17	11	0	24	13	0	0	7	28
5060	45	7	0	7	5	0	0	1	35
5260	32	3	0	2	4	0	1	7	50
5460	5	0	0	76	3	0	0	0	16
5660	52	4	1	3	12	0	0	6	23
5750	46	7	5	4	10	0	0	5	23
5800	70	4	1	2	0	0	0	2	20
6000	58	7	1	1	0	0	2	0	31
6200	63	7	2	1	0	0	0	6	21
6400	48	4	3	7	0	0	0	8	30
6600	31	0	1	22	2	0	0	10	30
6800	60	7	0	2	4	0	0	4	23
7000	59	0	1	1	1	0	4	0	34
7200	72	7	0	1	1	0	2	2	15
7400	61	4	1	1	0	0	0	5	28
7600	73	3	1	1	3	0	0	2	17
7800	69	3	1	1	0	0	3	0	23
8000	78	2	1	0	1	0	1	2	15
8200	51	3	1	0	5	0	3	4	33
8400	53	3	1	1	3	0	2	2	33
8500	58	2	2	1	4	0	1	3	29
8580	27	10	1	0	0	17	0	0	45
8700	38	0	3	1	1	0	2	0	45
8800	46	2	2	1	1	0	1	0	47
8900	43	3	2	0	1	0	2	4	45
9000	48	2	2	1	1	0	2	4	40
9100	53	2	3	1	1	0	1	0	39
9210	46	3	2	1	0	0	2	2	44
9310	31	4	1	0	1	0	2	3	58
9460	29	0	1	0	0	12	0	0	58
9560	54	0	2	0	1	0	1	4	38
9700	61	2	3	1	1	0	0	2	30
9900	72	0	2	0	0	0	0	0	26
10100	47	2	0	1	2	0	0	5	43
10300	57	2	0	1	1	0	0	3	36
10400	69	0	4	0	0	0	0	0	27
10600	54	3	4	0	0	0	1	2	37
10800	55	2	2	0	0	0	0	0	41
11000	45	4	3	0	0	0	0	4	44
11200	50	0	2	0	0	0	2	4	42
11400	46	0	2	0	0	0	2	8	42
11600	55	1	1	1	0	0	2	3	37
11750	57	1	0	0	1	0	0	4	37
11850	45	2	1	0	0	0	1	6	45
12050	51	2	2	0	0	0	0	9	37
12250	56	0	0	1	1	0	0	7	35
12450	58	2	2	1	0	0	1	5	31
12650	60	4	2	0	16	0	0	2	16
12850	59	3	2	0	2	0	0	0	35

In the section available, two stratigraphic units are crossed. Chimana/El Cantil goes until 6655 ft, and from here to the end of the section, it is recognised as formation Barranquín. The integrated biostratigraphic and sedimentological information complete the lithological descriptions of these units (Report: PEP Macal- Estratigrafía, 2001):

a. Formation Chimana/El Cantil: cream colored calcites, white sandstones with some glauconite, grey shales, some traces of pyrite and carbon are present everywhere. Sometimes, as above 4740 ft, calcites predominate whereas between 4820 and 5390 ft sandstones are dominant. From 6483 ft to 6655 ft there are abundant blackshales. Calcites have cement, not much of which is dolomitic. The clay minerals are mainly kaolinite, chlorite, illite and mixed illite/smectite. The predominant depositional environment observed is neritic medium.

b. Formation Barranquín: sandstones silicoclastic and calcareous to glauconitic, interlayered with black shales and few calcites. The environment is transitional. The mineralogical composition from DRX shows that illite is the dominant clay mineral. Diagenesis is intense and sandstones present porosity by fracture, cement dissolution and lixiviation of feldspars. Below 8430 ft sandstones are conglomeratic and there are some traces of volcanic rocks and red siltstones.

2.1.2 Shale Volume

Comparing the potassium values in both formations, the significant presence of illite and perhaps feldspars in Barranquín (and their slight presence in Chimana), can also be interpreted from the NGS log (figure 2-7); higher percentages of potassium are in general observed in Barranquín. Thorium bearing rocks, on the other hand, tend to be more abundant in Chimana formation than below which also indicates the detritic predominant lithology of Barranquín.

The concentration of uranium is not a shale indicator, therefore the Computed Gamma Ray (CGR), that is, the gamma ray curve where the radioactivity contribution from uranium has been substracted, was used to compute the shale or clay

volume. For each formation, V_{sh} is approximated as:

$$V_{sh} = (CGR - CGR_{min})/(CGR_{sh} - CGR_{min}) \tag{2.1}$$

where CGR_{min} and CGR_{sh} correspond to the minimum and maximum value of CGR respectively (Serra, 1984a). It is assumed that the maximum value is associated to the rock in the unit with the highest percentage of clay. In the case of well M, Chimana's highest reading is located around 5980 ft while for Barranquín this depth is about 7050 ft. In figure 2-8 the computed shale volume is plotted.

The rapid variability in mineralogy of the formations around well M makes difficult the correlation of the failures observed in the borehole walls with a particular rock type. In general, calcium rich rocks are stiffer than sandstones or shales, therefore they support higher stresses before failing. An example is shown in figure 2-9 where two intervals, whose lithologies are provided by mineralogical analysis, have different mechanical behaviour.

As mentioned before, even limestones in this section contain certain percentage of quartz and/or shale. In general, clay content reduces the rock mechanical resistance, however we observe a correlation in formation Barranquín between less shale volume and borehole instability (fig. 2-10) [3].

2.2 Drilling Logs

Drilling logs did not show any anomalies in Barranquín formation. There were neither circulation losses nor drag effects that could indicate the necessity of changing mud weight. Zones of overpressure common in adjacent areas, were not crossed by this well. On the other hand, it seems that the mud weight could have been too low in this interval. Below 12600 ft the borehole is better preserved and there, the mud weight was increased from about 8.4 to 8.8 lbs/gal. Figure 2-11 depicts these data.

In order to identify any mechanically anomalous interval it is useful to analyse the

[3] this observation is analyzed more extensively in section 3.6.

ROP (Rate Of Perforation) log; fig. 2-12 shows the behaviour from 11000 to 12000 ft. ROP tends to increase from 5 to 10 ft/h in those depths where the borehole is enlarged, indicating that these formations are less compacted.

2.3 Density Log

The density data shown in figure 2-3 come from the dual-spacing litho-density logging (LDT[4]). It is obvious that the density log is very much affected by the borehole conditions since the curve follows the caliper behaviour (fig. 2-13).

In general, density logs use the Compton scattering phenomenum that undergo gamma rays to measure the electron density (ρ_e) of the formation around the well. Gamma rays are emmitted from a radioactive source (Cs^{137}) and as they are scattered, energy is lost. Gamma rays with less energy, are received at the tool detector which emits an electrical pulse and counts each detected ray (Schlumberger, 2002d). The number of counts at this detector is inversely related to the electron density per unit volume of the formation: in high density formations considerable scattering limits the distance gamma rays can travel, therefore only a small number of gamma rays reach the receiver.

The function of the second (short-spacing) detector is to compensate for the effects of mud filtrate and borehole rugosities. When the contact between the tool and the formation is not perfect, the second detector provides a correction, however it has some limitations since the depth of investigation is, depending on the formation density, about 4 inches (Schlumberger, 2002d). The tool is pressed against the borehole wall through a mechanical arm located on the back. The distance between the front tool panel (where source and receivers are located) and the eccentric arm is recorded as a caliper curve.

The true bulk density (ρ_b) is related to the electron density (ρ_e) by a factor that depends on the atomic number of the elements and their atomic weights; since this factor is near unity ρ_b is taken as ρ_e. On the other hand, the formation density depends

[4]Mark of Schlumberger

on porosity and density of the fluids filling the pores. Tools are usually calibrated such that the measured density (apparent, ρ_a), matches that of a freshwater-filled pure limestone (Schlumberger, 2002d):

$$\rho_a = 1.0704\rho_e - 0.1883 \tag{2.2}$$

When formations are liquid-filled sandstones, limestones or dolomites, ρ_a approximates ρ_b. If rocks are gas-bearing, coals, anhidrites or else, further corrections are needed and laboratory calibration charts provide them.

One of the applications of the density logging is to obtain porosity. The relationship between these quantities comes from:

$$\Phi = (\rho_m - \rho_a)/(\rho_m - \rho_f) \tag{2.3}$$

where ρ_m and ρ_f refer to the known matrix density and the fluid density respectively. The matrix density is usually chosen according to the type of formation, environment and other characteristics of the area. Due to the short penetration of this tool into the formation, the fluid in the pores is probably the mud filtrate and usually a density between 0.9 and 1.1 g/cc is assigned to ρ_f.

The bulk density curve shown in figure 2-13 is already corrected by the differences recorded with the short-spacing detector, however, corrections do not seem to be enough to compensate for the hole enlargement. On one hand, the mechanical arm that presses the tool against the borehole wall opens only up to 22 inches. On the other hand, the borehole diameter changes very fast and often in less than 4 ft, which is the source-receiver distance of the tool. Densities at depth of larger caverns are too low, disagreeing with normal expected values for the actual rock types.

Following the previous description of the tool, the density log is unreliable. An alternative procedure to obtain density values from sonic velocities is presented in next chapter.

2.4 Dipmeter Log

The dipmeter log is mainly used to measure the structural dip of bedding planes intersecting the well. In the case of well M, the tool used has four pad-type microinduction sensors arranged in an orthogonal pattern, that measure the variation of formation conductivity. The reference pad, pad 1, is magnetically oriented and two independent calipers measure the borehole diameter between pads 1 and 3 (C1), and pads 2 and 4 (C2). The four-arm dipmeter aligns with the long axis of a non-circular borehole (Schlumberger, 2002c). The tool used in well M is designed particularly for oil-based muds (Oil-Based Dipmeter Tool, OBDT [5]).

Due to the tool rotation as it travels uphole, sometimes the pair 2-4 is the one that aligns with the long axis. This is why the curves in figure 1-1 intersect at some depths. Referred to pad 1, the tool is also measuring the direction with respect to the magnetic north (azimuth) as well as the deviation angle of the hole and orientation of the deviation (relative bearing).

We will use the dipmeter data for three purposes: to determine the structural dip; to localise possible fractured zones; and to identify the instabilities in well M. The failures observed in the dipmeter caliper (breakouts) contain information about the horizontal stresses direction (Zoback, 2001).

2.4.1 Structural Dip

At each of the four pads, one conductivity curve is recorded (fig. 2-14); when the tool crosses a dipping plane the change in resistivity is measured at different depths at each pad. If the orientation of the sonde, the borehole deviation and azimuth are also known, one can compute the apparent dip of the plane cut by the well. Note that this plane could correspond to bed boundaries but also fractures, faults, erosional surfaces or folds; their discrimination is part of a complicated interpretational process (Schlumberger, 2002b).

For the purposes of this work, we would like to know if there is a dominant

[5]Mark of Schlumberger

structural angle and if major features with different orientation are crossing the well. The method we applied is a simplification of the standard dipmeter processing (Serra, 1984a), and is summarized as follows:

1.) We focus on the possible differences between signals of pad 3 and pad 1. These two pads are separated 180° and the distance between them is known at all depths. The reason to choose this pair is that the tool measures orientation data referred to pad 1.

2.) Both signals are scaled to the range -1 to +1.

3.) A correlation window of 20 ft (40 samples) is selected [6].

4.) We shift pad 3 curve, $g(z)$, in steps of one sample, 6 samples on both directions (l), and at each step we compute the correlogram:

$$C = \frac{1}{n\sigma_f\sigma_g}\sum_{i=1}^{n} f(z)g(z+l) \tag{2.4}$$

where n is the number of samples and σ is standard deviation.

5.) We compare the coefficients of this correlogram and observe at which lag it reaches a maximum. The displacement of pad 3 signal that produces this maximum corresponds to the depth difference between the two pads in registering the same 20 ft interval. An example interval where a shift of 1 sample on pad 3 curve gives maximum correlation (0.76) is shown in figure 2-15.

6.) We take the next 40 samples and repeat steps 4 and 5.

7.) For each 100 ft, we compare the lag results of the 5 intervals correlated. Those with correlation coefficient smaller than 0.1 are neglected. The best and most frequent lag within the 100 ft interval is selected. In figure 2-16 a histogram for the whole well section is shown. The two conductivity curves correlate best without any shifting (zero lag) for most of the section. This indicates that bedding should be perpendicular to the borehole. The maximum well inclination (in the section available) is about 4° at 5330 ft but in average, deviation is approximately 1° NW. Layers must then have a dip close to 0°.

[6] in commercial dipmeter processing correlation windows range from 3 to 15 ft (Serra, 1984a)

A second mode was observed at a lag of -1 and a third, less dominant, at +1. We verified if the difference in sign of these secondary events (+1 and -1) was due to the orientation of the tool. At those depths with lag of +1, where the tool was more than 50° rotated respect to near depths of shift -1, a lag of -1 was re-assigned. In such cases, both modes correspond to the same dip azimuth and the occurrences in the previous histogram can be added. The resultant histogram is shown to the right in figure 2-16. The -1-lag occurrences constitute the second most significant mode, this means that pad 3 is registering some "layers" about 0.5 ft deeper than pad 1. This relative displacement could correspond to a regional tectonic trend or some dipping structures crossing the 0° bedding.

To compute the apparent dip of such features, we relocate the depth intervals showing the -1 lags. These are located mainly between 5700 and 6500 ft, 8500-9000 ft and between 10700 and 11000 ft where the average distance between pad 1 and 3 (d_{1-3}) is about 14 in [7], then, $dip = atan(0.5ft/d_{1-3}) \simeq 23°$. Note that this corresponds to an upper limit estimation since best correlation could come from displacements less than 0.5 ft. In fact, Report: PEP Macal- Geología Structural (2001) reports average structural dip of 9° to the SSE.

The apparent azimuth is computed from pad 3 azimuth which is in average 115° at the former depths; the magnetic declination is 10°, then, $azimuth \simeq 125°$ measured from the geographic north. Here we are assuming that the apparent strike coincides with the 1-3 direction, however such assumption is not completely irrational since conductivity curves at pad 2 and 4 are very similar indicating there is no relative displacement between these two points.

In summary, the well is crossing flat layers and there is some structural dip of less than 23° towards the south-east (S55°E).

When analysing dipmeter data care must be taken whether the borehole is badly caved because the pressure of the pads against the wall decreases as the caliper arms are more open. In the extreme case when one or both of the diameters is larger than 21.7 inches (the maximum distance that the tool can open), the dipmeter

[7] rarely the intervals where this dip was registered coincided with zones of failures

resistivity measurements are unreliable. Moreover, at these depths, the dipmeter caliper measurement might not be showing the true hole diameter as illustrated in figure 2-17.

2.4.2 Possible Fractured Zones

The dipmeter can be used as a fracture identification log when non-steeply dipping formations are crossed. When mud filtrate invades a fracture system, it causes a lower microresistivity reading from the pad positioned opposite to the fracture (Schlumberger, 2002c). The former observation is valid when mud is more conductive than the original fluids in the fractures (salty water relative to fresh water or hydrocarbons). In such cases, reported decreases in resistivity can go from about 100 to 10 ohm.m in fractured zones (Serra, 1984b).

Resistivities recorded in well M vary from about 2 to 25 ohm.m. This indicates that formation and mud may not have distinctive conductivities, making it difficult to detect fractures with this technique. In any case, the change of conductivity has to be observed at opposite pads (180° apart), hence, the anomalous zone appears consistently when overlying adjacent pad curves. In addition to this, regions with changes of conductivity, where maximum aperture of the tool is reached, are not reliable and should not be associated to fractures based only on this method (e.g 12100-12400 ft).

The analysis produced the following results: 1.) apart from few localized areas, neither fractures nor other evidences of anisotropic conductivity around the borehole were found, 2.) the characteristics of few possible fractured zones are summarized in table 2.2 and some are shown in figure 2-18, and 3.) in most of these zones, if there are fractures, they are in the direction orthogonal to borehole elongation.

From table 2.2 we can see that only the first interval (5166-5173 ft) presents conductivity anisotropy in the direction where the borehole is elongated. In the other cases, fractures average strike is about N10W-S10E. The results do not imply that these are the only possible fractured or anisotropic regions, but they are the only ones detected with this procedure.

Table 2.2: Possible fractured/anisotropic intervals based on dipmeter conductivity data (approximate values over the intervals). The column "pair" refers to the pads registering increment of conductivity. In all these cases the pair 1-3 is the one aligned with the long axis of the borehole.

Depth[ft]	Pair	Pad 1 az.[deg]	Strike
5166-5173	1-3	160	N10W-S10E
8487-8495	2-4	260	N-S
10025-10035	2-4	250	N10W-S10E
10080-10125	2-4	250	N10W-S10E
10465-10472	2-4	50	N30W-S30E

It has been suggested that increases of hole diameter might respond to crumbling of a fractured zone during drilling due to single or closely spaced steeply dipping fractures (Serra, 1984b). Other authors have found intersecting fractures as a valid explanation (Babcock, 1978). However, all of these mechanisms predict fracture strike aligned with borehole elongation, and according to the dipmeter analysis presented, they could not explain all the failures in well M.

A final aspect concerning the fractured zones is their distinction as possible natural or induced fractures. Usually natural fractures produce circulation losses. We have shown that this is not the case of borehole M. Drilling-induced (tensile) fractures are limited to the wellbore wall and because they do not propagate into the formation they are not generally associated with circulation losses. Tensile fractures have been found to form when the mud weight is comparable or slightly greater than pore pressure (Zoback, 2001), as in well M case.

2.4.3 Borehole Conditions

Instabilities in the borehole wall respond to different causes and present variable geometries. We classify them into four kinds:

1.) Hole in-gauge: the wellbore wall presents rugosities. Both calipers are not smooth and show minor crumblings in random directions. If the rugosities are significant the borehole is usually referred as an "overgauged" hole.

2.) Washouts: collapses of a portion of the wellbore or hole erosion observed as significant enlargement of both calipers; maybe predominant on one of them but still preserving similarities between both (Cox, 1983). Washouts are usually attributed to insufficient mud weight or improper mud chemistry design (Last, 2001). We have included under this term the alteration of plastic zones, normally associated to water-based muds that usually lead to shale hydration (osmotic swelling) and produce sticky hole causing increased torque and drag (Tare and Mody, 2002).

3.) Borehole Elongations: oriented failures on the wellbore. One diameter is significantly elongated while the other remains close to bit size. If elongations are caused by stress release failure, they are subclassified as "breakouts". Breakouts are responses to stress anisotropy (or heterogeneties) and to rock strength. The shape of the resultant hole after breaking out might not be necessarily elliptical since the spalled areas could be narrow as 'dog ears' (Zoback et al., 1985).

4.) Tight Hole: reduction of borehole size. Expected to show time-dependency in formations prone to creep, e.g. salts, siltstones. The causes of these instabilities do not seem to be clear. Some authors attribute them to the ductibility of some mineralogies and to time-dependent changes in pore pressure (Tare and Mody, 2002).

When the well is somewhat deviated, failures tend to occur asymmetrically. As a consequence, the tool may not be centered and measure one diameter smaller than bit size. These instabilities are called "key seats" (Serra, 1984b). Hydraulic fractures were not included in the previous classification. Caliper dipmeter is not likely to detect them. In any case, an intact formation can develop a fracture if borehole pressure is too high. The fracture may propagate and take in drilling fluid, and give mud back if pressure is later reduced (partial losses with some gains known as "wellbore breathing"). More importantly, these fractures provide stress information since they are known to occur parallel to the maximum stress direction (Zoback, 2001).

In the section of study, we observed all kind of instabilities with the exception of number four above. The borehole is pretty much in gauge until 12620 ft. Often, other deformations are superimposed. A comparison between two sample intervals, one stable and another unstable, is presented in figure 2-19.

Zones of washouts were selected where the borehole size did not exceed 15 inches and both caliper curves showed similar behaviour. Figure 2-20 depicts a washout example in well M. In some regions, failures are too large in both directions although some elongation still exists. We think a combination of breakout and washout is affecting these intervals. To separate the effect of each is a non trivial task since it would require better understanding of the processes causing washouts. An example is shown in figure 2-21.

The dipmeter tool has a pad length of 30 cm and width of 6 cm, meaning that the calipers will only measure borehole elongations if the area of the damaged zone is at least 200 cm^2. Caliper arms reach to the borehole wall has to be sufficient to interrupt the normal tool rotation, which is somehow dependent on the uniformity of the diameter and the departure from bit size (Plumb and Hickman, 1985).

Cox (1983) uses similarity between large caliper and resistivity curve to distinguish washouts from borehole elongated areas. Plumb and Hickman (1985), based on the comparison between borehole televiewer and dipmeter data, present a sytematic method to further discriminate between elongations and breakouts. These authors considered other characteristics of the caliper curves and the tool configuration, which is appropriate for cases where elongations are localised and not extensive. We set the following criteria to select the "borehole elongation" areas in well M:

1.) The length of the elongated depth interval is at least 1 ft, that is, it is recorded consistenly in at least two samples.

2.) The difference between caliper readings at same depth is greater than 1.5 inches.

3.) The smaller caliper is close to bit size, not greater than 14.5 inches.

4.) The tool rotation is interrupted on the zone of elongation.

Examples of borehole elongated intervals are shown in figure 2-22. The complete classification of well M instabilities is shown in figures 2-23 2-24 and 2-25, and the main features of the borehole elongated zones are described in table 2.3.

Whether the borehole elongations correspond to pure breakouts or other mechanisms is analysed next. Plumb and Hickman (1985) observed the occurrences in

azimuth-frequency plots and discarded those events with azimuth directions coincident with either the high side of the borehole when deviated, or with the azimuth of bedding dips. In our case, the well is almost vertical and the azimuth of structural dip is about S55°E which would correspond to a long axis orientation of 125 deg (or 305 deg) in table 2.3 [8].

A histogram of number of occurrences every 10 degrees of the elongated intervals is plotted in figure 2-26 where some events show the structural dip azimuth (300-310 deg). These intervals are labeled "DIP" in table 2.3, since they do not classify as breakouts. For the remaining distibution, dominant azimuths are between 250° and 260° and the corresponding intervals are categorised as stress induced breakouts in the same table. Note that such events are ramdomly distributed below 8000 ft. If accepting a wider variation, we could say that breakouts occur between 250 and 280°.

Breakout azimuth corresponds to the direction of minimum regional stress. This has been proved, theoretically (Gough and Bell, 1982), and supported with earthquakes focal mechanisms, hydraulic fracturing experiments and other stress indicators (Zoback and Zoback (1989); Zoback et al. (1986)). Breakouts in well M, hence Sh, are oriented ENE-WSW, thus SH should run approximately NNW-SSE (fig. 2-27), which is consistent with the regional tectonic model.

Regarding the "possible fractured zones", the analysis done in this section give us other insights. From the intervals described in table 2.2, the last four correspond also to breakouts which increases the probability of having tensional fractures 90° away (Zoback, 2001). In fact, the strike of these possible fractures is about N10W-S10E coinciding with the orientation of SH intrepreted from breakouts.

[8] the long axis orientation respect to the geographic north is obtained by adding the magnetic declination (10°) to the azimuth of pad 1, in case that the maximum diameter direction is registered by the pair 1-3. Otherwise, the orientation of the borehole large side has to be found first by adding 90 ° to pad 1 azimuth.

Table 2.3: Borehole Elongated Intervals. Average values over the interval. Long axis azimuth is measured from geographic north whereas "P1 az" indicates the magnetic azimuth of pad 1 (C1-3).

Depth [ft]	C1-3[in]	C2-4[in]	P1 az[deg]	Long-ax az[deg]	Breakout?
4850-4890	12.3	14.5	206	306	DIP
5035-5065	14.4	12.5	172	182	
5100-5185	15.8	12.1	160	350	
5200-5210	15.9	12.1	146	336	
5420-5450	14.1	12.6	13	203	
5583-5590	12.7	14.8	8	288	
5675-5678	14.7	12.5	279	289	
5692-5700	14.8	13	281	291	
5855-5865	15	12.3	264	274	
5970-5975	14.3	12.3	321	331	
6055-6062	14.2	12.4	353	183	
6135-6145	14.4	12.5	0	190	
6185-6200	14.4	12.3	351	181	
6370-6380	14.4	12.3	304	314	
6450-6470	12.2	14.8	293	213	
6570-6585	12.2	15	65	345	
8160-8170	12.5	16.3	155	255	YES
8275-8277	14.3	12.7	118	308	DIP
8345-8350	12.6	14.5	350	270	
8450-8470	14.9	12.3	250	260	YES
8485-8495	16.6	13.2	260	270	
8555-8575	15	12.4	267	277	
8770-8780	20.4	14	246	256	YES
8802-8810	19.5	14	228	238	
8870-8874	12.5	15.3	174	274	
8890-8897	13	16.4	155	255	YES
8920-8945	16.4	13.4	68	258	YES
8960-9000	15.6	12.7	63	253	YES
9030-9060	15.7	12.8	80	270	
9070-9120	16.1	12.6	82	272	
9150-9190	14.7	12.4	91	281	
9200-9210	16.1	12.7	84	274	
9230-9250	17	12.6	72	262	
9255-9260	16	12.8	66	256	YES
9325-9350	12.4	16	336	256	YES
9410-9430	12.9	16.9	336	256	YES
9440-9460	12.8	18	339	259	YES
9480-9560	12.8	18	341	261	
9600-9630	20.6	13.2	341	351	
9790-9825	13.1	15.8	338	258	YES
9835-9895	13.3	19.6	344	264	
9980-10100	21.5	13.7	246	256	YES
11000-11020	13.6	21.5	5	285	
11540-11550	19.5	13.6	260	270	
11580-11625	21.5	13.8	244	254	YES
11765-11850	21.3	13.5	231	241	
11870-11880	20.6	13.5	228	238	
11890-11930	20.2	12.8	220	230	
12010-12040	21.3	14	240	250	YES
12140-12240	13.1	21.4	141	241	
12245-12265	21.1	13.1	63	253	YES
12320-12340	20.1	13.7	66	262	
12442-12495	13.3	21.2	310	230	
12510-12520	12.8	17.3	336	256	YES
12545-12570	12.6	15.4	310	230	
12580-12600	12.4	14.7	292	212	
12610-12620	12.5	16	318	238	
12670-12690	15.5	12.4	61	251	YES
12880-12900	14.3	12.5	260	270	

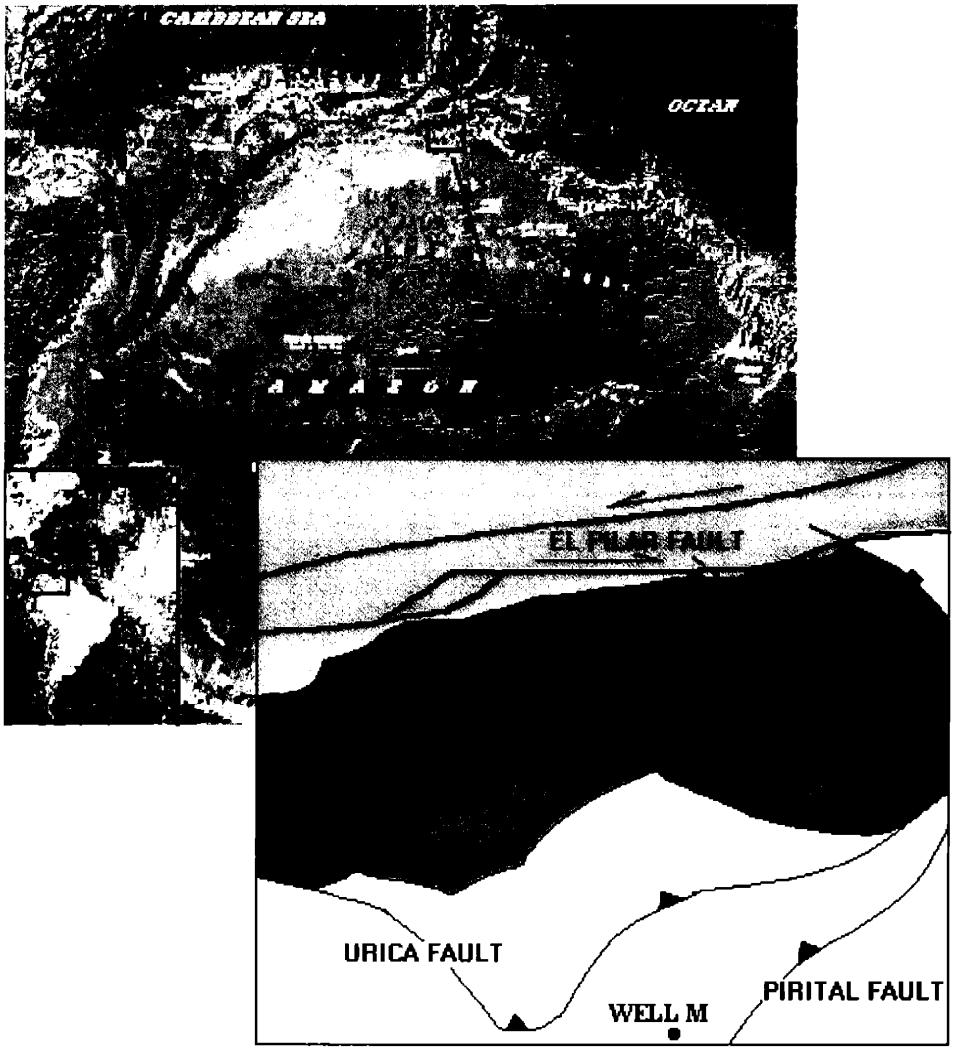

Figure 2-1: Location and structural setting of the area of study. Enlarged figure represents an area of about 200 by 300 km. Modified from Report: PEP Macal-Geología Structural (2001)

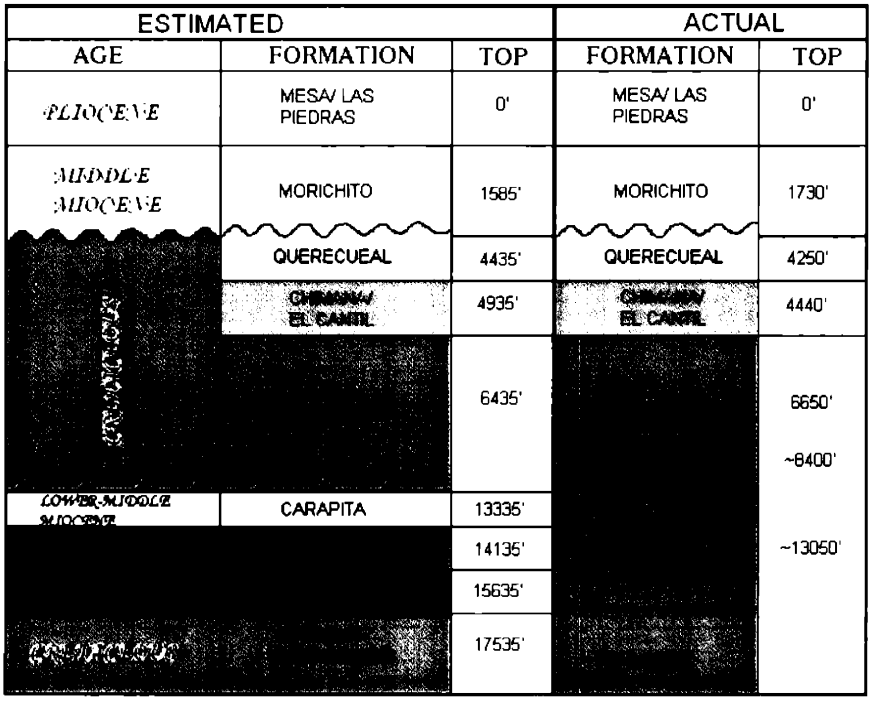

Figure 2-2: Stratigraphic column and prognosis. Ages, lithologies and formation tops were established based on biostratigraphy of high resolution (foraminifera, nanoplankton calcareous and palynology), and sedimentology analysis (cuttings, petrography and X-ray diffraction). Modified from Report: PEP Macal- Estratigrafía (2001).

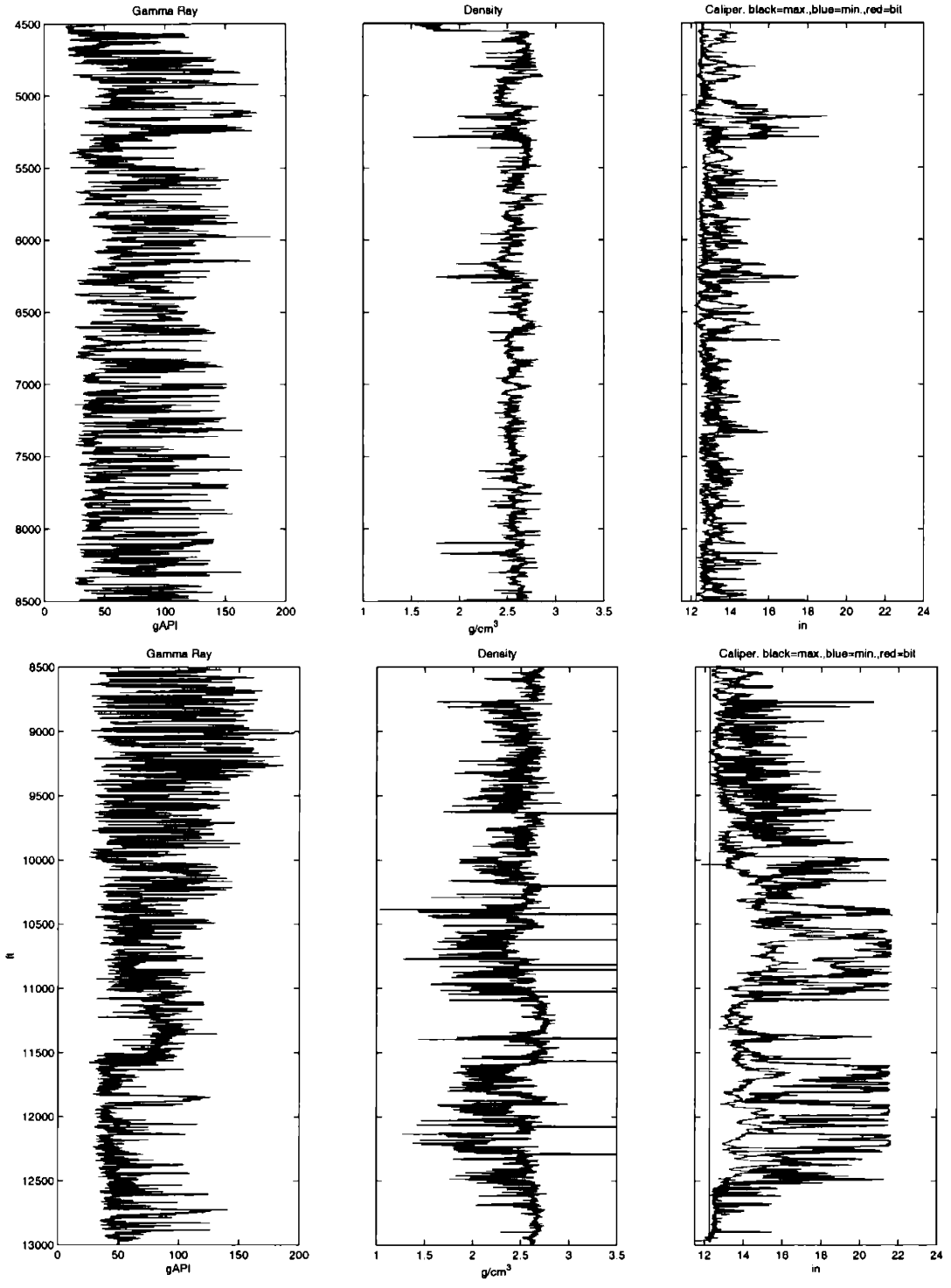

Figure 2-3: Gamma ray and density logs. Right-most log is maximum (black) and minimum (blue) hole diameter.

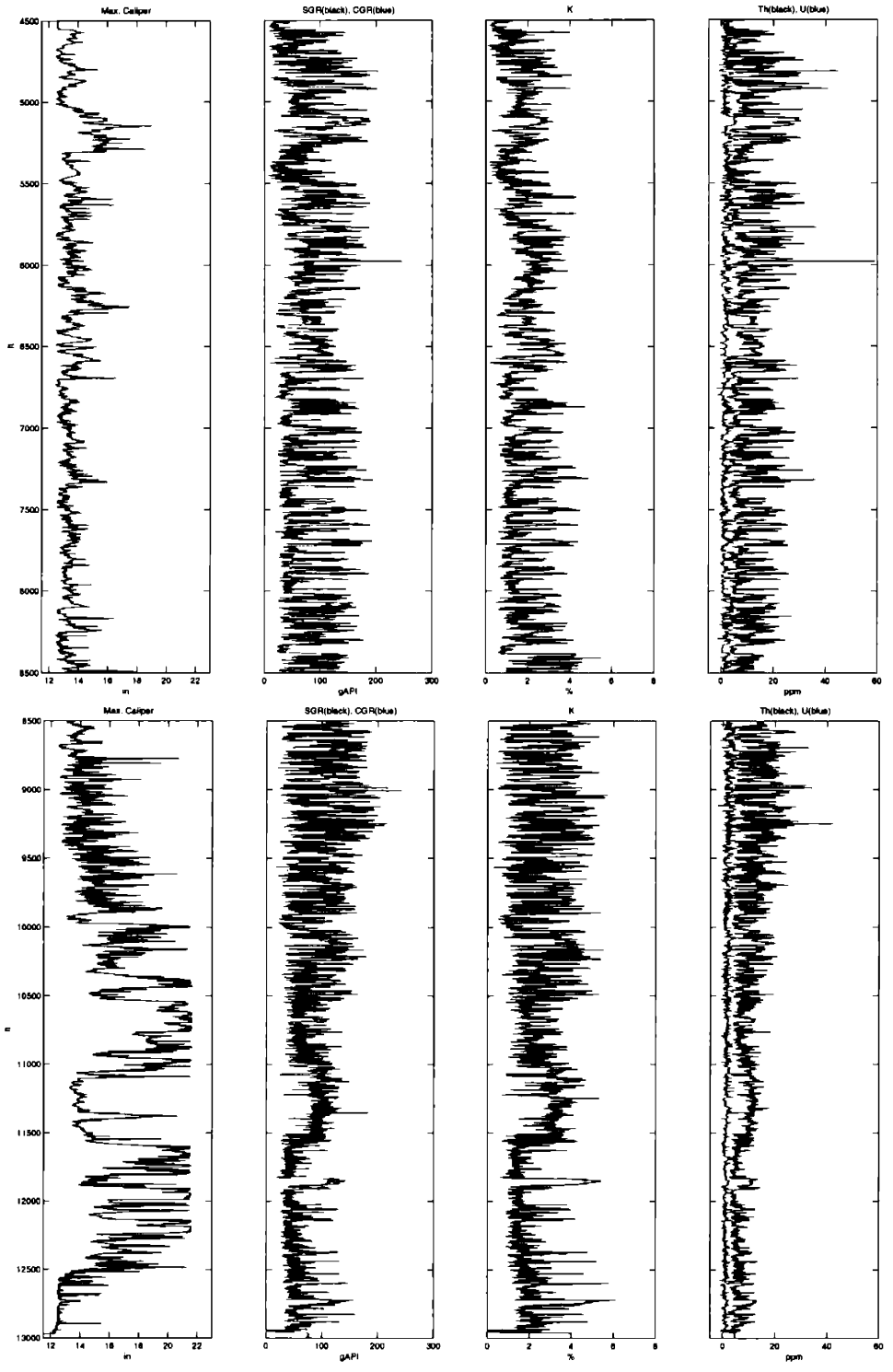

Figure 2-4: Natural Gamma Ray Spectrometry. From left to right: maximum borehole diameter; SGR (gamma ray from the composite contributions of potassium, thorium and uranium) in black, and CGR (gamma ray from thorium and potassium only) in blue; Potassium curve; Thorium (Th) and Uranium (U) curves (blue).

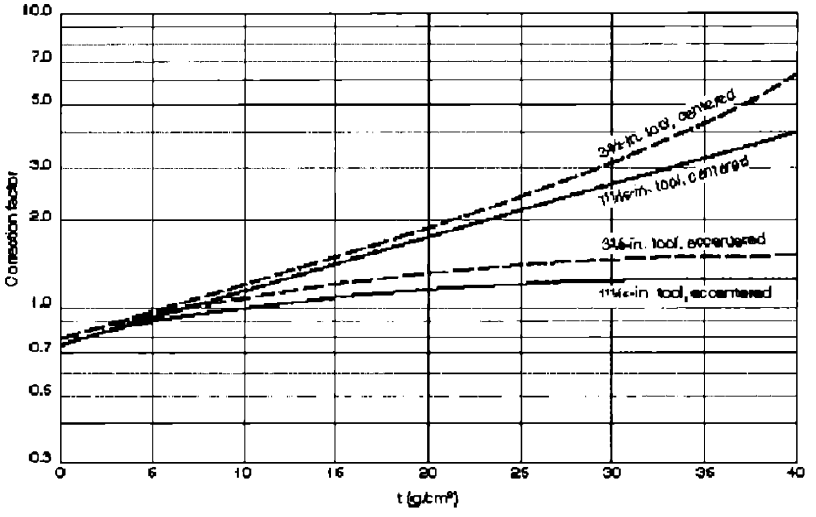

Figure 2-5: Chart GR-1. The correction factor normalises the response to an off-centered tool in an 8 in borehole with 10-lbm mud. t is obtained at each depth from: $t = \frac{W_{mud}}{8.345}(\frac{2.54}{2}(d_{hole} - d_{sonde}))$. d_{sonde} refers to the tool diameter and W_{mud} is the mud weight. Modified from Schlumberger (2002a). Correction factors for well M are between 1.2 and 1.6.

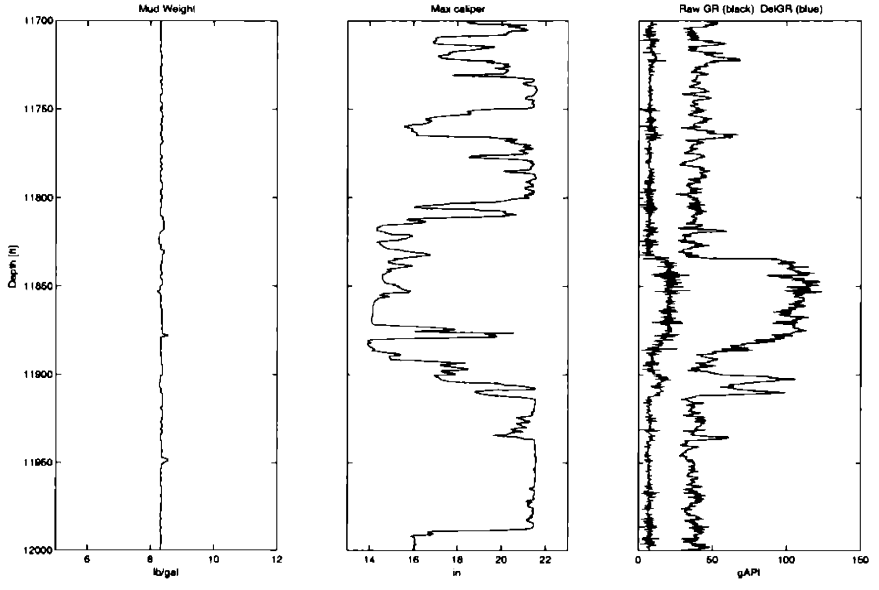

Figure 2-6: Correction of gamma ray log by borehole size and mud weight. In the right-most panel, the raw gamma is plotted in black. The difference between the corrected reading (shown in fig. 2-3), and the raw one is plotted in blue.

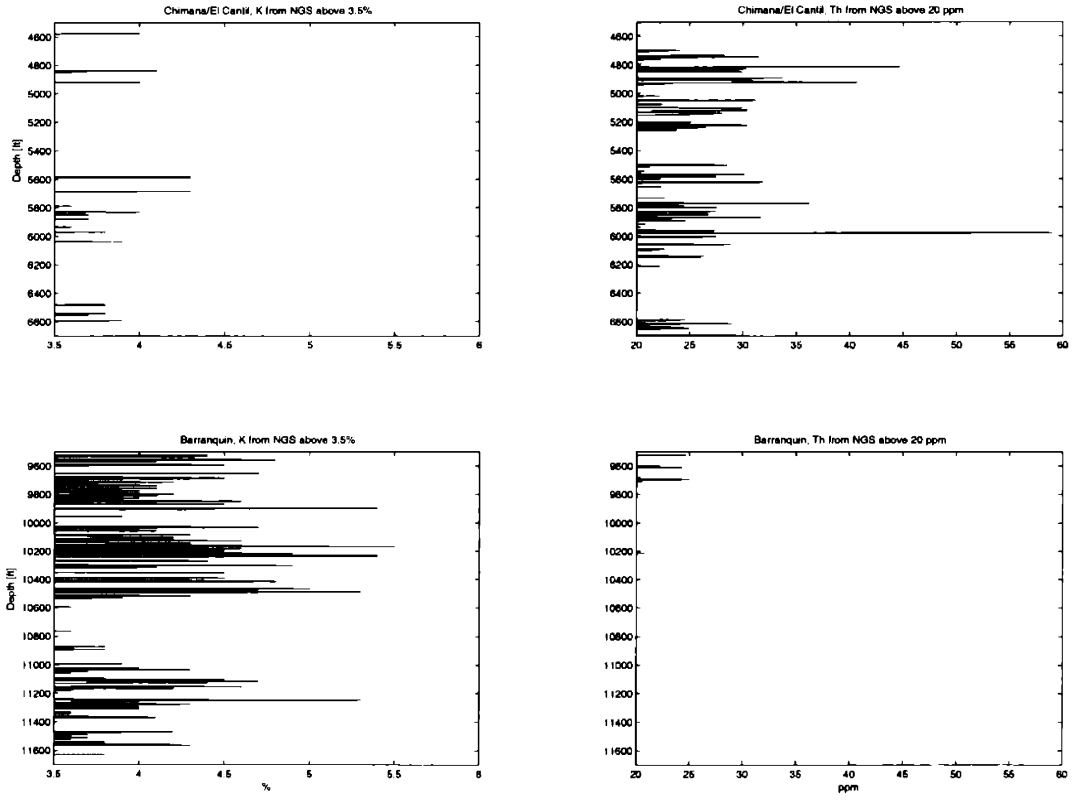

Figure 2-7: General comparison of K and Th gamma ray radioactivity from formations Chimana/El Cantil and Barranquín showing the main lithological differences between these two units. Chimana/El Cantil (top figures) contains calcites and several different clay minerals while Barranquín (bottom figures) is mainly composed of sandstones with feldspars and/or illite, interlayered or as cement in fractures, and red silts. In the case of Chimana Fm. K curve (top left) shows small activity in comparison with the potassium-bearing rocks of Barranquín (bottom left). The opposite occurs with the concentrations of Thorium (right figures).

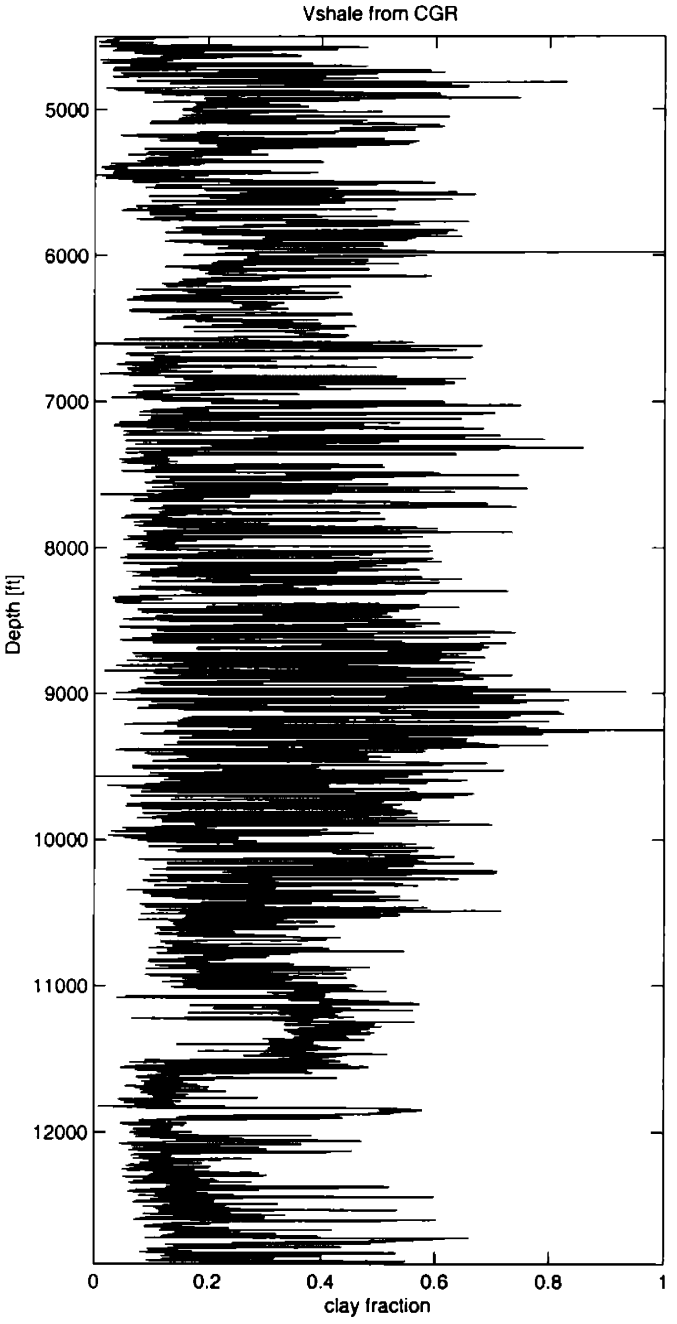

Figure 2-8: Shale volume computed from the gamma ray formula of clay index. 1 indicates a 100% clay rock or a shalestone. Uranium was substrated from gamma ray curve. For formation Chimana/El Cantil (4500 to 6655 ft) $CGR_{min} = 6.905$ at 5453 ft, and for Barranquín (6655 to 13000 ft) $CGR_{min} = 17$ at 7349 ft.

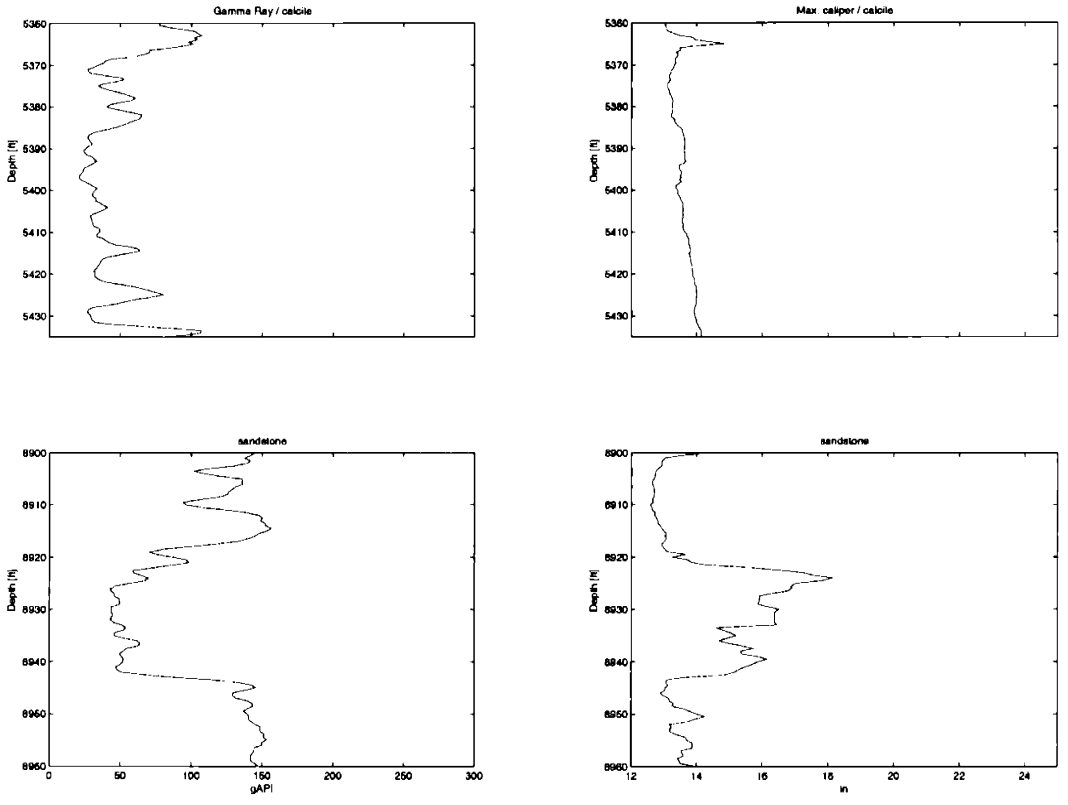

Figure 2-9: Gamma ray logs (left) in limestone (top) and sandstone (bottom). To the right, corresponding long borehole axis at depth intervals. Calcium rich rocks are less likely to fail.

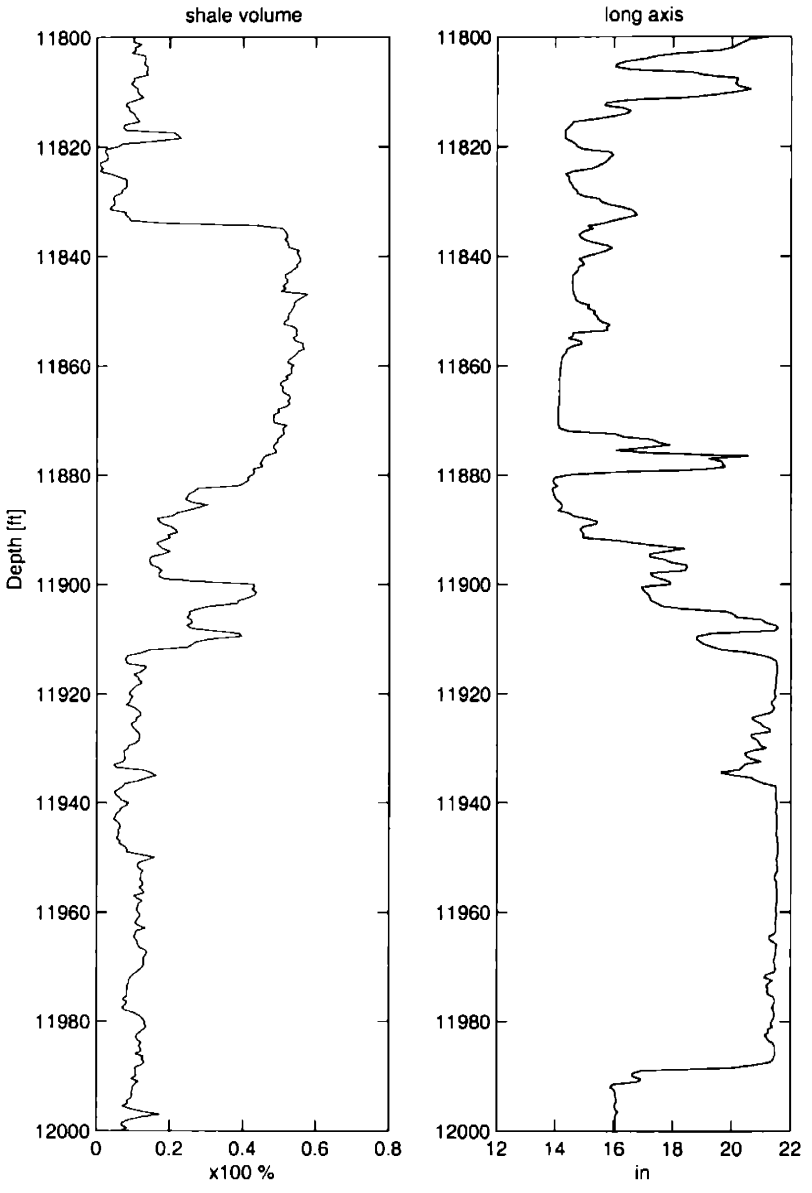

Figure 2-10: Shale volume (left) and long borehole diameter (right). There is a correlation between high shale volume and more preserved borehole radius.

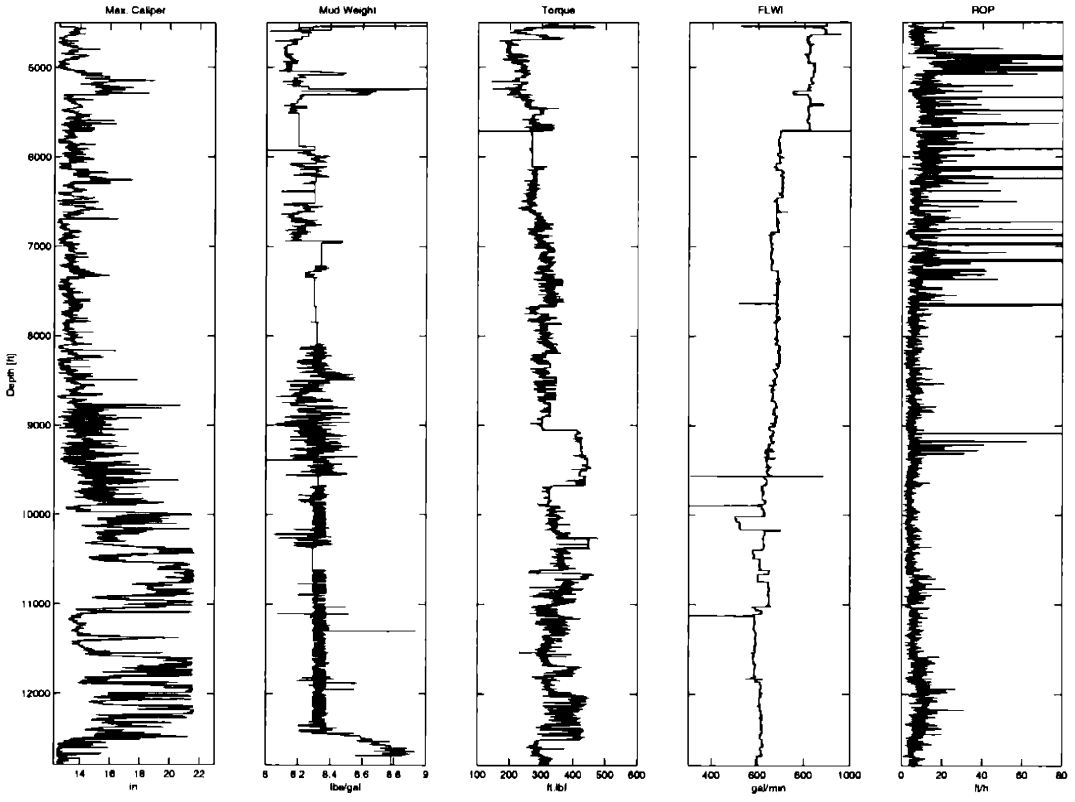

Figure 2-11: From left to right, maximum borehole diameter, mud weight, torque, fluid inyected and rate of perforation (drilling). These logs indicate no particular difficulties were encountered while drilling this interval, however the borehole is unstable.

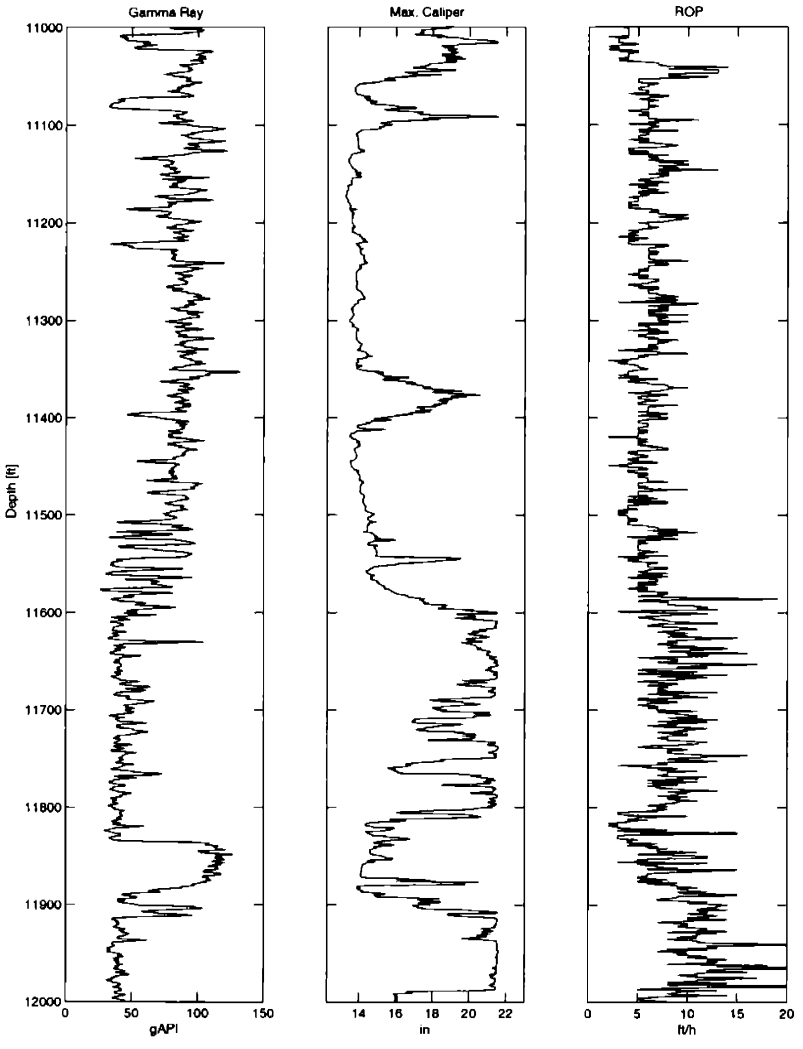

Figure 2-12: Correlation between deformations in the borehole (middle) and rate of drilling (right). Rock intervals easier to drill are more likely to fail since they are less compacted (or less mechanically resistant).

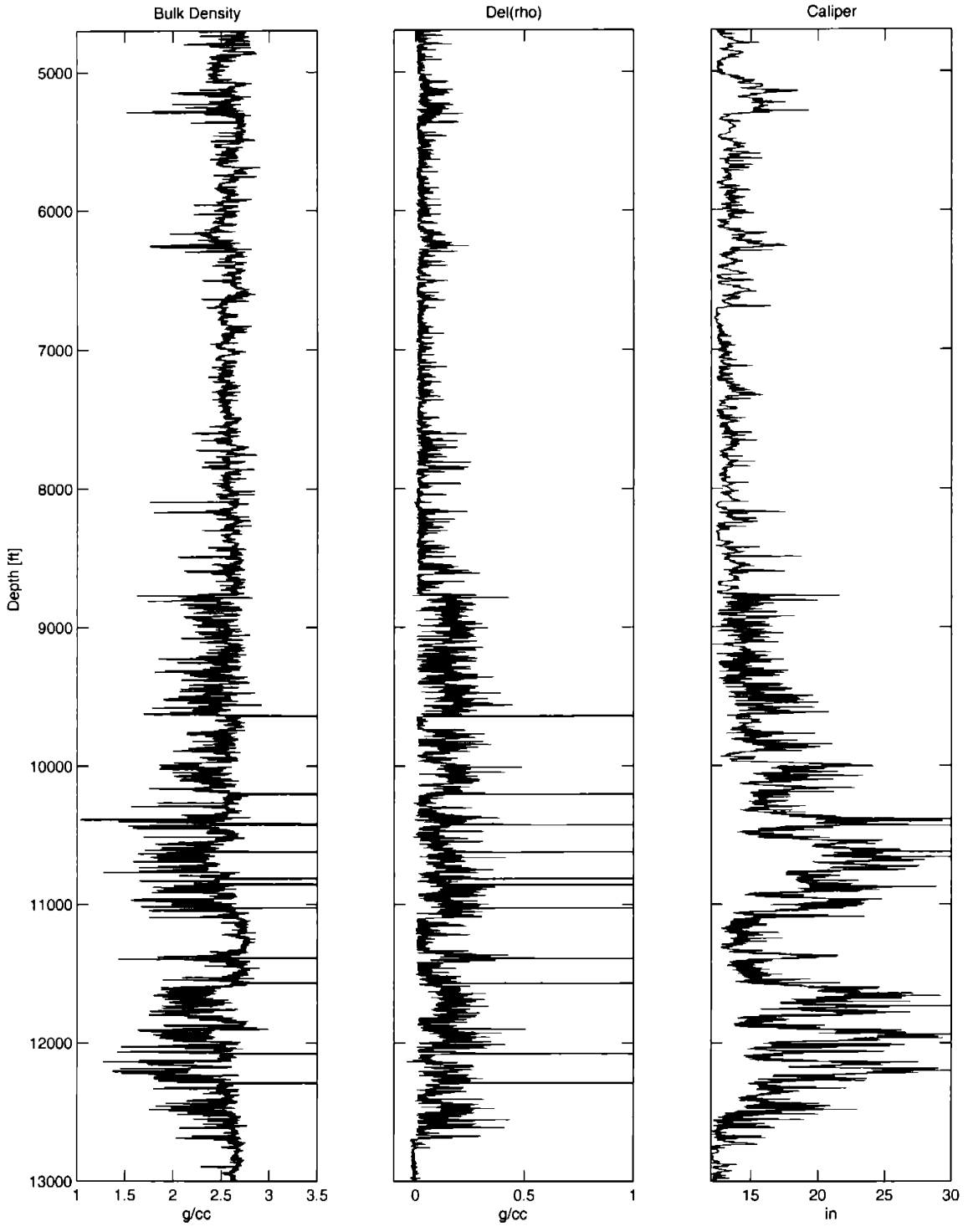

Figure 2-13: Bulk density (left), bulk density correction (middle) and caliper data from LDT (right). Where the borehole is larger, density decreases indicating that the tool is measuring the effect of the drilling fluid.

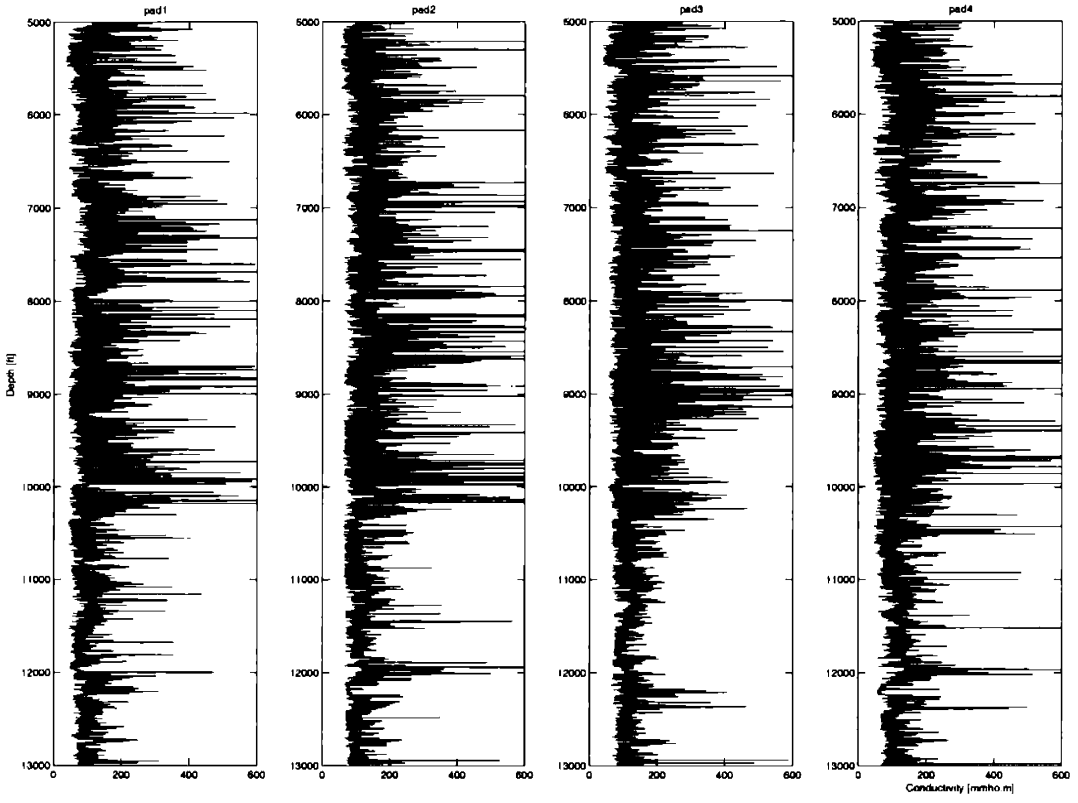

Figure 2-14: Conductivity recorded from dipmeter. Pads 1 and 3 are orthogonal to pair 2-4.

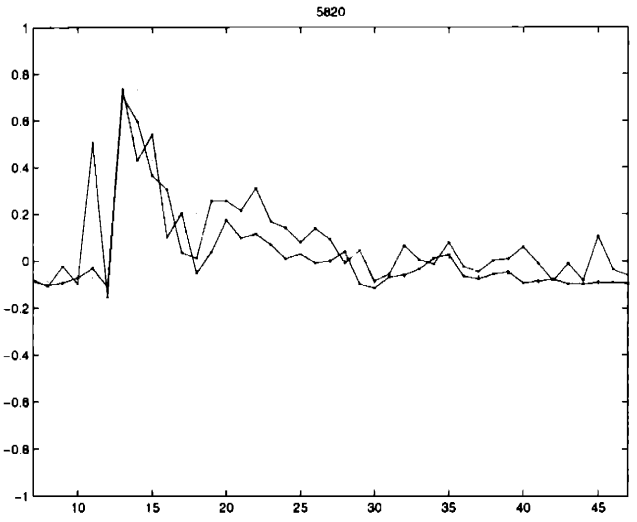

Figure 2-15: Signals of pads 1 (blue) and 3 (light blue) normalised and superimposed for the depth interval 5820-5840 ft. The curve in red corresponds to the signal recorded at pad 3 shifted up (left) by 0.5 ft. This shift produces the best correlation among different displacements in a 6 ft window.

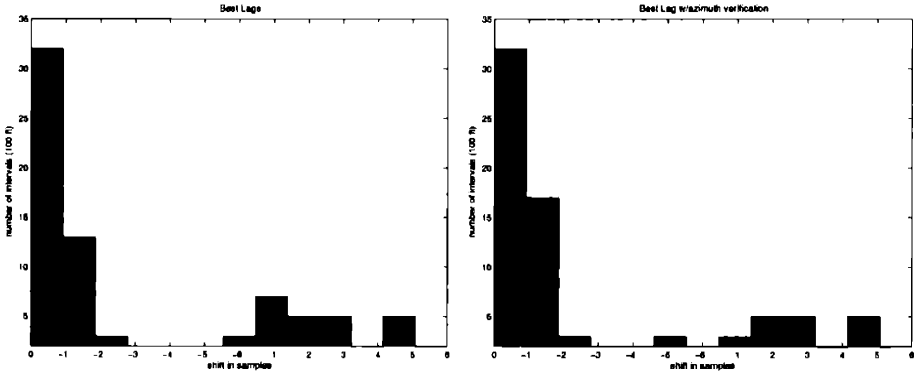

Figure 2-16: Left: Best and average lag-frequency histograms for the whole section showing three predominant modes: zero shift and +/- 1. Right: Histogram after adding +1 lag contributions to -1 lag based on tool azimuth.

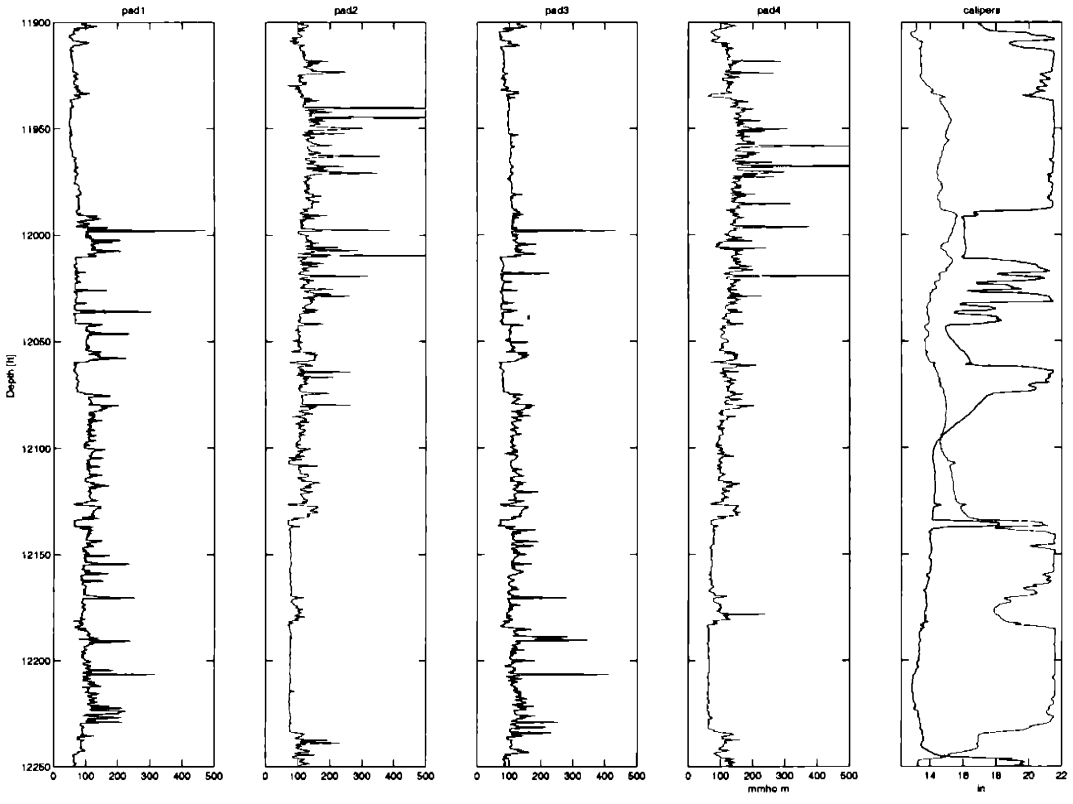

Figure 2-17: Dipmeter data, caliper (right-most panel) and conductivity (pad 1 to 4 from left to right), are unreliable in regions where arms are completely opened. An example around 12000 ft suggests that the borehole maximum diameter is larger than 21.7 in. Note the flat character of the conductivity curves in comparison with regions where tool is pressing against the wall. Between 11900 and 11980 ft, pads 1 and 3 are not reaching the wall whereas between 12140 and 12240 ft is the pair 2-4 the one loose.

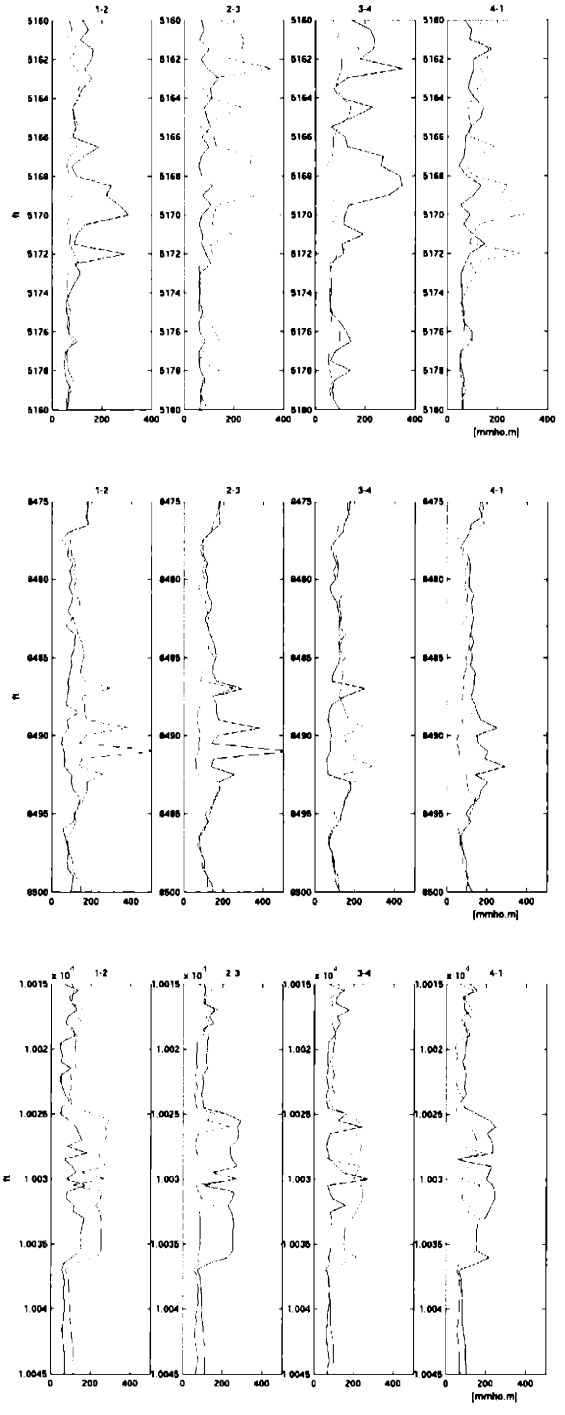

Figure 2-18: Possible fractured/anisotropic zones from increase of conductivities in opposite pads. From top to bottom, the zones of fractures can be seen around: 5166-5170 ft, 8485-8495 ft and 10025-10035 ft

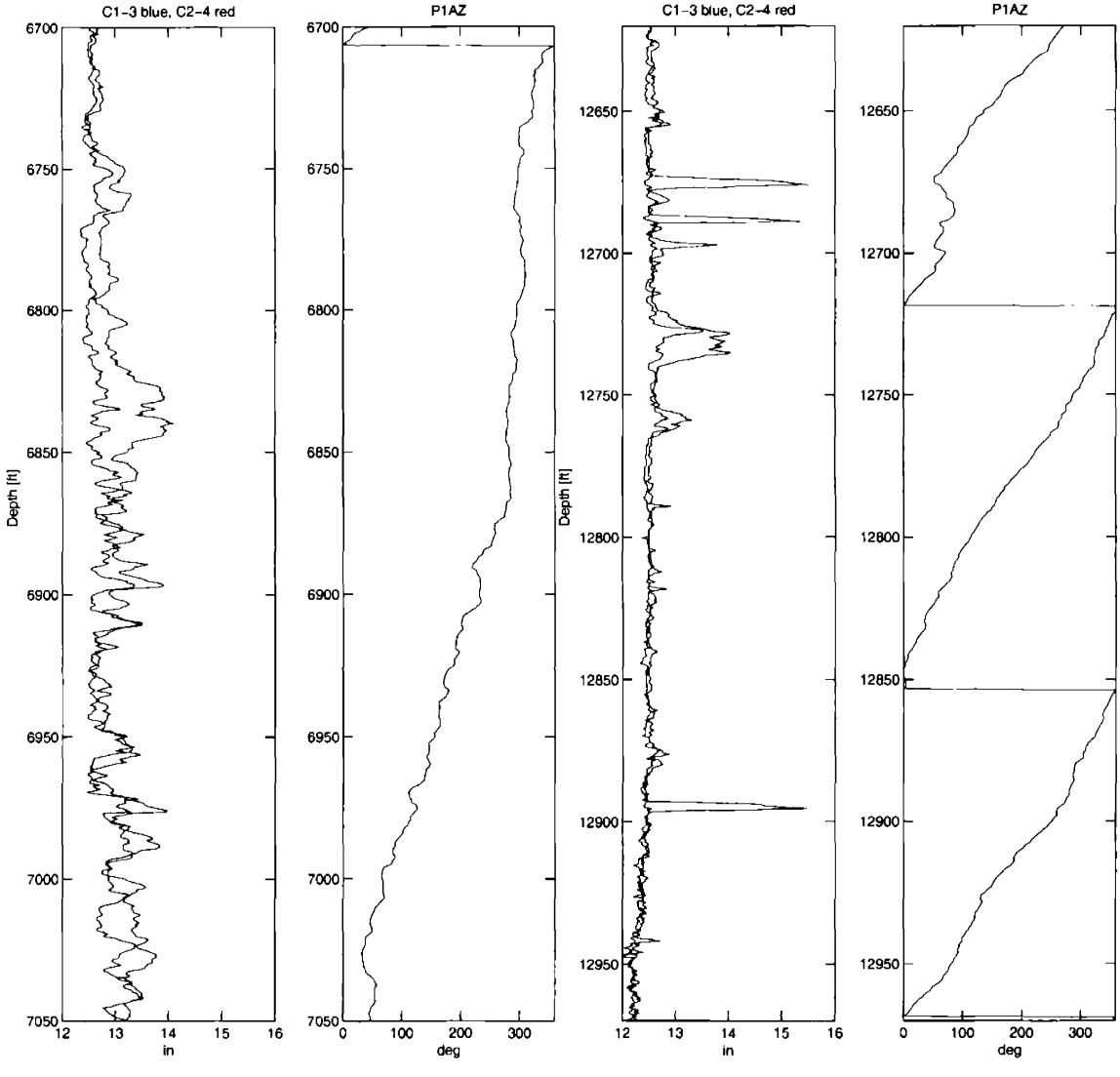

Figure 2-19: Caliper data in two regions, to the left the borehole is in gauge with probably other instabilities superimposed. The right panels show the behaviour below 12620 ft where apart from some localised elongations, the borehole is stable. Notice how the tool rotation is interrupted when the borehole has caverns. In the second example, tool rotates 360° in 320 ft, almost three times, whereas in the left section (6700-7050 ft) it barely completes one rotation.

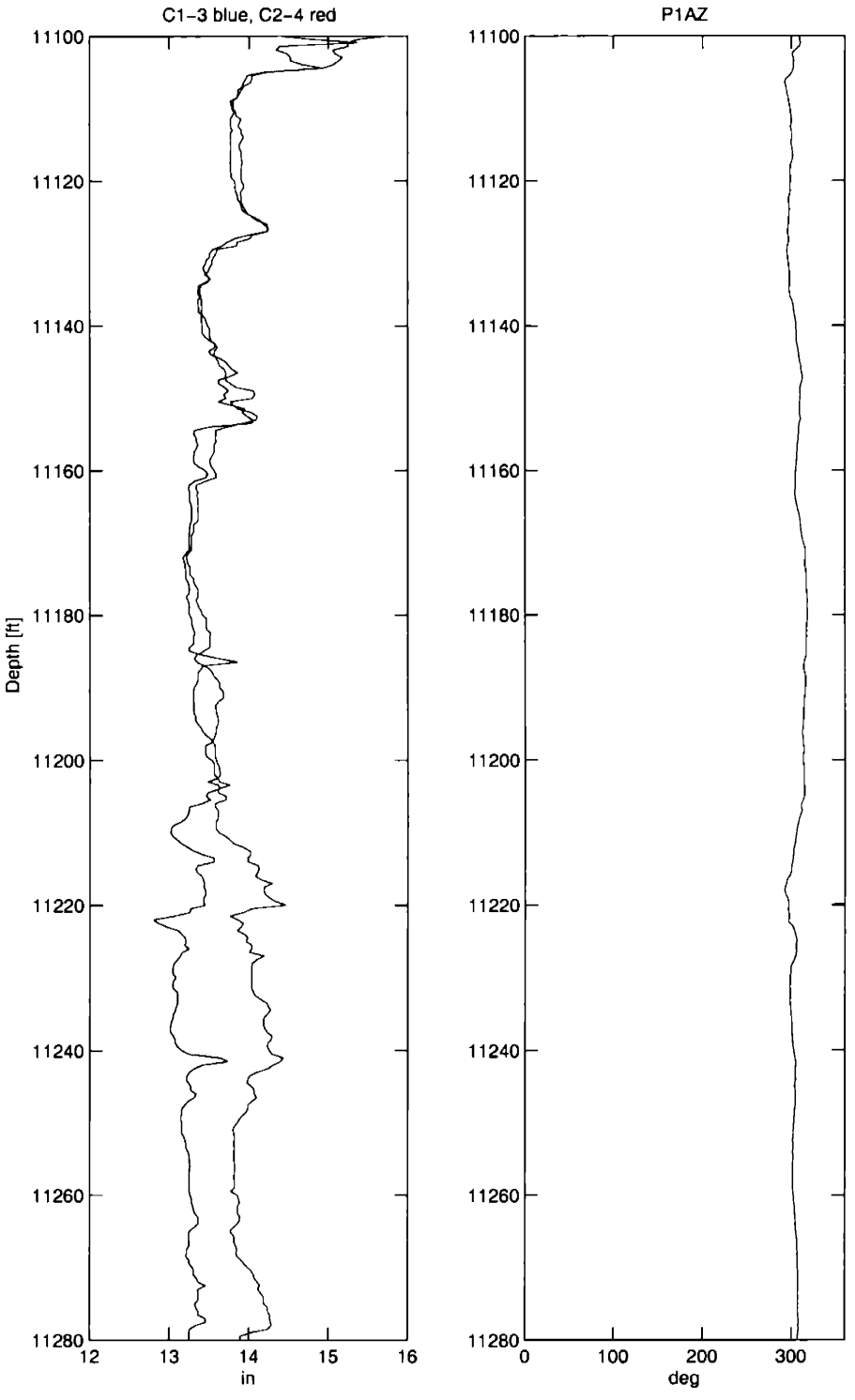

Figure 2-20: Example of washout. Both calipers show significant enlargements and curves are similar.

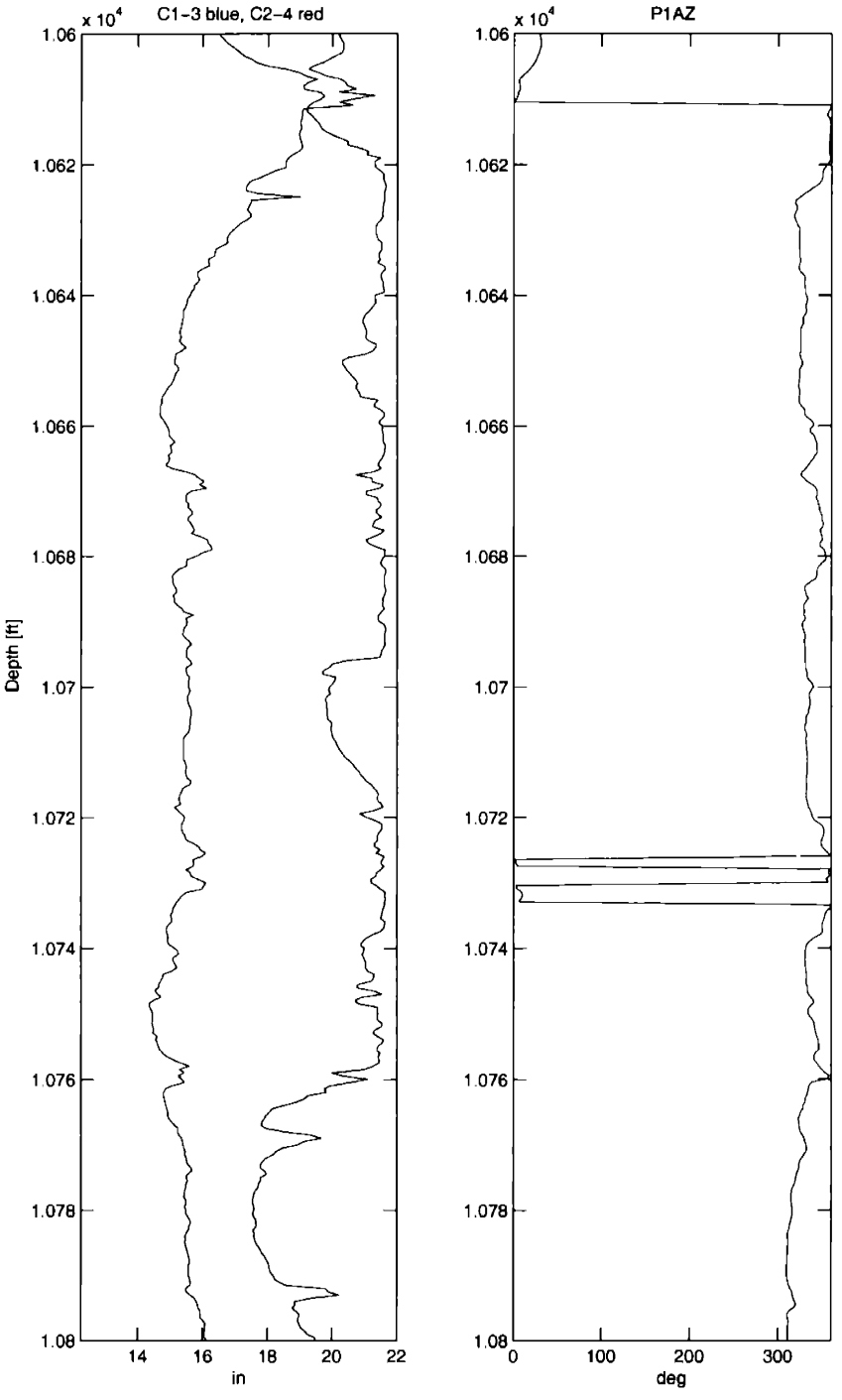

Figure 2-21: Example of a region where washouts and breakouts are superimposed (10620-10760 ft). The diameters are too large (more than 3.5 in larger than bit size) to be considered pure washout. On the other hand, borehole is elongated in the direction of caliper 2-4 and curves are somewhat different indicating that it may be a breakout area.

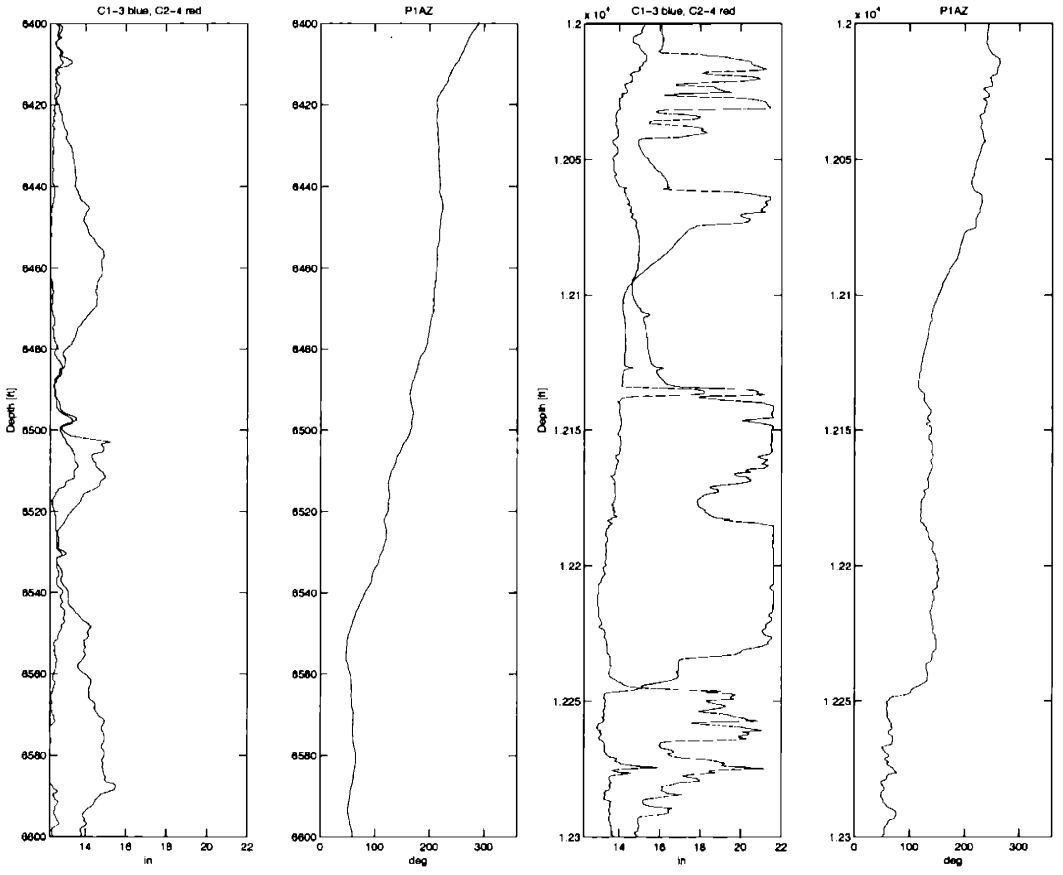

Figure 2-22: Example of region of borehole elongations, possibly breakouts. On the left, two areas of elongations are separated by a washout (6480-6540 ft). On the right, the interval between 12140 and 12260 ft shows an ovalised borehole with one axis more than 8 in larger than the other. In both cases, the caverns are deep enough to stop the tool from its regular rotation

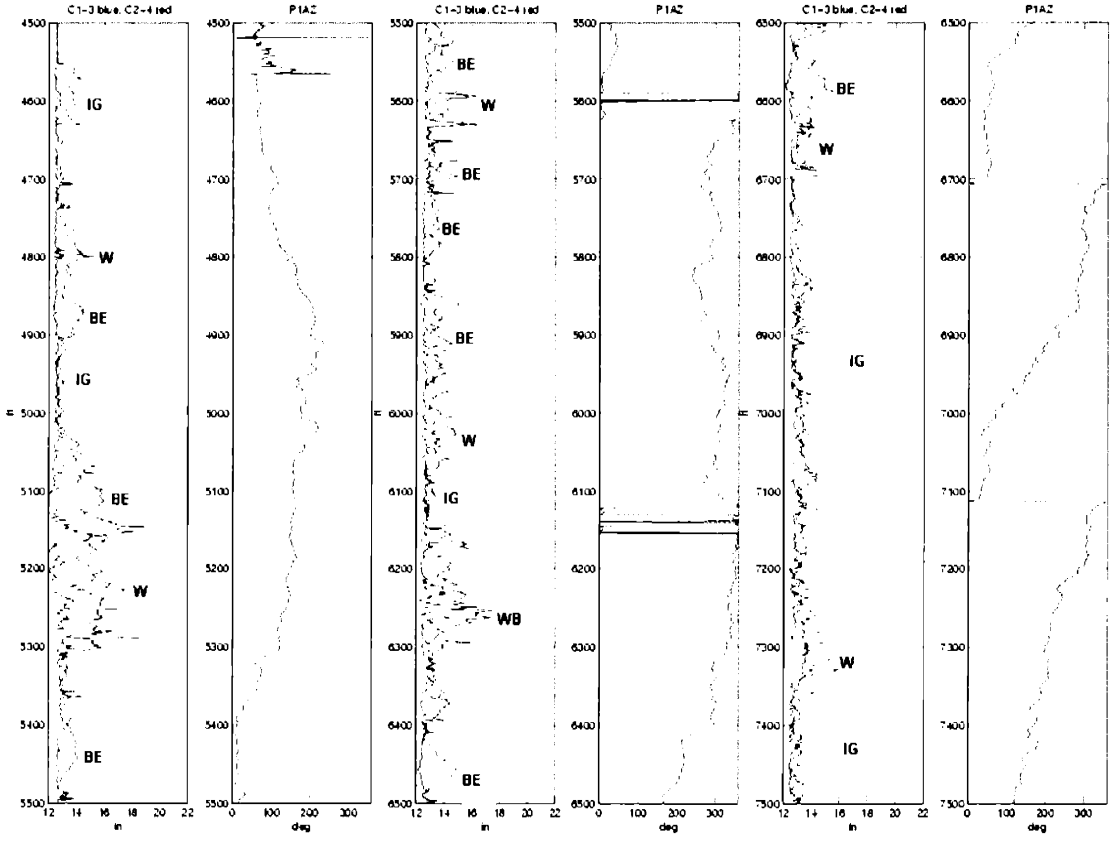

Figure 2-23: General classification of borehole instabilities 4500-7500 ft. IG: hole in gauge, W: washout, BE: borehole elongation, WB: washout+breakout, S: stable.

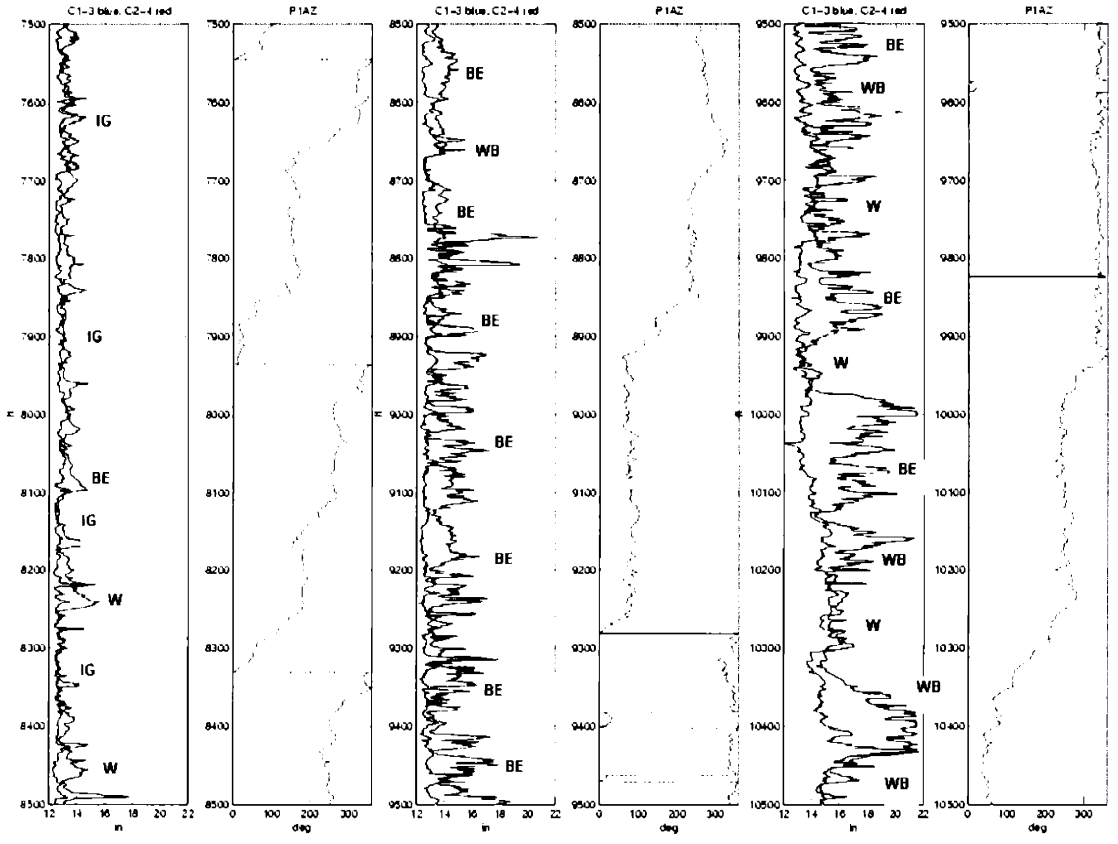

Figure 2-24: General classification of borehole instabilities 7500-10500 ft. IG: hole in gauge, W: washout, BE: borehole elongation, WB: washout+breakout, S: stable.

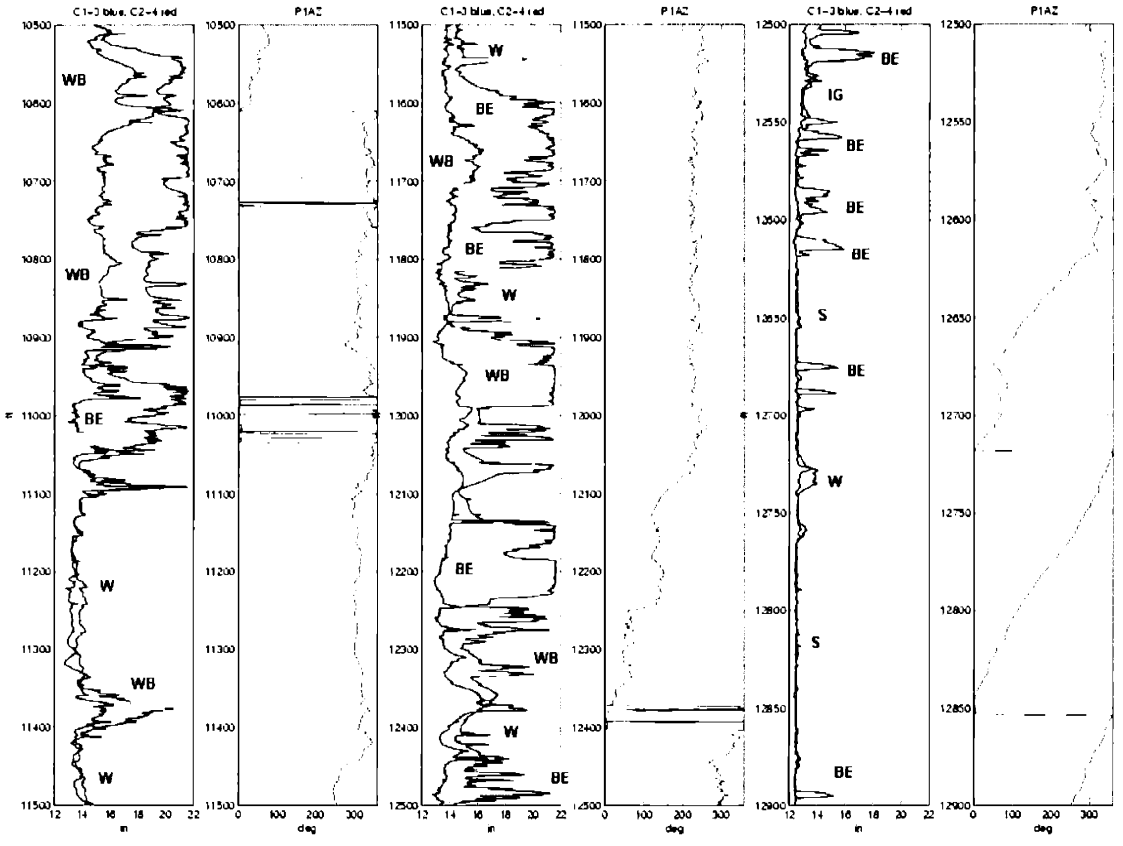

Figure 2-25: General classification of borehole instabilities 10500-12900 ft. IG: hole in gauge, W: washout, BE: borehole elongation, WB: washout+breakout, S: stable.

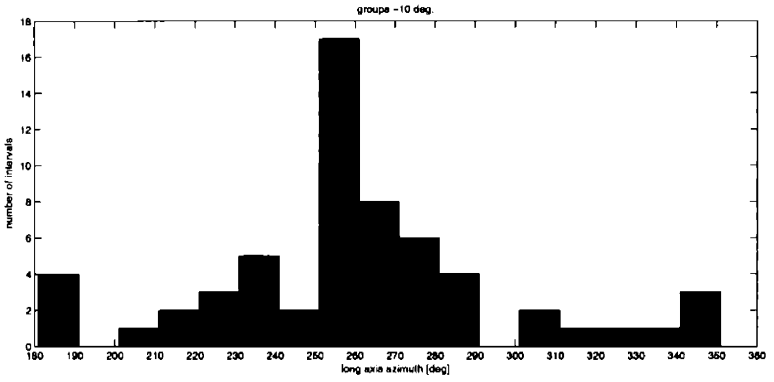

Figure 2-26: Orientation of Elongations. Histogram of azimuths (from geographic north). Angles between 250 and 260 deg are more frequent and consistent in the section.

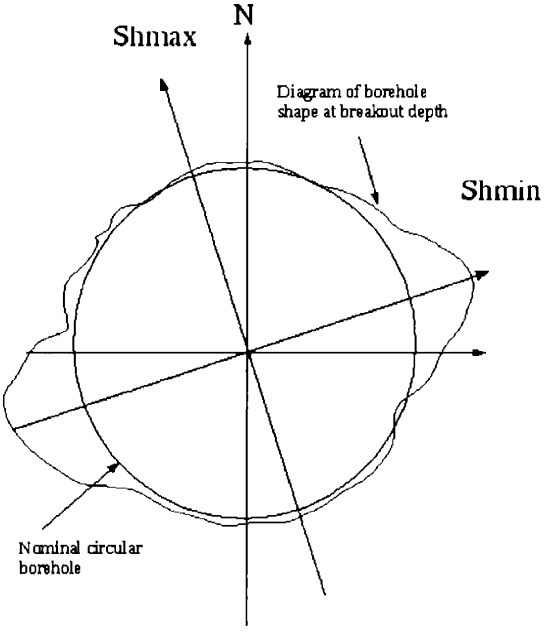

Figure 2-27: Borehole cross-section (constant depth) schematic representation of the maximum and minimum horizontal stress orientation extracted based on breakout data.

Chapter 3

Borehole Acoustics

A sonic logging tool (DSI[1]) was ran in well M. The DSI tool consists of a transmitter and a multireceiver section. It has three transducers: one monopole (omnidirectional) transmitter and two unidirectional dipole transducers oriented perpendicular to each other. The receiver section consists of eight stations 0.5 ft apart, each of them has two hydrophone pairs, one oriented in line with the upper dipole and the other in line with the lower dipole. The outputs from each pair are substracted for dipole reception and summed for monopole reception [2].

The distance between the monopole source and the near receiver of the array is 9 ft. The source-receiver spacing is 11 ft for the upper dipole source and 11.5 ft for the lower dipole source. An isolation joint separates the transmitter from the receiver section acting as a mechanical filter to avoid signals to travel up the tool.

The tool has several acquisition modes. For well M, upper/lower dipole, cross dipole, monopole Stoneley and monopole P and S modes were recorded. The dipole transmitters and the monopole source in its Stoneley mode are low-frequency with an excitation pulse below 1 kHz, whereas a high-frequency pulse drives the monopole transducer in its P and S mode.

The source frequency along with several other parameters (formation slowness, source-receiver spacing etc) determines the depth of investigation. Conventionally, it

[1]Dipole Shear Sonic Imager. Mark of Schlumberger

[2]a complete DSI tool description can be found at http://www.slb.com/Hub

varies between 12 and 100 cm (Serra, 1984a). At the low frequency band, penetration may be deeper and beyond altered zone. The large deformations observed on well M exceed, in some circumstances, the specifications of the DSI tool.

The applications of full waveform acoustic data are numerous. We will only deal with compressional and shear wave velocity determination to further obtain the rock elastic parameters and to estimate porosity and density. The mechanical strength is computed from the static moduli. The compressional wave velocity is uniquely obtained from the sonic tool through head waves recorded in monopole data. This estimation is, in general, a robust process. On the other hand, the S velocity determination requires a more careful analysis, in part because it is not always possible to record head waves propagating at the shear speed. In those cases, shear velocity has to be estimated from the flexural or the screw waves provided by the dipole or quadrupole data.

In well M, the formation is fast. We have redundancy to obtain shear velocities: from the monopole high-frequency set (shear refracted waves/low frequency pseudo-Rayleigh waves), from the monopole low-frequency set (in theory from the phase velocity of the Stoneley wave), and from the dipole or crossdipole set (flexural waves). Unfortunately, sensitivity to the type of processing, among other reasons, complicates the determination of the true shear velocity. The unique borehole conditions found in well M are expected to affect the sonic data and therefore the determination of velocities. In principle, the borehole irregularities should complicate the identification of some borehole modes, whose wavelengths are directly related to the borehole size, and reflections from the borehole wall might interfere destructively with other arrivals.

In the following, the monopole and dipole data are presented separately. In each case, the compressional and shear wave velocities as well as the waveforms, are analysed to understand the effects of the borehole conditions on these type of logs. Finally, porosity, density, the elastic parameters and the rock strength are obtained.

3.1 Monopole Data

Two sets of data are conveniently generated with axisymmetric sources from the DSI tool. The difference between them is the frequency band of operation of the source. In the first case, Monopole P and S, frequencies between 8 and 30 kHz are excited. The second case corresponds to the Monopole Stoneley mode, in which frequencies are between 80 Hz and 5 kHz. On this band, the Stoneley mode is widely excited and it can be used for specific applications as, for instance, permeability estimation or evaluation of fractures (Burns et al., 1988).

The Monopole P and S data set is analysed to obtain the compressional and shear velocities. There have been some attempts to compute formation shear velocity from the phase velocity of the Stoneley wave but it has also been proved that this method underestimates shear velocity in high permeability zones (Toksöz and Cheng, 1991).

In figure 3-1 the first 3 ms of the monopole P and S dataset from 12486 to 11986 ft are plotted in variable density. This type of display is a convenient way to visually identify the borehole modes and, because one can see both amplitude and time for the whole record, it gives an idea of the signal quality as a function of depth in the borehole.

We identify the main borehole waves: the first arrival, at about 0.85 ms, corresponds to the refracted compressional wave. The amplitude of this arrival is low in comparison with the rest of the section. Following the P arrival, the shear head wave, together with the low frequency pseudo Rayleigh, are observed around 1.2 ms. Both, the compressional and the shear wavefronts vary sharply with lithology (depth) but the shear wave displays a somewhat greater variation.

Within the pseudo Rayleigh wave train, the high frequency component of the Stoneley wave is easily recognized at about 2.4 ms. At these frequencies, the Stoneley wave is travelling at a velocity close to the fluid velocity. Although variable density plots are not appropriate to estimate accurate travel times, the boundary wave velocity is roughly 1150 m/s. Note that unlike the head/pseudo Rayleigh waves, the Stoneley wavefront remains relatively constant in depth.

A final remark about figure 3-1 concerns the Vp/Vs ratio. In spite of its low amplitude, the compressional arrival is identifiable everywhere in the section. However, the shear wave seems to be somehow obscured at some depths where, coincidentially, the P wave velocity decreases, as for example around 12390 ft and 12145 ft. Note as well that the quality of the pseudo Rayleigh wave is in general reduced at these bands. An initial explanation might be that shear velocity at these intervals is slow, and therefore no shear refracted wave exists. For instance, between 12415 and 12390 ft, Δt_p is roughly 0.11 ms which represents a reduction in compressional velocity of about 350 m/s. If the shear velocity dropped to less than the fluid velocity, it would imply a change of about 700 m/s, which is very unlikely.

The dissaperance of the shear wave could be also attributed to highly attenuating media, due to thinly laminated intervals or presence of fractures, that even in fast formations, could reduce the refracted shear energy significantly (Zemanek et al., 1991).

At the bottom of figure 3-1 we show the borehole diameters in the same interval. The borehole cross section changes rapidly between 15 and 21 inches and most of the changes in character observed in the VTA plot can be associated to differences in borehole size. However, it is not very clear whether the low energy bands corresponds to larger holes. Without losing generality, reflections from sharp contrasts in the borehole wall may be interfering with the rest of the borehole modes in a complicated pattern and as a function of the mode frequency, the formation parameters and others (Bouchon and Schmitt, 1989).

The Monopole Stoneley dataset shows a clearer picture of the effects of the borehole shape (fig. 3-2). In this frequency range the boundary wave features reverse dispersion, i.e. phase velocity increasing with frequency. The variable density plot of the Stoneley dataset shows reflections coming from abrupt changes of diameter as for example at 12146 ft. Even at high frequencies (fig. 3-1), the Stoneley arrival is blurred where the diameter variations are rapid (below 12286 ft).

A better correlation between character of the monopole P and S data and the hole size is observed between 11000 and 11500 ft (in figure 3-3). Probably because the

borehole is relatively smoother at these intervals, it is clear that regions of low data quality are related to zones of larger hole, more elliptical shapes and more rugosities.

3.1.1 Quality Control of P and S Automatic Velocities

The acquisition unit is equipped with a high-speed array processor that uses the slowness-time-coherence (STC) method to determine compressional, shear and Stoneley wave slowness. STC processing computes coherence within time windows of the whole array for different moveouts, then a semblance plot shows regions of large coherence that correspond to a particular slowness or velocity, and arrival time (Kimball and Marzetta, 1984). Matching them to the propagation characteristics of the wave types sought, produces a continuous log of velocity versus depth. Because this is an automated process, velocities of every mode can be obtained as often as the depth sample rate (0.5 ft).

P and S wave velocities versus depth are shown in figure 3-4 together with the gamma ray and the caliper data. The shear wave velocity is in average 2700 m/s indicating that the formations logged are fast. An extended analysis of the correlation between lithology, velocities and borehole deformations is presented in a later section. However, we should mention here that the rapid variation of velocities with depth is initially explained given the fine interlayering of clean and shalier sandstones, specially between 8000 and 10000 ft. Nonetheless, errors inherent to the processing technique cannot be ignored.

Some of the assumptions of the automatic semblance processing are: (1) the formation is vertically homogeneous over the span of the receiver array- 3.5 ft in this case, (2) it uses a peak-finding routine limited to a pre-specified region and (3) it automatically classifies the arrivals based on some constraints empirically derived and sometimes dependent on the energy function (therefore related to (1) above) (Kimball and Marzetta, 1984).

Control points, analysed separately to test the quality of the automatic process, are plotted together with the STC chosen depths in figure 3-5. Significant differences are seen, sometimes as large as 40% in the P velocity (although only about 10% in

average). The automatic velocities are not consistently larger or smaller but vary more than the velocities individually picked.

The control velocities were determined from a semblance type of processing as well but actual picking was done manually, yet it is impractical to inspect visually contour plots for every depth. The energy functions were generated using a moveout window of about 0.4 ms [3] (sampling rate is 10 microsec) in increments of 20 samples, and the velocities were sought between 1000 and 7000 m/s every 10 m/s.

There are two possible sources of error to explain the differences in figure 3-5. First, the parameters used to obtain the semblance functions may differ between the automatic and the individual processing. Three semblance plots at the same depth (12250 ft) together with the array waveforms are shown in figure 3-6. The middle panel was generated using a window of correlation of 0.4 ms, the top one with a window of 0.2 ms and the one at the bottom right with a larger window of 0.8 ms. The compressional velocities picked at maxima from these three figures are 4940, 4930 and 4950 m/s, thus only a slight variation in velocities can be attributed to different lengths of correlation window.

The coherence method takes advantage of the array overcoming the limitations of noisy individual waveforms. In cases like the one depicted in figure 3-6 the waveforms by themselves have good signal to noise ratio and the main arrivals are clear. At 12250 ft, the automatic processing is off by about 180 m/s (4%) in the compressional velocity, and might be attributed to a low performance of the peak-finding routine, the second possible source of error. If this is indeed a pitfall in the automatic STC, this error would be worse in cases where signal to noise ratio is poorer or energy of relevant arrivals is weaker. In fact, there is a strong relation between low energy semblance functions and large variance in the automatic velocities respect to the control ones; an example of which is shown in figure 3-7. In these cases, an interpretative processing is required, taking into account the behaviour at close depths and other logs information.

The performance of the automatic picking is finally tested in some depths where

[3] in commercial processing time windows are usually 2 to 5 cycles of the dominant arrival frequency (Kimball, 1998), in this case a window of 0.4 ms represents about 4 cycles of the dominant frequency.

even in the presence of high coherence and clean waveforms, significant differences in the velocities are observed; an example of this is shown in figure 3-9.

Sometimes multiple, distinct peaks can be identified in the semblance plot, which can be interpreted as the shear or pseudo Rayleigh waves. For example, at 11200 ft, (here the borehole is circular), we can distinguish one peak at about 1.2 ms and 2980 m/s and a second one of less energy, at 2.2 ms and 2840 m/s (fig 3-10). It is possible that this second peak comes from the limitation of the semblance algorithm to handle dispersion (of the pseudo Rayleigh in this case) [4]. It also could be associated to the Airy phase of distinctive lower group velocity. However, it is also possible that the formation is anisotropic close to the borehole wall at this depth in which case, shear waves split into two polarizations, one travelling slower than the other (Tang et al., 1999).

Apart from errors in the determination of velocities when using either an automatic algorithm or some other method, there is still the issue of how reliable these velocities are in case irregular borehole conditions. We reduce the next analysis to six representative depths:

1.- Circular, nominal size borehole: as at 8280 and 11200 ft (figures 3-9 3-10 and 3-11). These depths serve as control cases to base the comparisons.

2.- Large circular borehole: as at 12440.5 and 11100 ft (figures 3-12 3-13 and 3-14). The borehole has a larger cross-sectional area than the nominal bit size (a diameter of about 16 in) but it is close to circular with eccentricity less than 1.1.

3.- Elliptical borehole: as at 12250 and 11000 ft (figures 3-6 3-7 and 3-8); the borehole is increased in one diameter and eccentricity is about 1.4 in both cases.

Circular Borehole

The little difference on borehole diameter between 11200 and 8280 ft (the borehole is about 0.7 inches larger at 11200 ft), is not expected to introduce significant variations. It can be observed in the waveforms, however, an apparent difference in the amplitude of some frequency components. Despite this, at both of these depths, the P head wave,

[4] this point is elaborated in the dipole data section.

the pseudo Rayleigh and the Stoneley arrival are easily identifiable. The velocities are similar, the formation at 11200 ft being only about 70 m/s faster in its compressional velocity, and 50 m/s faster in its shear speed.

The two examples for this case show conventional variations in their full-waveforms character that have to be related to differences in formation properties at both depths and not to borehole conditions. Comparing the signals of one receiver for both depths in the frequency domain (fig. 3-15) we first recognize the expected effect of the borehole guide on the source spectrum : the original source signal (all frequencies between 8 and 30 kHz excited equally) is broken up into a number of resonant peaks each of them associated to a mode cutoff frequency (Hearst et al., 2000). For both signals, approximately the same peaks are observed but at 8280 ft, frequencies above 10 kHz are more attenuated than at 11200 ft. Differences in attenuation properties at these two formations might account for such variations (Cheng et al., 1982).

Large Circular Borehole

At 12440.5 and 11100 ft the borehole conditions are quite different; the borehole diameter is about 17 and 15 in respectively. The waveforms reflect such conditions in the following way:

1.- Multiple pseudo Rayleigh modes: the cutoff frequency of the pseudo Rayleigh wave decreases with increasing borehole radius. As a consequence, more radial modes are observed in the same band of frequency (fig. 3-16); all of their low frequency components travelling with approximately the shear velocity. For the case modelled in figure 3-16, the radius is 1.5 times larger and the cutoff frequency of the 2nd. pseudo Rayleigh wave diminishes from approximately 12.3 kHz to 8 kHz. The next mode cutoff decrease is greater, of about 5.5 kHz [5]. In the same figure the case of a borehole only slightly large (as in 11200 ft), is included to show that differences respect to nominal case are negligible [6]. At 12440.5 ft, for example (fig. 3-12), several

[5]the program computes the roots of the characteristic equation on the denominator of the integral that describes the pressure response of the borehole to excitation by a point source (Paillet and Cheng, 1991). It was coded by Dr. Rama Rao at MIT.

[6]the modelling did not include the tool. The results when incorporating the tool (of diameter 3

of the pseudo Rayleigh modes are seen (with same moveout across the array).

2.- Stoneley energy decreases: the Stoneley wave amplitude decreases when borehole diameter is larger. The further the receivers are from the borehole wall the weaker this wave is (Bouchon and Schmitt, 1989). At 11100 ft (fig. 3-13, the Stoneley wave is not distinguishable probably because at the receivers position the borehole reaches 21 in.

Additionally, the borehole wall shape varies more sharply in the 11100 ft case than in the rest of the cases. One explanation for the 'noisy' character of the waveforms is that the abrupt changes of diameter act as reflecting boundaries in the travelling path of some of the borehole waves. These reflections may interfere destructively with the main arrivals. Bouchon and Schmitt (1989) found in their numerical modelling that a steep radius variation gives rise to a reflected Stoneley wave and an associated decrease in the amplitude of the transmitted wave (related to (2) above and shown in the VTA plots). Bouchon and Schmitt (1989) also investigated the effects of small scale variations in borehole diameter (rugosities) using a wide frequency band source and observed that the Stoneley mode as well as the pseudo Rayleigh, are somewhat delayed.

Elliptical Borehole

The clear separation of arrivals in the semblance plot at 12250 ft (fig. 3-9) is remarkable considering that the borehole is very non-circular (diameters 13 and 19 inches). Semblance, as well as energy of the arrivals in the VTA plot, seems unaffected contrary to what intution might suggest. A similar eccentricity of 1.4 is found at 11000 ft (fig. 3-7) and this depth shows the lowest energy semblance.

Further modelling is required to establish the exact effects of the borehole ellipticity, however based on the actual data and on comparisons with the circular case:

1.- The pseudo Rayleigh wave appears to be the most affected. Contrary to the increased energy of higher radial modes observed when the borehole is larger, it seems

5/8 in) are similar as if the borehole had a smaller effective radius, in agreement with Cheng and Toksöz (1981)

that the ellipticity reduces the energy of the pseudo Rayleigh wave. This is probably due to cancellation among the resonances of this particular borehole shape. Since it is not 'symmetric', the summation process is not necessarily effective in enhancing monopole modes and reducing dipole and higher modes. Both cases presented here show this behaviour.

2.- The P head wave and the Stoneley wave (unlike the circular large borehole cases), are both distinctive arrivals. This could be explained considering that one diameter remains close to the nominal size.

Nicoletis et al. (1990) and Randall (1991) found independently that ellipticity of the hole decreases the tube wave velocity. Randall (1991) reported a 2.3% decrease for an eccentricity of 2, and lower for weaker ellipticities. The velocity of the Stoneley wave at high frequencies did not show significant variations as we also realize here by comparing, for example, the data at 12250 ft and 11200 ft. The previous effects onto the tube-wave velocity would be probably observed by processing the low-frequency Stoneley dataset.

At 11100 ft and 11000 ft the P head wave arrival has anomolous high amplitudes. We suspect that this is related to a combination of the hole dimensions and tool off-centering [7].

In summary, the effects of changes in diameter are difficult to isolate mainly because the waves recorded are complicated functions of the fluid and formation properties, and the borehole radius. As far as the velocities are concerned, the compressional wave velocity is determined without major difficulty because the STC processing is not sensitive to amplitudes and the wave dives into the formation avoiding the effect of rugosities. The head waves travel within the formation and away from the borehole boundary (Paillet and Cheng, 1991). In contrast, the shear velocity is more affected by hole conditions. Even in cases when semblance finds distinctive moveout, elliptical

[7]The DSI tool was ran simultaneously with the OBDT tool. This last one acts as a centralizer since its two perpendicular arms align with the long and short axis of the borehole. Because of the configuration of the tool string there is a distance of about 30 ft between the position of the dipmeter arms, which determines the center, and the position of the source in the DSI. If the borehole changes diameter within this 30 ft, the tool might not be centralized respect to the conditions at the source-receivers locations.

hole shapes could be producing an averaging effect on the velocities.

3.2 Dipole Data

In fast formations monopole data contain shear refracted waves. However, shear velocity can also be inferred independently from the velocity of the flexural wave at low frequencies generated with dipole sources.

The dipole dataset analysed here is really a cross-dipole since it was recorded by firing alternating the upper and lower dipole sources and receiving also alternating at both, inline and crossline receivers. In this way, four sets of 8 traces each, are generated: upper dipole source - inline receivers, lower dipole source - inline receivers, upper dipole source - crossline receivers and lower dipole source - crossline receivers. The two middle sets are also referred as the cross-components. By "crossline receivers", we mean the hydrophone pairs oriented inline to the lower dipole source, whereas "inline receivers" correspond to the ones oriented inline with the upper dipole. In here, we deal only with the first and last set, referred hereinafter simply as upper and lower dipole.

The sampling interval is 40 μsec, and the sources operate at low frequencies (peak around 2 kHz). The phase difference introduced by the separation of the sources and the delay between firings is corrected for in the field (B. Sinha - Schlumberger-Doll Research, personal communication).

Similarly to monopole data, dipole waveforms are processed for velocity estimation using the semblance technique. STC is usually performed following time and frequency data windowing to isolate the flexural arrival and improve peak quality, in cases where, for instance, altered zones are present. However, the main limitation of coventional STC is in handling the dispersive character of the flexural mode (Kimball, 1998).

In practice, in order to account for the flexural dispersion, a pre-computed correction is included in the processing. The amount of correction is derived using a model dispersion that depends upon the signature of the source, the STC filter, the borehole

size and the shear slowness; this last parameter being an approximation since it is not known [8].

Processing nondispersively a dispersive wave results in an underestimation of velocity. Traditionally this was the case provided the sources excited more energy at frequencies where most of dispersion was found (around 3.5 kHz) (Kimball, 1998). As a consequence, the energy of the flexural mode was very low at the nondispersive frequencies and techniques available to process the data had to operate at a signal-to-noise disadvantage.

Nowadays however, and it is the case of the DSI, tools are designed to excite much lower frequencies, minimizing the dispersion and easing the limitations of nondispersive processing methods (fig. 3-17), which by the way, require much less computation time than their dispersive analogs (Kimball, 1998). Under ideal conditions, the implemented correction mentioned above should be enough to account for possible biases in DSI dipole data.

The flexural mode does not posses a theoretical cutoff but its excitation becomes extremelly small below a transition frequency, leading to an effective cutoff (Ellefsen, 1990). The transition occurs where the shear wavelength in the formation exceeds about 5 borehole diameters (Randall, 1991); in the case of figure 3-17 it would be around 1.8 kHz. Hence, the non dispersive range of the flexural mode is difficult to excite and measure.

Additionally, there are some situations where peak of excitation occurs at a frequency where the flexural mode is strongly dispersive. In well M, this is often the case given the deviations from nominal borehole size encountered. The effect of a circular but larger borehole diameter on the flexural wave is investigated in figure 3-18. The borehole diameter was increased from 12.8 in (shown in fig. 3-17), to 15 in and 19.7 in. The phase velocity at the peak frequency (2-2.25 kHz) for the largest bore (19.7 in, middle figure), is about 30% smaller than the low frequency limit of 2930 m/s, but it is only 2% off in the case of the 15 in diameter bore. However, if the fluid

[8] http://www.slb.com

velocity is decreased from 1500 to 1300 m/s [9], the error for the 15 in borehole climbs to 18%. Note that the current data represents a worst-case since in slow formations, the normal modes dispersion is less.

The 'shifting' of the spectrum towards more dispersive frequencies is caused because the effective cutoff frequency of the flexural wave decreases as the radius increases. For the case presented above, a borehole radius of 19.7 inches shifts the flexural cutoff to approximately 1.1 kHz.

Therefore, the performance of STC is expected to be sensitive to the actual borehole conditions as it was upon the limitations of older tools. We expect as well that the bias correction would account for some, but not all, of the errors driven by the nondispersive assumptions of the semblance method.

3.2.1 Quality Control of Dipole Shear Automatic Velocity

In figure 3-19 the shear velocities derived from the upper dipole data, using STC plus bias correction, as well as the previous monopole shear velocities are plotted for comparison in four intervals. In general, the two shear measurements agree over most of the section with a mean difference of 160 m/s. At some depths velocities differ significantly, with a maximum difference around 5290 ft, shown in the first panel of figure 3-19.

Zemanek et al. (1991) concluded that zones where monopole and dipole shear velocities did not agree corresponded to slow intervals, in which case, the dipole measurement was more reliable. To see if the same conclusion is valid for our data, we compared variable density monopole and dipole sections between 12100 and 12200 ft (figure 3-20) [10]. In the figure, we see how the flexural mode arrival is very definitive on the dipole section even in those intervals over which the monopole doesn't show distinct shear wave. It is clear from these plots that the results from processing dipole

[9]The velocity of oil is somewhat less than fresh water or brine, varying from 1 to 1.4 km/s (Hearst et al., 2000). The drilling mud in well M was oil-based but its velocity could vary above or below the velocity of water according to additives like gels or barite.

[10]This interval was previously presented as an example of low quality bands in the monopole data that were possible indicators of large attenuation- significant decreases of shear velocity or interference from sharp borehole wall.

data will be more reliable.

On the other hand, Kimball (1998) attributes differences between monopole and dipole shear velocities to the differences in resolution (as long as the dipole velocities are computed by dispersive processing). This explains the slight smoother character of the monopole velocity profile in comparison with the dipole, observed also in our data.

The implications of different frequency bands become specially relevant under the actual borehole conditions. Monopole signals have short wavelengths and therefore are able to resolve close to the borehole wall whereas dipole energy reaches deeper into the formation. If the borehole is damaged, the dipole waveforms would have more chance of registering the true formation shear velocity. The same would happen if the borehole is not damaged but under an anisotropic stress field. The previous disgressions rely on the fact that the pseudo-Rayleigh cutoff is much higher than that of the flexural wave but it does not exempt the dipole velocities to be influenced by the borehole deformations as we will discuss later in this section.

A third cause that could be responsible for discrepancies between monopole and dipole velocity measurements is the presence of intrinsic anisotropy in which case monopole data could be averaging slow and fast velocities provided its symmetric characteristics. According to the automatic proccesed upper and lower dipole velocities, there are many places in the section where both measurements (in perpendicular directions) differ (fig. 3-21). Moreover, the delay between waveforms is easily identifiable by inspection (fig. 3-21).

If the differences in shear velocity in perpendicular directions is indeed the result of intrinsic anisotropy and not of errors in acquisition or processing, crossdipole data need to be rotated in order to align the dipole orientation with the principal axes of anisotropy. In this way, the velocity determination would be unbiased by properties at intermediate angles. Because the tool rotates in its way up, data rotation needs to be performed at each depth. This explains why both velocity profiles cross and none of them is consistently the fastest or slowest.

In order to validate the performance of the bias corrected STC velocities, some

control points are selected, similarly to what was done with the monopole data. At these control points, velocities are computed by two methods: standard semblance (non dispersive, in time) and a variation of semblance in frequency, that allows one to pick the dispersion relation of the flexural wave (Nolte et al., 1997). The velocity at the effective cutoff frequency corresponds to the shear velocity.

The first method is exactly the same applied to the control points of the monopole data; the second method requires that the flexural wave is isolated, then over a frequency range, several slowness at each frequency step are tried until the one that produces maximum energy is found [11].

In figure 3-22 the results are compared. With the exception of few points, the velocities obtained with the dispersive processing are faster, as expected (Kimball, 1998), the mean of the difference being about 190 m/s.

The standard semblance method is not accurate for dispersive waves since it treats all frequencies equally, independently on the non uniform excitation of these components (Block et al., 1991). In general, velocity-time maps from semblance exhibit two or more peaks at different velocities, connected by ridges and blurred more or less depending upon the noise level (Kimball, 1998). In time, the blobs look streched and sometimes as if dispersive (fig. 3-23). The maxima does not correspond any more to the shear velocity.

Although a dispersive analysis is the correct approach to determine shear velocities from flexural waves, this method has the shortcoming in practice of being very sensitive to the energy content, therefore at frequencies where energy is low, or 'noise' is present, the performance is also low (fig. 3-24 and fig. 3-25). In addition, if, as in our case, the borehole presents enlarged diameter, the resolution close to the corresponding flexural cutoff (lower than in the nominal radius case), becomes still more critical preventing any reasonable picking.

The effects of different borehole sizes was demonstrated through a numerical solution in figure 3-18 and examples from the data are shown in figure 3-26. In this

[11] The dispersion analysis used here was coded by Dr. Beltram Nolte and Dr. Xiaojun Huang at MIT.

figure, the dispersion curves corresponding to two upper dipole frames are plotted. Formation velocities are similar at both depths, however the diameter is almost 6 inches larger at 12250 ft in the orientation of the upper dipole. Hence, the nondispersive part of the flexural wave is displaced towards lower frequencies in comparison to the smaller bore case at 8280 ft. Low energy at these frequencies prevent an accurate picking of the shear velocity at 12250 ft.

At 12250 ft the borehole has a more elliptical shape with eccentricity of about 1.4. Randall (1991) proved through numerical modelling, that the flexural mode corresponding to one dipole orientation is fairly insensitive to the conditions at the perpendicular direction (as long as dipoles are oriented with minimum and maximum axis). In his tests, eccentricities larger than 1.5 start to show some departures in the shorter direction response respect to the dispersion of a circular borehole of the same radius. In all cases, the flexural mode shifts towards lower frequencies as if the borehole were effectively larger. The equivalent occurs for the flexural dispersion corresponding to the longer diameter dipole orientation.

For the purposes of determining velocity from flexural waves and following the results of Randall (1991), we can expect that the effects of having a large circular borehole of, for example, 16 in diameter, are harsher than those upon the flexural wave oriented with the shorter axis of an elliptical bore that has, for instance, diameters 18 and 13 in.

Finally we compare in figure 3-27 the automatic velocities, computed with the bias correction after semblance, and our velocities derived with the direct dispersive technique.

The velocities from dispersion analysis are not consistently higher or smaller than the ones bias corrected but in average, when faster, the difference reaches about 370 m/s. Where the dispersive velocities are slowly the mean difference is somewhat less (300 m/s). These variations represent a possible error of about +/- 13%. Similarly to the monopole P velocities, the automatic shear processing show a maximum 'error' of 40% in particular locations. The automatic velocity is in most of the depths analysed, higher than the ones obtained with conventional semblance (not shown), indicating

that the bias correction is precise although not necessarily accurate.

The upper dipole shear velocities obtained by STC with bias correction every 0.5 ft are the ones used in the following computation of the elastic parameters in spite of the several uncertainties here presented, yet it is out of hand a reprocessing at the same vertical resolution.

3.3 Sonic-Derived Porosity

An acceptable approximation of porosity for rocks, sufficiently compacted (transit times below 100 $\mu sec/ft$), can be obtained from sonic data through Wyllie's empirical equation (Hearst et al., 2000):

$$\Phi = (\Delta t_{log} - \Delta t_{ma})/(\Delta t_f - \Delta t_{ma}) \tag{3.1}$$

where Δt_{log} is the transit time of the compressional wave, Δt_{ma} is the trasit time in the rock matrix and Δt_f is the transit time in the saturating fluid.

This porosity calculation from transit times is a rearranged time-average relationship which interrelates velocity and rock parameters (fluid velocity and mineral composition), for a fairly wide range of porosities, and when the fluid content is mainly brine. The validity of the time-average relationship is connected with Gasmman's theory in the sense that the variation of velocity with pressure can be neglected at depths of deeper sediments in situ.

The porosity computed by equation 3.1 for well M is shown in figure 3-28 where Δt_f was assumed to be 200 $\mu sec/ft$ and Δt_{ma} 48$\mu sec/ft$ above 6800 ft, and 44 $\mu sec/ft$ below. The porosity computed from the density log (eqn. 2.3) is plotted for comparison, although we already established its low reliability.

Porosities in Chimana formation are in average 15% with a maximum value of 35%. Barranquín formation shows lower porosities on the order of 11% and in agreement with the sedimentological observations.

It is common practice to crossplot the ratio Vp/Vs vs. compressional wave trav-

eltime. Since Δt_c is related to the inverse of porosity, this procedure gives an idea of the degree of consolidation or the effective stress of the formations crossed. In general, Vp/Vs increases as compaction decreases (Δt_c increases) for water-saturated sands. On the other hand, dolomite, limestone and dry or gas-bearing sands show constant Vp/Vs ratio at different porosities (Schlumberger, 2002c).

In figure 3-29, well M shows very low Vp/Vs ratios and Δt_c [12], indicating that these formations are well consolidated.

3.4 Sonic-Derived Density

In the previous chapter the unreliability of the density log was established based on the effects of the borehole irregular diameter. On the other hand, density of the column rock at each depth, as well as P-wave and S-wave velocities, is required in the computation of elastic constants and some geomechanical parameters like the vertical stress.

Gardner et al. (1974) were concerned with the primary properties governing the occurrence of seismic reflections, namely, P-wave velocity and density, and in how these parameters related under different rock composition and environmental conditions. These authors recognised the importance of porosity, mineral composition, intergranular elastic behavior and fluid properties, depending on overburden and fluid pressure, microcracks, age and depth of burial.

From a large number of laboratory and field observations of different brine-saturated rock types (excluding evaporites), density fairly relates to P-wave velocity through (Gardner et al., 1974):

$$\rho = 0.23V^{0.25} \tag{3.2}$$

where V refers to compressional wave velocity in ft/sec and ρ to bulk density in g/cm^3.

[12] unconsolidated shales may show Vp/Vs on the order of 3.5 with Δt_c as high as $150\mu sec$.

The corresponding bulk density for well M computed from equation 3.2 is shown in figure 3-30. In order to verify its validity, figure 3-31 shows the agreement with the original density log in an area where borehole diameter is preserved.

3.5 Elastic Constants

Elastic moduli can be derived from several methods and, according to the type of measurement, the resultant constants are classified as static or dynamic. The static elastic properties are defined as those measured by static deformation in an open system. The dynamic properties are broadly referred to those derived from wave propagation measurements, regardless of whether rocks are in an open or closed system (Wang, 2000). The distinction between open or closed system is related to the possibility of the pore fluid to flow out when the system is subjected to compression (or to flow in when subjected to expansion).

Static and dynamic values differ in general. In some cases, as for example when experiments are carried out at atmospheric or low pressures, the difference may reach several hundred percent (Wang, 2000); the static values are less than the dynamic ones.

The causes of the discrepancy include several factors, some of them related to the type of measurement itself and others dealing with particular rock features. Among the first group are, strain amplitudes, frequencies, system type and uncertainties in the measurements themselves. As far as the latter are concerned, if the static and dynamic moduli differ by 10% or less in hard rocks, and by 25% or less in soft rocks, no further correction of the measured dynamic moduli is necessary in estimating the static one, considering the measurement uncertainties which could amount +/- 5% to as high as +/- 25% in the worst case (dynamic-laboratory, soft rocks) (Wang, 2000).

The geometry and density of pores, cracks, fractures and grain boundaries seem to be an important factor to explain the difference between static and dynamic elastic properties (Simmons and Brace, 1965), (Cheng and Johnston, 1981), but it is now mostly accepted that strain amplitude causes the major effects.

Although in-situ reservoir rocks deform nearly statically, it is not always possible to obtain directly the static elastic moduli required to describe this deformation. Even in the case of core availability, it is not possible to measure elastic properties for the whole well column. On the other hand, full-waveform sonic logs along with density logs provide continuous data to derive dynamic moduli. Corrections are then needed to convert these wave-derived dynamic properties to their static equivalents in order to applied them in engineering applications, for example, borehole stability, hydraulic fracturing design, reservoir compaction and so forth.

Up to date, there is not a universal relationship or unique way of deriving static values from dynamic measurements. Several empirical relationships are conventionally applied but care must be taken since those were obtained for particular rock types and conditions.

In the following, the dynamic elastic moduli are computed from the wave velocities and density values of well M; some corrections of these data are also discussed. The static elastic moduli are calculated next, once a particular empirical relationship is justified as appropiate based on well M formation characteristics.

3.5.1 Dynamic Moduli

Dynamic elastic moduli are determined by wave propagation measurements, done on cores in laboratory, or directly in wells through sonic logs. Laboratory methods include the resonance method, where dynamic Young's modulus is determined by measuring the resonant frequency of a vibrating bar, and the seismic pulse method where piezoelectric transducers of compressional and shear waves emit pulses whose travel times are measured.

Due to the absence of laboratory data, elastic constants for well M are initially derived from the full-waveform acoustic logs. The relationships between elastic moduli

and V_p, V_s and ρ are:

$$E = \rho V_s^2 \frac{3V_p^2 - 4V_s^2}{V_p^2 - V_s^2} \tag{3.3}$$

$$\nu = \frac{V_p^2 - 2V_s^2}{2(V_p^2 - V_s^2)} \tag{3.4}$$

$$K = \rho(V_p^2 - \frac{4}{3}V_s^2) \tag{3.5}$$

$$G = \rho(V_s^2) \tag{3.6}$$

where K, G, E and ν refer to bulk, shear, Young modulus and Poisson ratio respectively.

In dynamic measurements strains are very small, typically less than 10^{-6}. Under these low strain amplitudes, the deformation process of flat pores, cracks and grain boundaries is elastic and as a result the rock seems to be less compressible or deformable.

Frequency is another important factor given that in dynamic experiments they can be quite high: around 10 kHz in logs and 500 kHz in ultrasonic tests. Wave velocities are required to be corrected provided elastic waves are dispersive, mainly in fully fluid-saturated rocks. Biot's theory if often used in this correction, but in general, it is of little significance, 1-3% (Wang, 2000), in comparison with for example, measurement uncertainties.

If dynamic elastic properties are obtained from sonic logs there is one necessary correction prior to deriving their static equivalents. Such correction consists in converting the dynamic properties measured in a closed system to the moduli that would correspond to an open system, had the pore fluid been unconstrained, as in static experiments. The modified dynamic bulk modulus K_d, that is, the dry (or gas saturated) modulus, can be computed from the fluid saturated bulk modulus (K) by means of the reverse Gassmann equation (Wang, 2000):

$$K_d = K - \frac{K_f(1 - \frac{K}{K_m})^2}{(1 - \frac{K_f}{K_m})\Phi - \frac{K_f}{K_m}(1 - \frac{K}{K_m})} \tag{3.7}$$

where K_f refers to the fluid bulk modulus, K_m to the matrix and Φ is the porosity.

Since the shear modulus is not affected by fluid saturation, the correction for Young's modulus is:

$$E_d = \frac{9GK_d}{3K_d + G} \tag{3.8}$$

Assuming an oil-based mud saturating fluid, $K_f \simeq 1.7$GPa (Gardner et al., 1974), and a quartz matrix, $K_m \simeq 25$GPa, K_d and E_d are calculated for well M. The resultant dynamic elastic constants are shown in figure 3-32.

Bulk modulus in undrained conditions (liquid saturated) are higher than their equivalents in drained conditions (gas or dry): the stress is now supported also by fluid and not solely by the rock frame, therefore rock is stiffer and deforms less. As observed in figure 3-32, the maximum decrease in Young's modulus is about 15 GPa.

Particularly in well M, differences between dry and saturated constants are small, probably because low porosities and lack of pore fluids. Presence of tight gas sandstones would cause same behaviour. The dynamic Young's modulus ranges from 14 GPa to 85 GPa with a mean value of 48 GPa.

The large variation of parameters in depth is suspicious. Poisson ratio negative values and as high as 0.45 confirm that the velocities are incorrect in many places.

3.5.2 Static Moduli

Static elastic properties of rocks are measured by standard stress-strain tests in an open system. Opposite to dynamic tests, static measurements are done essentially at a frequency close to zero. Strain gages, in one or several directions, are attached to core samples. Confining pressures, or uniaxial loading, are then increased in steps while the gages measure the deformation.

Stress-strain curves for many reservoir rocks are not always perfectly linear because of permanent deformation. Static tests are characterised by high strain amplitudes, typically greater than 10^{-2}, that cause that flat pores, cracks and grain boundaries suffer anelastic deformation; as a result, the rock seems to be more com-

pressible (Wang, 2000). Cheng and Johnston (1981) explain the difference between static and dynamic bulk moduli based on microcrack density: the ratio K_s/K_d decreases with increasing crack porosity.

When cores or rock mechanics laboratory facilities are not readily available, as in well M case, static elastic properties have to be derived from dynamic measurements. Several correlations have been suggested. For instance, Cheng and Johnston (1981) obtained a ratio K_s/K_d varying from about 0.4 at atmospheric pressure to 0.9 at pressures above 200 MPa. This behaviour was observed in rocks such as sandstones of different porosities and cementation degree, granite and tuff.

Empiral Relationships between Static and Dynamic Moduli

Logarithmic relationships between static and dynamic Young's modulus have also been suggested (van Heerden, 1987), (Eissa and Kazi, 1988). Test specimens in van Heerden (1987) included sandstones, quartzites and others which have been classified as hard rocks ($E_s \geq 15$ GPa). Under the same classification, Wang (2000) incorporated data from Yale and Jamieson (1994) (carbonates) and found the linear correlation :

$$E_s = 1.15E_d - 15.20 \tag{3.9}$$

The corresponding bulk modulus correlation is:

$$K_s = 1.29K_d - 11.63 \tag{3.10}$$

The same paper establishes another relation for soft rocks data obtained from several sources, however, data are more scattered than in the previous case.

For weak rocks, static and dynamic moduli (K and E) show significant differences, even for dry rocks, which have been found to be strongly dependent on stress and strain (Fjaer, 1999). Observations indicate that a major cause is that failure occurs continuously (crushing of asperities in the grain contacts) as stress and strain changes.

Fjaer (1999) develops quantitative relations between static and dynamic bulk and Young's moduli, based on the assumption that for small increments of stress ($\Delta\sigma$), the non-elastic deformation change ($\Delta\epsilon_{ne}$) is proportional to the stress change.

$$\Delta\epsilon_{ne} = 3P\Delta\sigma \tag{3.11}$$

Since the non-elastic deformation is supposed to vanish for small amplitude strains, dynamic moduli are only involved in the elastic part of the volumetric strain increment ($\Delta\epsilon_e$),

$$\Delta\sigma = K_d\Delta\epsilon_e \tag{3.12}$$

The total static volumetric strain increment ($\Delta\epsilon$) can be written as:

$$\Delta\epsilon = \Delta\epsilon_e + \Delta\epsilon_{ne} = \frac{\Delta\sigma}{K_s} \tag{3.13}$$

Substituting equations 3.11 and 3.12 in 3.13 gives the relation between static and dynamic bulk modulus:

$$K_s = \frac{K_d}{1 + 3PK_d} \tag{3.14}$$

where P is a proportionality constant depending on the hydrostatic pressure and the stress history. P is inversely related to stress because as the external stress increases, more and more asperities are crushed and cracks close, causing the contact area to broaden so that stress concentration is reduced. From equation 3.14, it is clear that when P approximates zero $K_s \simeq K_d$, however it is important to keep in mind that these relations were based on experiments on soft sandstones subjected to comparatively low pressures; at higher stress levels, P may eventually start to increase probably due to grain crushing and pore collapse. The general linear relationship between $1/P$ and applied stress was found to be caracteristic of most of the rocks investigated but particular differences were atributed to porosity and cementation

specific for each material.

For uniaxial loading tests, the derivation of the relation for E is similar if the non-elastic deformation term is separated between normal and shear deformation which is assumed proportional to the total strain. The proportionally constant in this case named F, is a measure of sliding cracks. Finally,

$$E_s = \frac{E_d}{1 + PE_d}(1 - F) \tag{3.15}$$

where P in all directions has been assumed equal.

Well M Static Moduli

Knowing that rocks in well M are mainly consolidated and low-porosities sandstones E_d is estimated using equation 3.15. Static bulk modulus is computed from equation 3.14. Observed discontinuity in depth of failures in well M suggests that it should exist a significant variation of rock stiffness and it seems appropriate to correlate zones of failures with weaker (brittle) rocks.

The selection of P and F values introduces other uncertainties. Here, P is assumed to be a twentieth of the fractional porosity, a function chosen to make sure that K_s/K_d remains within reasonable limits. F is closely related to shear failure, a value of 1 meaning global failure is reached. F was assumed zero.

In figure 3-33, bulk and Young's static moduli are compared with their dynamic counterparts. The average ratio K_s/K_d for the whole section is 0.52 while E_s/E_d is approximately 0.6. According to Cheng and Johnston (1981) such ratios correspond to pressures of about 30 MPa in their sandstones experiments.

Using other relationships to get the static values, like the ones described in equations 3.9 and 3.10 (not shown) produces very high ratios, on the order of 0.9, and twice the variance.

Few investigations have been done concerning the correlation between static and dynamic Poisson's ratio and there is not consistency to define if ν_d is greater or less than ν_s (van Heerden, 1987); for well M, $\nu_d = \nu_s$ is assumed.

3.6 Rock Strength

Mechanical properties of rocks are controlled by cracks, bedding, fractures, cement and grain cohesion. Compressive or shear strength refers to the resistance of the rock to compression. Tensile strength is the resistance against pulling apart. In an uniaxial compression test, a cylindrical core sample is loaded axially to failure. Conceptually, the compressive strength (C_0) is measured at the peak stress, defined as the maximum load sustained by a specimen, divided by its cross sectional area. Failure begins at C_0 and occurs progressively beyond this point.

Laboratory tests to measure directly the mechanical strength of rocks are difficult to perform since such properties are highly sensitive to individual characteristics of experiments and sample conditions. As a result, a great variation of strength for similar rock types (in porosity and composition) can be found in the literature (Zoback, 2001). For example, sandstones and limestones have compressive strengths as low as 10 MPa and as high as 700 MPa. Shales tend to be weaker (although not in a brittle sense), and their strength is commonly below 120 MPa.

In general, rock compressive strength is inversely related to porosity and directly related to confining pressure, Young's modulus and clay volume. Based on such observations, some attempts have been made to obtain C_0 indirectly from logs or other laboratory measurements (Coates and Denoo, 1981), (Fjaer, 1999), (Jizba, 1991). For the estimation of C_0 in well M, we apply the empirical relationship:

$$C_0 = 50000EK(0.008V_{sh} + 0.0045(1 - V_{sh}))\frac{cos\theta}{1 - sin\theta} \tag{3.16}$$

where E and K are given in 10^6 psi and are static values, and V_{sh} is the shale volume as before. θ refers to the angle of internal friction, which is a function of rock consolidation. For consolidated sandstones, θ is approximately 42° (Ruiz and Graterol, 2002). Assuming a smaller angle, as for instance 30°, decreases the compressive strength in about 30%. Relationship 3.16 is a modified expression that includes the effect of compressibility in original observations made from uniaxial compression experiments (Coates and Denoo, 1981).

Rocks are much less resistant to tension than to compression. As a general rule, tensile strengths are about 10% of the compressive strength, but in practice they approach zero (Zoback, 2001).

In figure 3-34, the estimated compressive and tensile strengths in well M along with the borehole long diameter are plotted.

Disregarding anomalously low and high values as, they are likely the result of errors propagated from the velocity estimation, compressive strength varies mostly between 30 and 160 MPa.

The estimated values are reasonable considering that porosities are low and a high degree of diagenesis has been reported in Barranquín formation from the sedimentological analysis. For similar porosity sandstones, compressive strengths from laboratory core measurements, range widely between 50 and 200 MPa (Zoback, 2001). Samples of Berea sandstone, for example, exhibit strength around 122 MPa at 10 MPa confining pressure [13]. Fitting these data to Mohr-Coulomb failure criteria suggests an angle of friction of about 39°.

The sensitivity of strength to clay content was recently studied by Jizba (1991) and, according to this analysis, we realize that applying equation 3.16 to the whole section in well M, is not quite correct. Jizba (1991) found, in confined uniaxial compression experiments, that the strength in sandstones with clay volume fractions less than 17% was independent from clay content but strongly dependent on confining pressure and porosity. Strength of shaley sandstones and shales was sensitive to confining pressures and clay content.

The same study reports compressive strengths in sandstones as high as 775 MPa at 50 MPa confining pressure, for a sandstone of porosity 1%, and about 500 MPa for one of porosity 9%. More importantly, sandstones exhibited linear elastic deformation and almost no ductile deformation prior to rupture. Rupture occured in a brittle manner with a sudden decrease in slope in the stress-strain curve.

Shaley sandstones, on the other hand, behave somewhat differently. Strengths

[13] this experimental result was learnt from a technical presentation by New England Research, Inc. at the Earth Resources Laboratory, MIT.

are lower than in sandstones; for instance, a sample of 5% porosity and 31% clay shows peak stress at about 320 MPa (at 50 MPa confining pressure). The stress-strain curve of these rocks indicated a nearly linear elastic behaviour followed by some ductile deformation, prior to rupture.

The ductile deformation observed in shales was larger and associated with work hardening. For instance, a sample of 63% clay and 5% porosity, showed up to 75% of additional axial strain prior to rupture, at the same confining pressure as before. The strength of this rock was about 200 MPa.

In well M data, specifically below 8000 ft, we observe a correlation between low percentage of clay and failures, (or larger borehole diameters) (fig. 3-35). Faster rocks correspond generally to cleaner sandstones, and hence, to higher values of strength. Therefore, faster, less shaly, and "stronger" sandstones are the rocks that comparatively fail more in borehole M. The experimetal work presented in Jizba (1991) supports the explanation:

Although shales have lower mechanical resistance than sandstones, they have the property of supporting high stress levels by building strains without failure. Sandstones, on the other hand, require high differential stresses but exhibit brittle behaviour, meaning that they fail after just a small stress increment beyond the yield point. Shales undergo plastic flow and other processes as shear banding, dislocations propagation, and compaction.

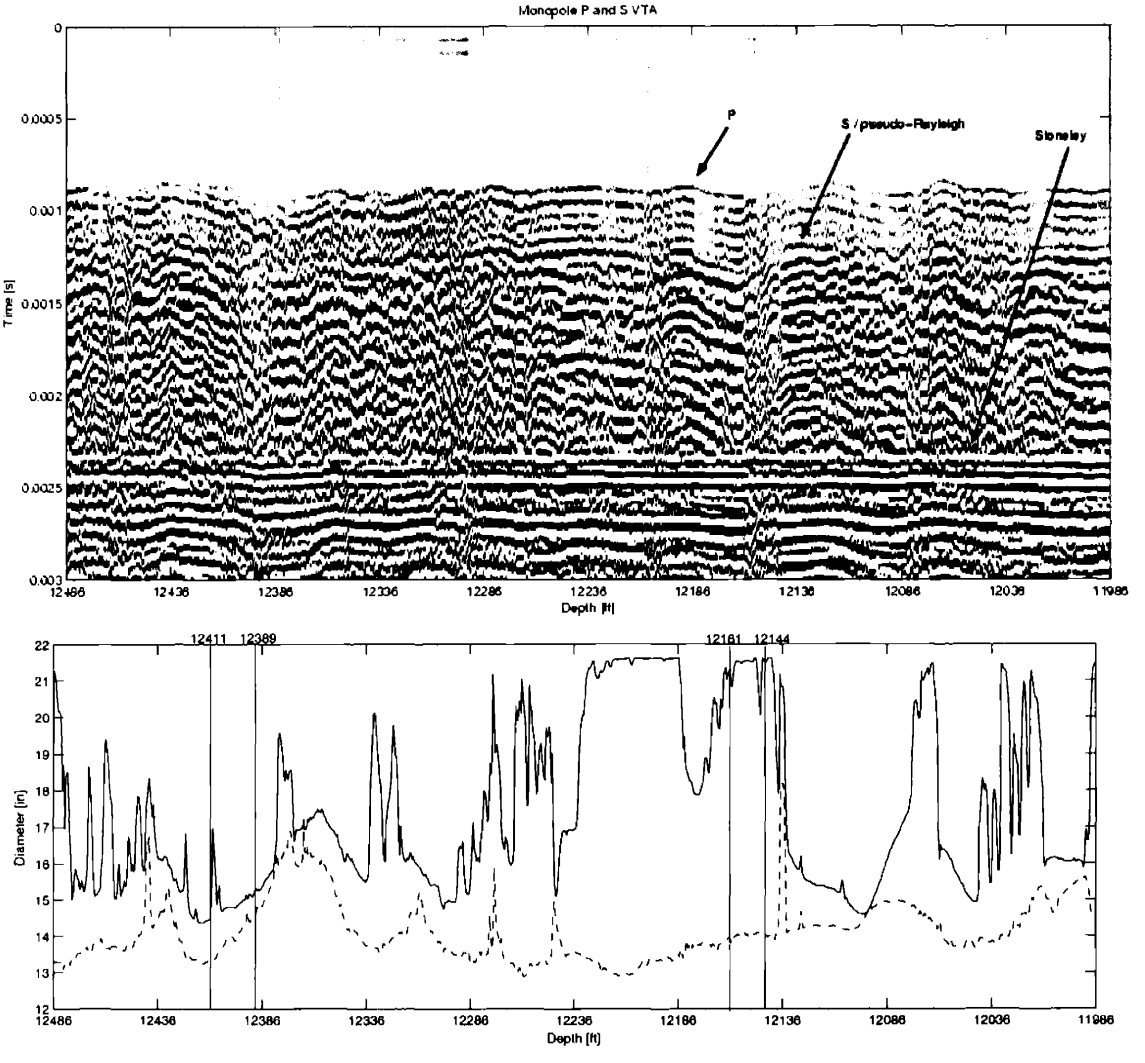

Figure 3-1: Full waveform data from the Monopole P and S mode between 11986 and 12486 ft in variable density. Only the near receiver for every source position (every 0.5 ft) is plotted. Maximum (solid) and minimum (dash) diameters of the borehole are plotted at the bottom figure. In the top figure, the P arrival is distinguished at about 0.85 ms, the shear head wave and the low frequency component of the pseudo Rayleigh wave arrive at around 1.2 ms. The Stoneley wave is the constant in depth arrival at about 2.4 ms. At the bottom figure the intervals 12389-12411 ft and 12144-12161 ft are delimited to indicate the regions where the shear wave arrival is not distinct in the VTA plot.

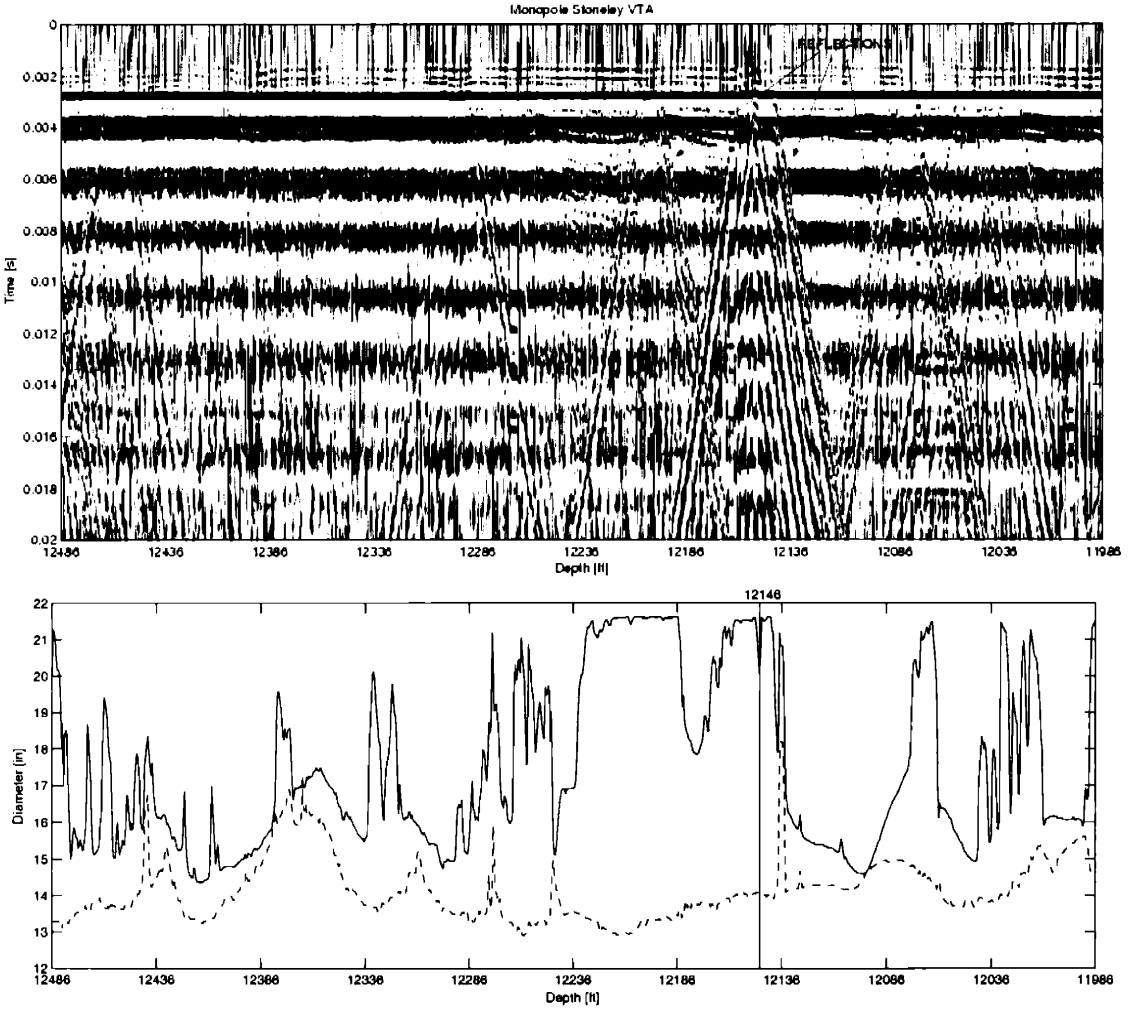

Figure 3-2: Full waveform data from the Monopole Stoneley mode between 11986 and 12486 ft in variable density. Only the near receiver for every source position (every 0.5 ft) is plotted. The signal is extensively affected by reflections coming from abrupt changes of borehole diameter as for example, at 12146 ft. This depth is indicated at the bottom figure where maximum (solid) and minimum (dash) diameters are plotted.

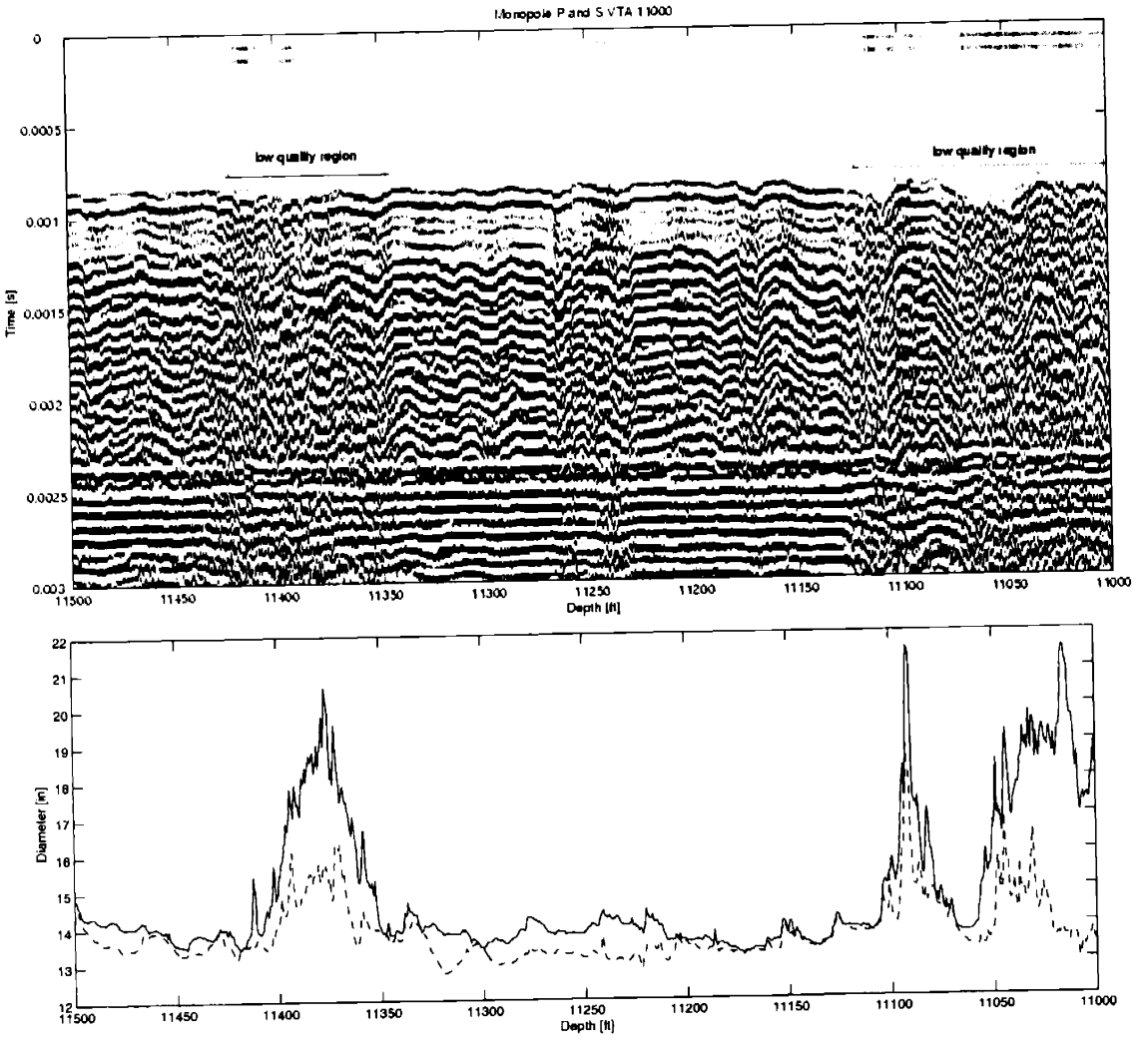

Figure 3-3: Full waveform Monopole P and S mode between 11000 and 11500 ft in variable density. Bottom figure shows maximum and minimum diameter of the borehole. Low quality zones in the VTA plot are associated to regions where borehole departures from nominal size.

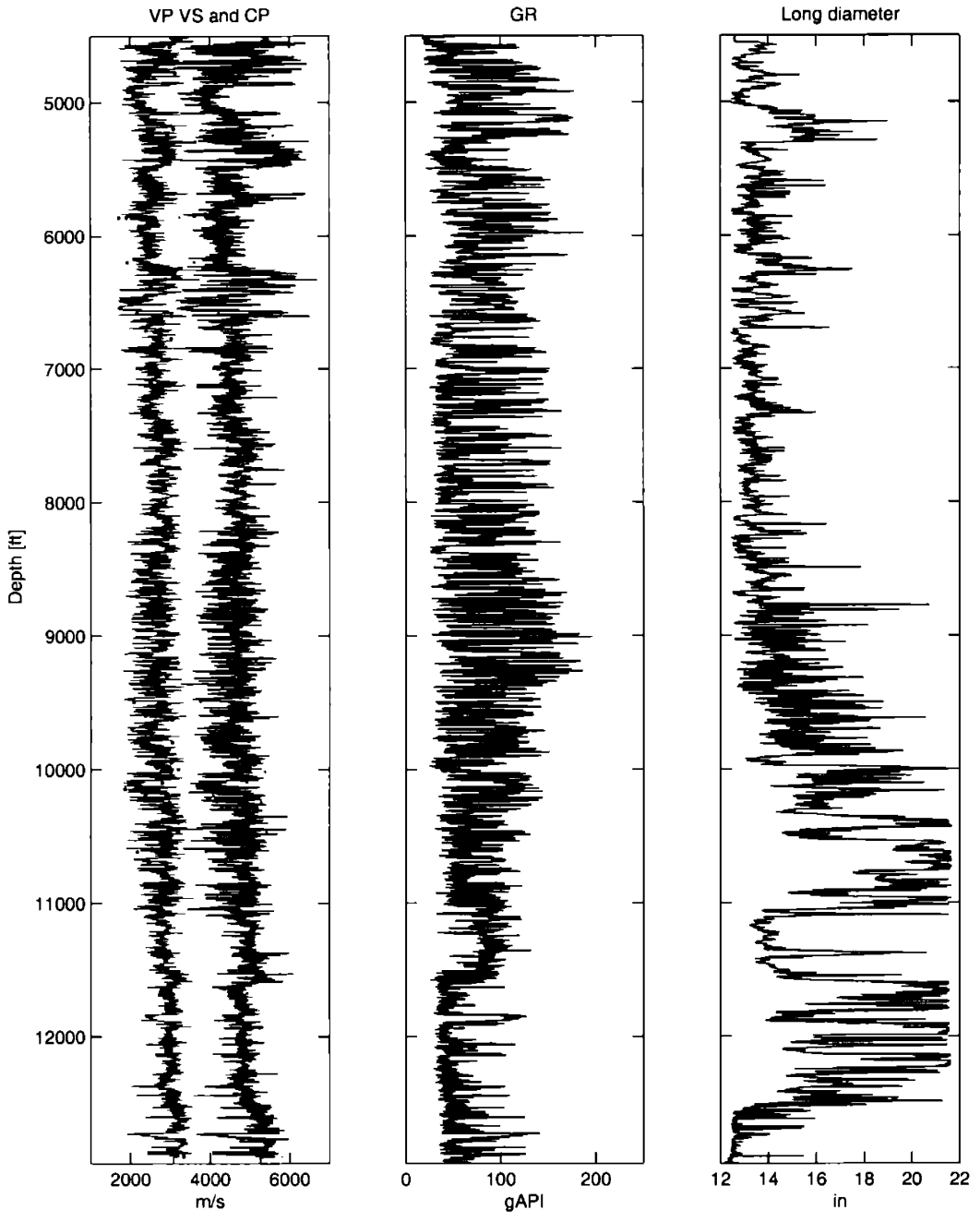

Figure 3-4: Automatic P and S velocities obtained from STC processing of monopole P and S data. The middle panel displays gamma ray data and the rightmost panel shows the maximum borehole diameter. The dots on the first panel mark the velocities at the control points. The rapid variations in depth of V_p and V_s agree with the fine lithological changes observed in the gamma ray. Shalier formations are relatively slower.

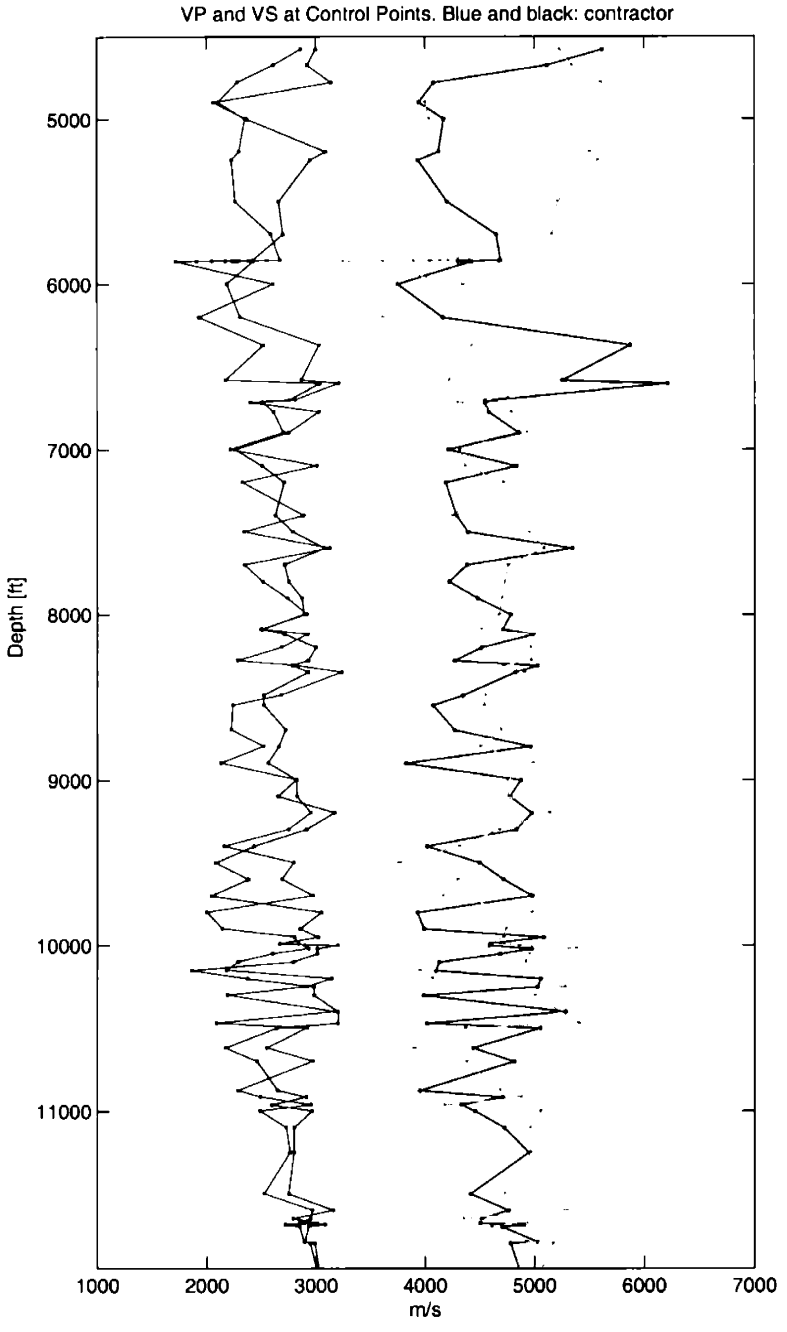

Figure 3-5: P and S automatic (blue/black) and in-house (red/green) processed velocities at control points. Both are based on semblance processing of monopole P and S data. Differences in compressional and shear velocities are in average 460 m/s and 315 m/s respectively. These values represent about 10% of possible error in the automatic velocities, however at some places, as for example 5250, the difference reaches 36%.

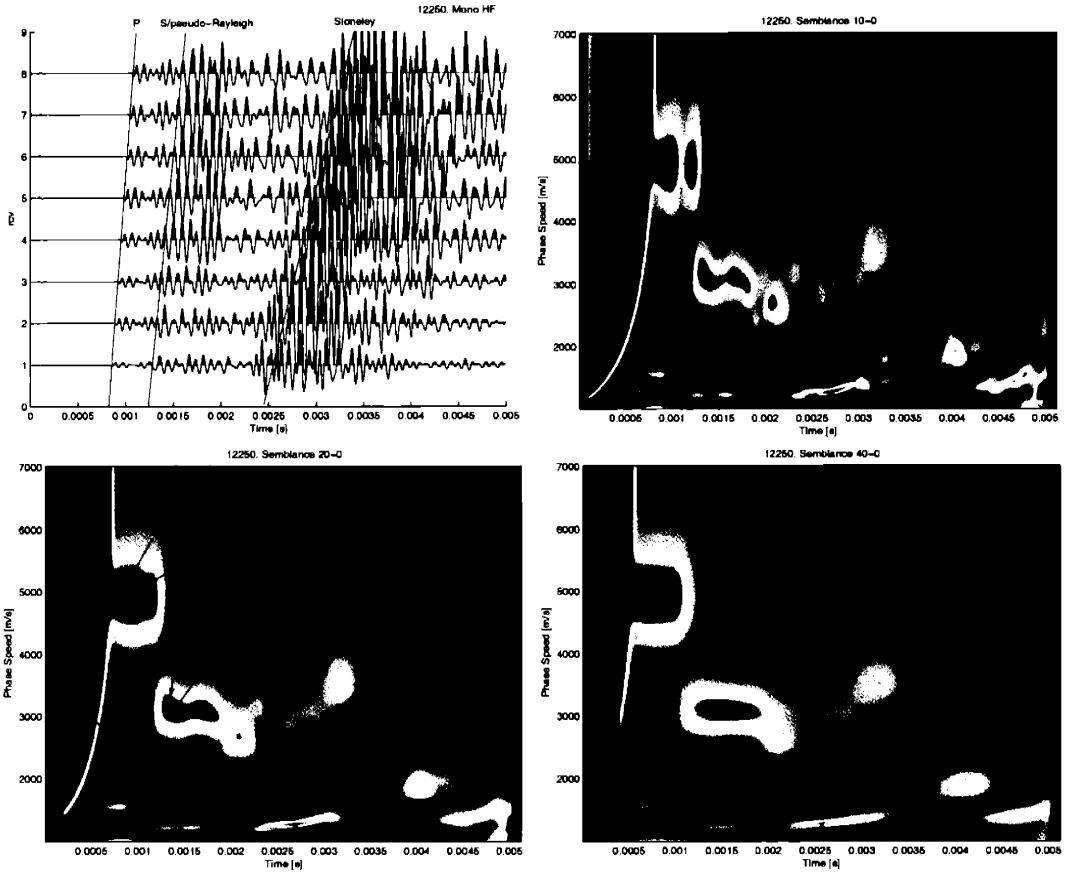

Figure 3-6: Errors due to processing parameters; example frame at 12250 ft. This frame is also an example case of non-circular borehole. From top to bottom, waveforms, semblance computed with time window of 0.2 ms (top right), with time window of 0.4 ms (below the waveforms) and with time window of 0.8 ms. On the waveforms, the main arrivals are indicated and their corresponding maxima in the semblance plots are also marked. The maximum labeled "electrical signal" refers to the instrumental pulse recorded at early times at all receivers. The monochromatic character of this signal produces high correlation at almost every moveout. The P and S automatic picks are indicated in the semblance plot (0.4 ms) to show that errors are larger than mismatches introduced by differences in semblance parameters. P velocity picked in these semblance plots varies only by 10 m/s while difference with automatic one amounts 186 m/s.

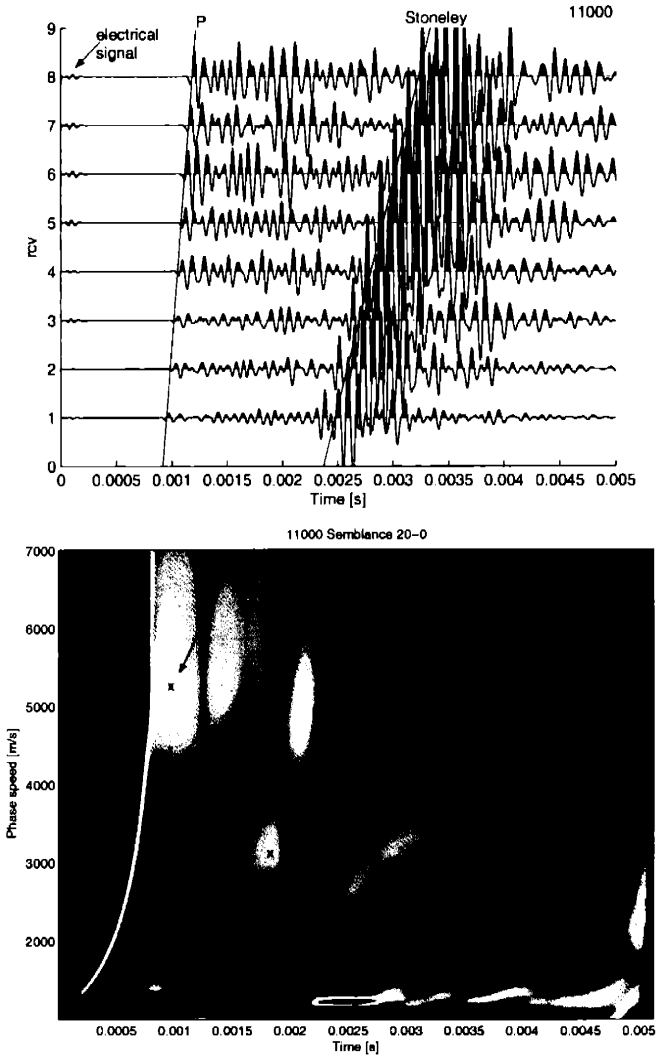

Figure 3-7: Frame at 11000 ft. Example of low energy semblance/interpretation required and case of non-circular borehole. Waveforms are on the top figure and semblance plot on the bottom. Errors in picking are accentuated given the lack of distictive maxima. The automatic P velocity at this depth is 4458 m/s and the shear velocity is 2487 m/s, about 500 m/s slower than what this plot suggests.

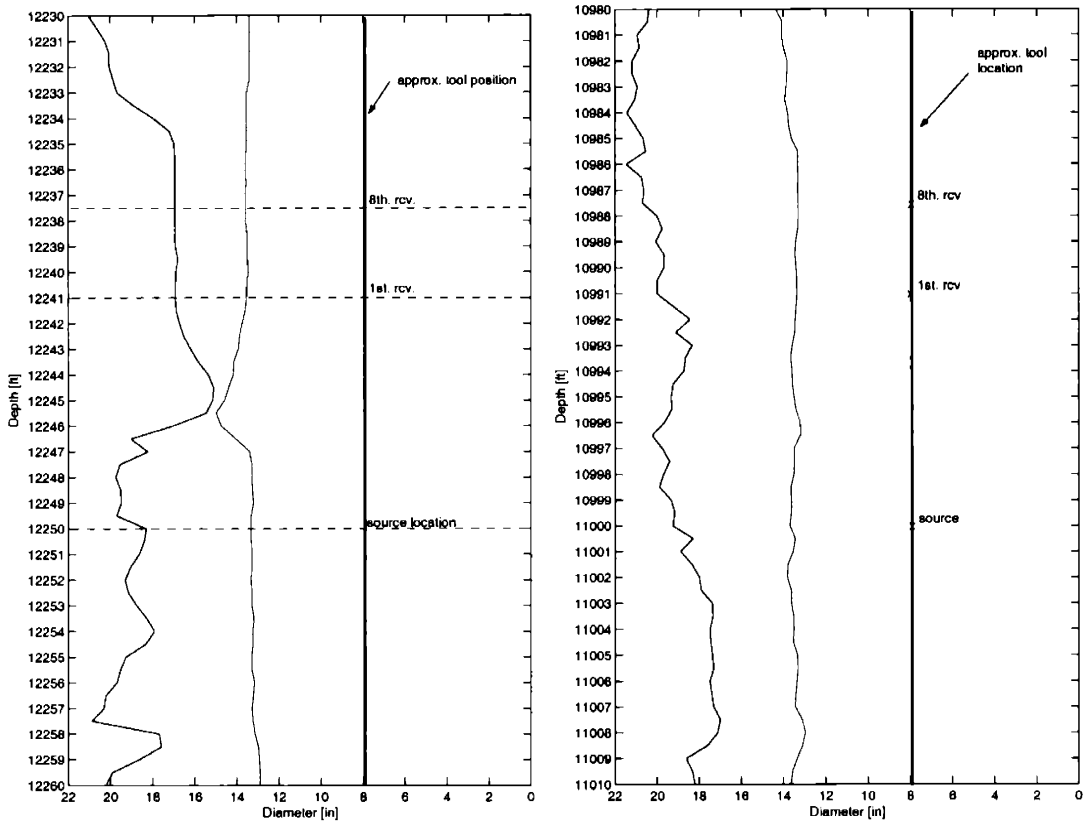

Figure 3-8: Non-circular borehole cases. On the left, diagramatic location of the tool, source and receiver levels and the borehole maximum (black) and minimum (blue) diameter for the frame 12250 ft. On the right panel, same for 11000 ft. Eccentricity is about 1.4 in both cases.

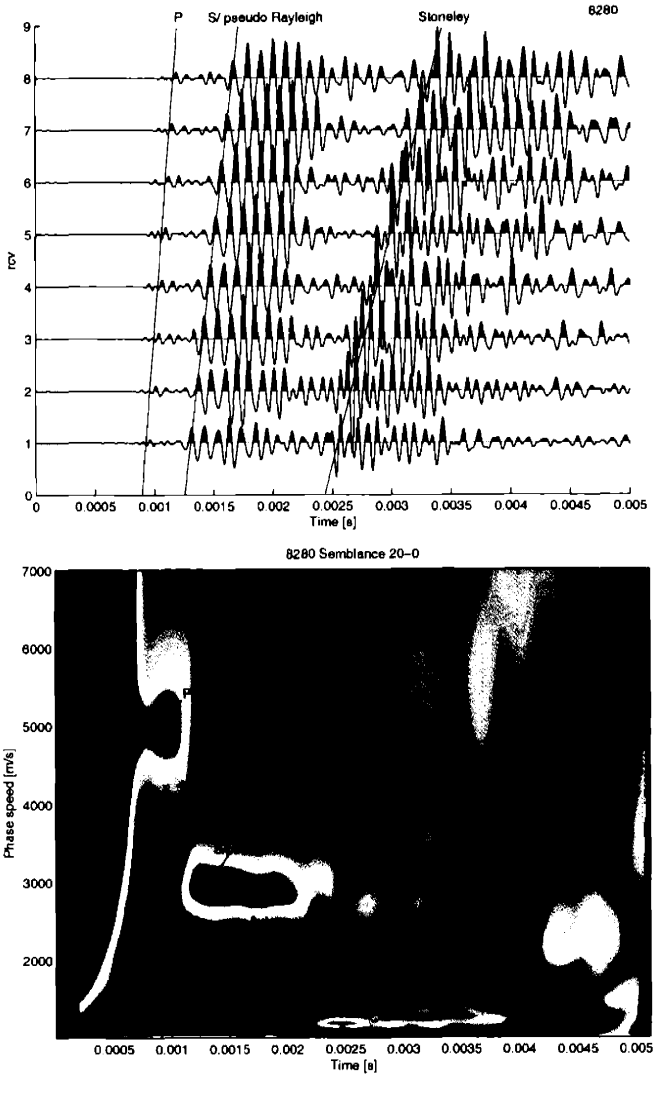

Figure 3-9: Frame at 8280 ft. Example of high energy semblance/low performance of automatic STC and case of circular/nominal size borehole. On the top figure, the waveforms and on the bottom, semblance plot for this frame. Difference in P and S velocities respect to automatic one is about 700 m/s.

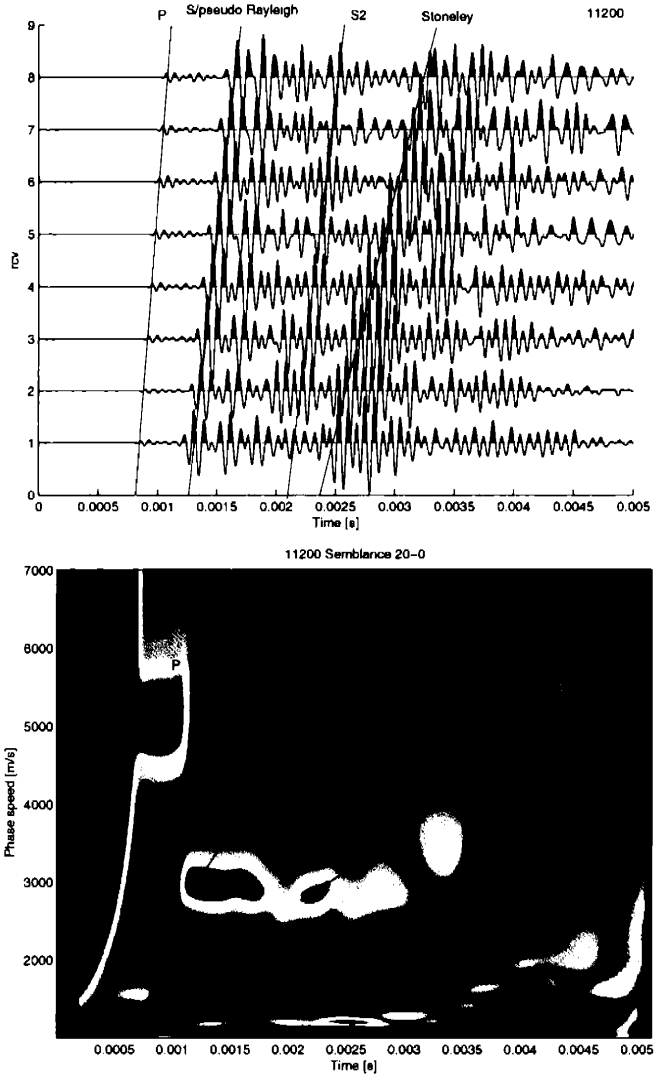

Figure 3-10: Semblance and waveforms from frame 11200 ft. Example of circular/nominal size borehole. The semblance plot (bottom) shows high correlation for the P, shear refracted/pseudo Rayleigh and Stoneley arrivals which are also indicated in the waveforms (top). There is a secondary energy maximum at around 2.2 ms showing a slightly slower moveout than the shear wave, this arrival is labeled "S2" in the waveforms to distinguish it from the fastest shear wave and indicating possibly anisotropy.

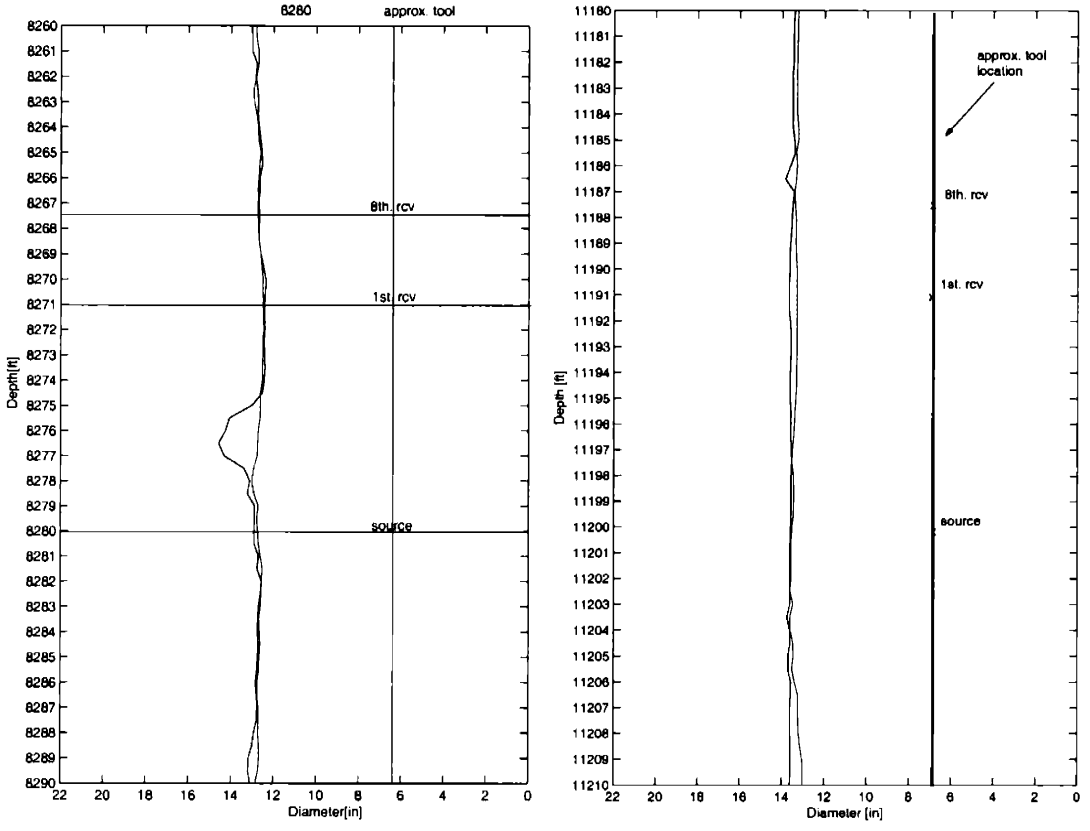

Figure 3-11: Circular borehole cases. On the left, diagramatic location of the tool, source and receiver levels and the borehole maximum (black) and minimum (blue) diameter for the frame 8280 ft. On the right panel, same for 11200 ft.

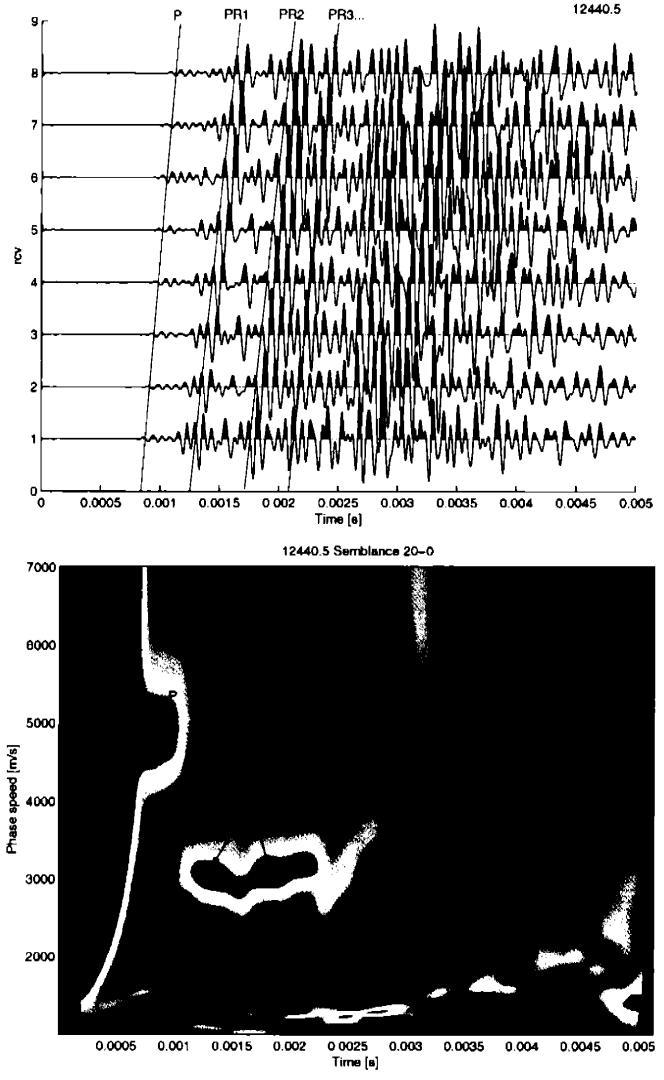

Figure 3-12: From top to bottom, waveforms and semblance for frame at 12440.5 ft. Example case of near circular/large radius borehole. The effect of multiple pseudo Rayleigh modes when borehole is large is observed in the waveforms where several arrivals with same moveout can be distinguished after the compressional refracted wave (PR1, PR2, PR3). The theoretical explanation of this phenomenum is depicted in figure 3-16 and explained in the text. Note as well how the Stoneley wave is less distinctive than in the circular cases.

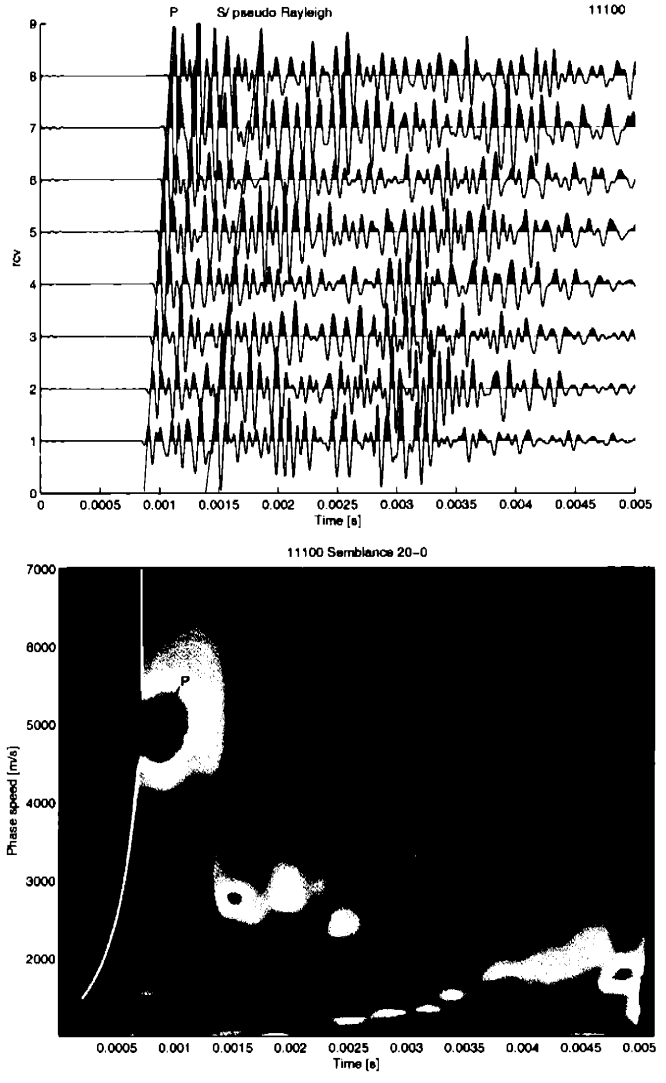

Figure 3-13: From top to bottom, waveforms and semblance for frame at 11100 ft. Example case of near circular/large radius borehole with maximum diameter of 16 in at the source level and eccentricity less than 1.1. The low energy of the Stoneley wave is more critical in this case than at 12440.5 ft probably because receivers are further from the borehole wall.

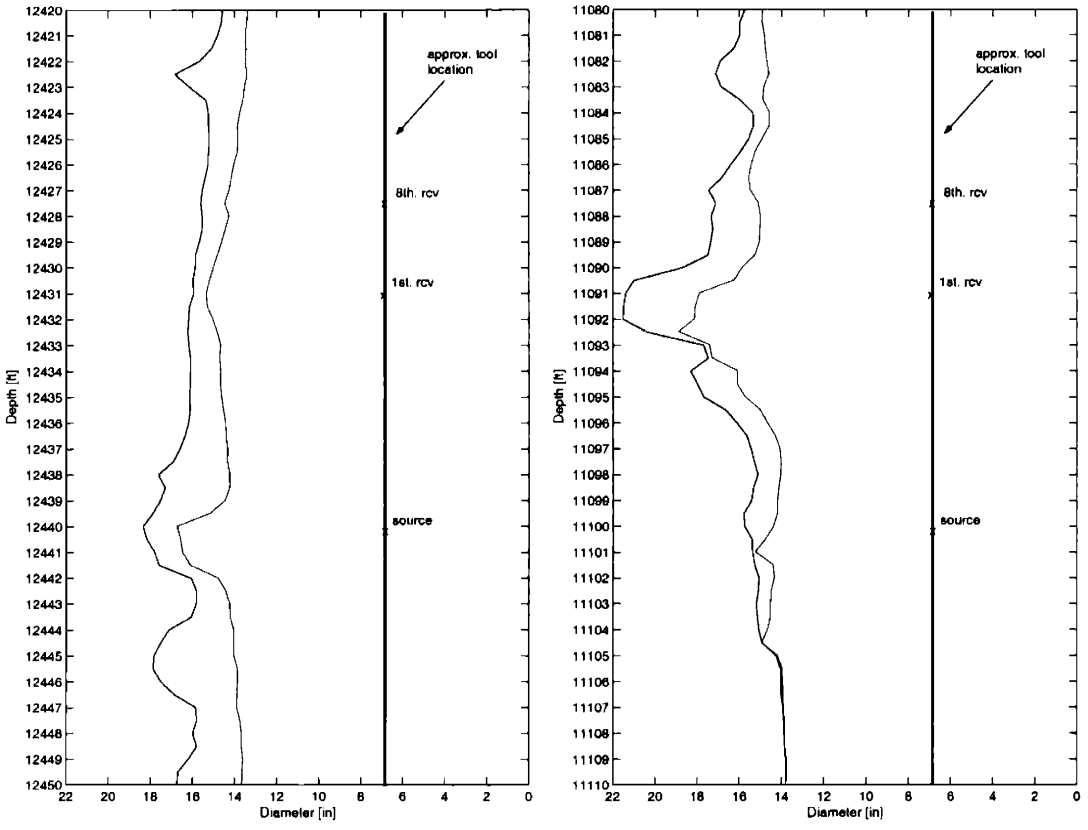

Figure 3-14: Near circular/large diameter borehole cases. On the left, diagramatic location of the tool, source and receiver levels and the borehole maximum (black) and minimum (blue) diameter for the frame 12440.5 ft. On the right panel, same for 11100 ft. Eccentricity in both cases is less than 1.1. In the right figure it can be seen that diameter changes sharply in the source-receiver length; this could be responsible for the noisy character of the waveforms and the anomalous high amplitude of the P wave relative to later arrivals (see fig. 3-13).

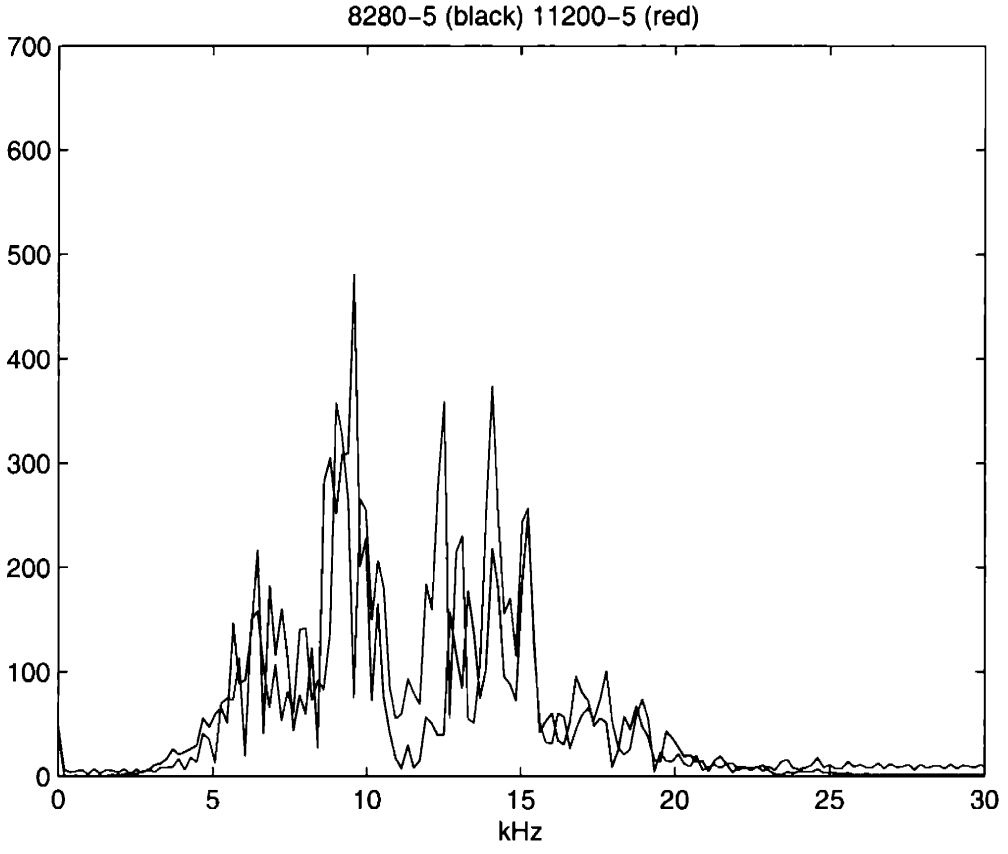

Figure 3-15: Spectra of fifth receiver for the 8280 (black) and 11200 ft (red) monopole high-frequency frames. At both depths borehole geometry is similar and circular/close to nominal size. Frequencies between 10 and 15 kHz are more attenuated than in the 11200 ft case which could account for the differences in character observed at the waveforms (figures 3-9 and 3-10). Formation is slightly faster at 11200 ft.

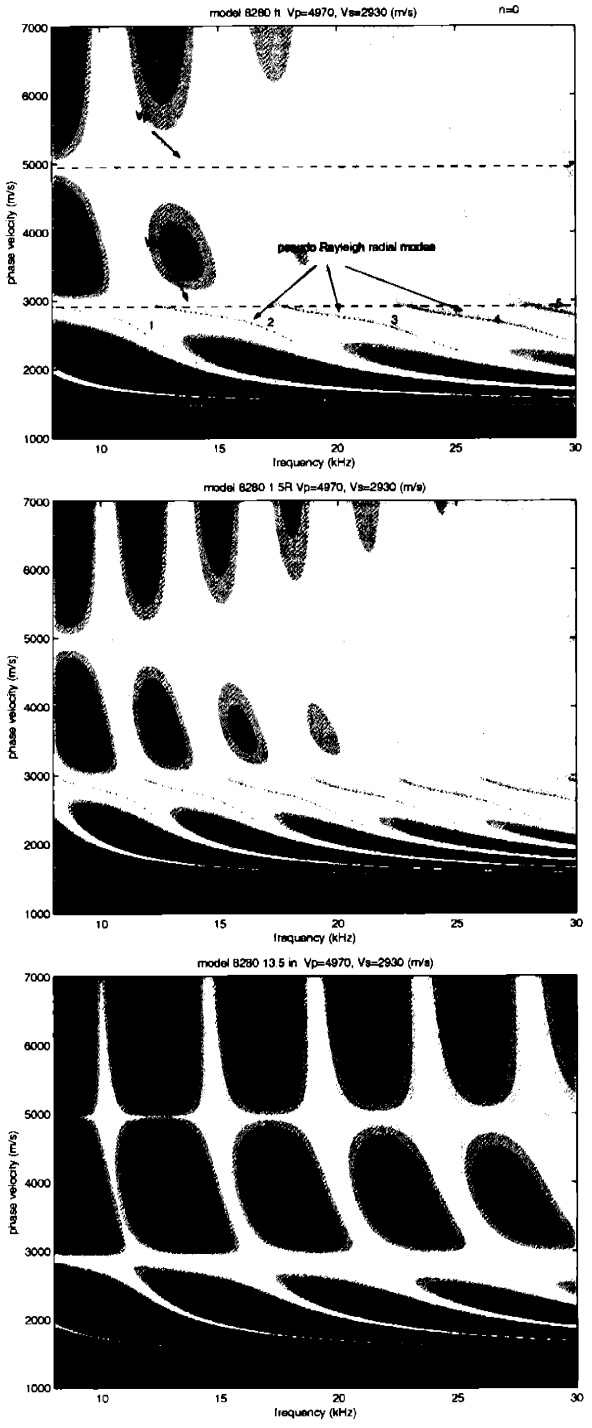

Figure 3-16: Effects of borehole radius on pseudo Rayleigh cutoff frequency. The figures show a map in the phase speed - frequency plane of all the monopole modes (azimuthal order zero and all radial variation). Middle pannel shows results for the same case depicted at the top but with a radius 1.5 times larger. Bottom figure corresponds to a radius 1.06 times larger. The colors towards blue indicate the solutions: refracted P wave, the fluid wave and the normal modes. All radial pseudo Rayleigh modes (labelled 0, 1, 2 etc), approach the shear velocity at their low frequency end. In the largest borehole increased number of modes is observed.

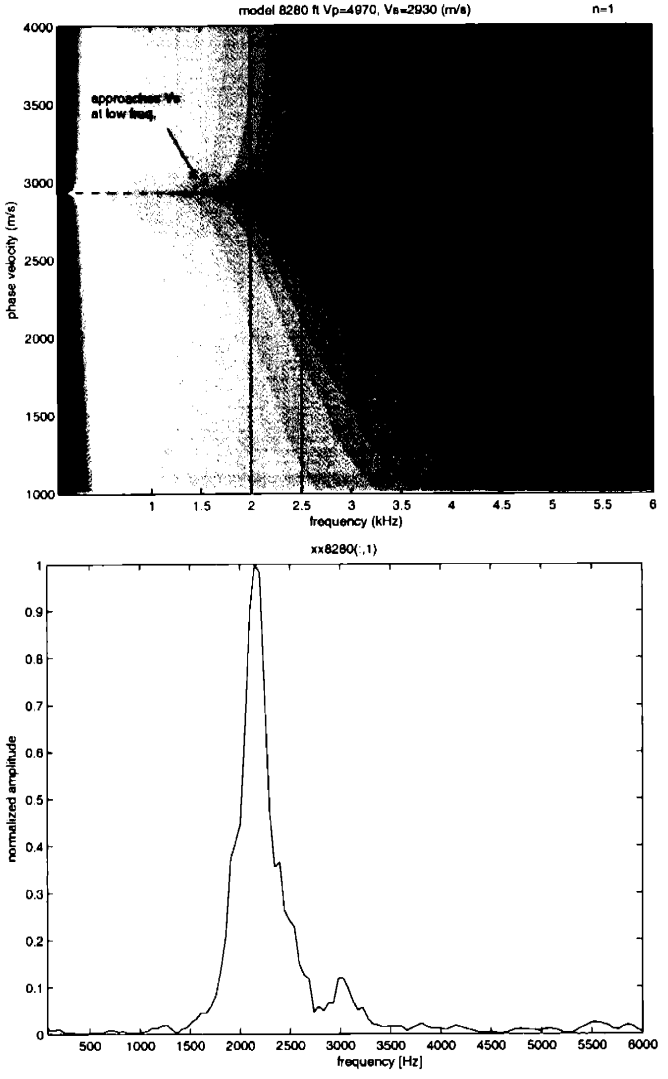

Figure 3-17: On the top, a numerical solution of the flexural wave dispersion for the conditions found at 8280 ft. The fluid velocity and density were assumed as 1500 m/s and 1000 Kg/m^3. In this figure, colors towards blue correspond to roots in the phase speed -frequency plane of dipole modes (azimuthal order 1 and all radial variation). At the bottom, the actual spectrum of the first receiver from the upper dipole frame at 8280 ft shows that the excitation peak is between 2 and 2.25 kHz. This band of frequency is marked in the top figure to point out that it coincides with the range where the wave is nondispersive.

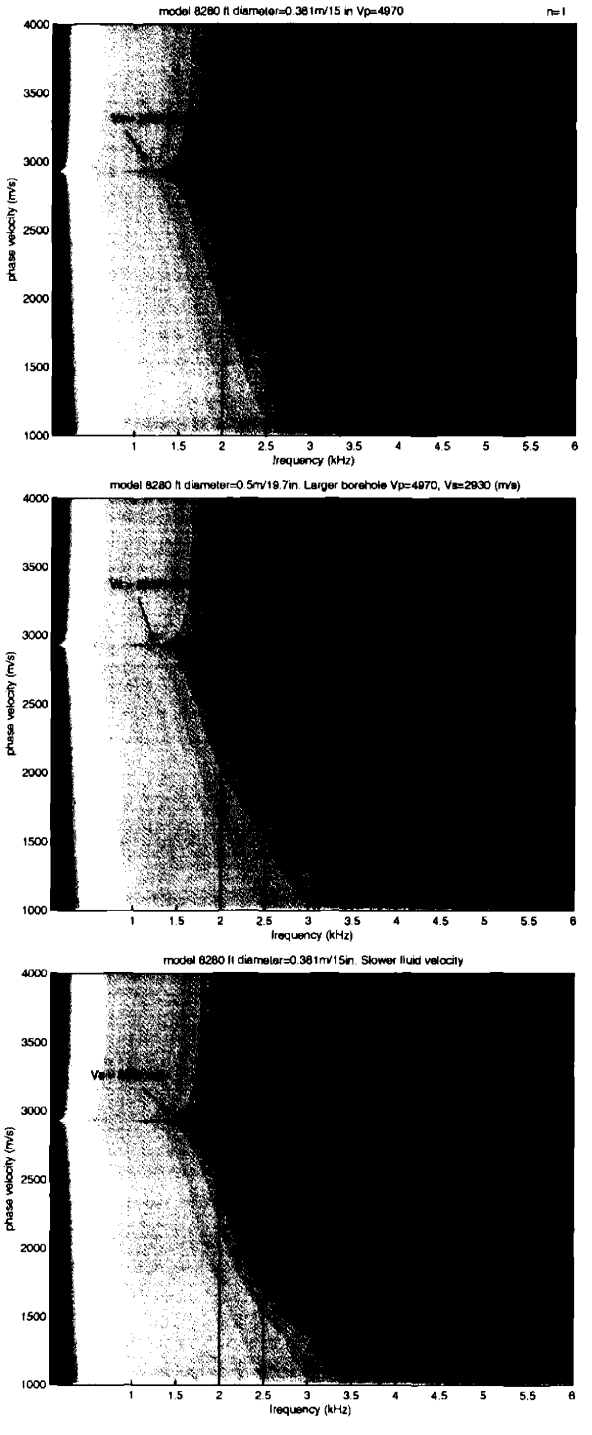

Figure 3-18: Effects of borehole radius and fluid velocity on flexural wave dispersion. Top figure: flexural dispersion for a borehole of diameter 15 in, formation velocities as at 8280 ft and fluid velocity 1500 m/s. Middle figure: same but borehole is circular with a larger diameter of 19.7 in. Bottom figure: same as top one but fluid velocity is 1300 m/s. In larger boreholes (middle figure), the effective cutoff frequency of the flexural wave is decreased similar to the effect of slow fluids (bottom figure). At frequencies with higher energy (2-2.5 kHz) the flexural wave is dispersive, hence, non dispersive velocity estimations would be incorrect.

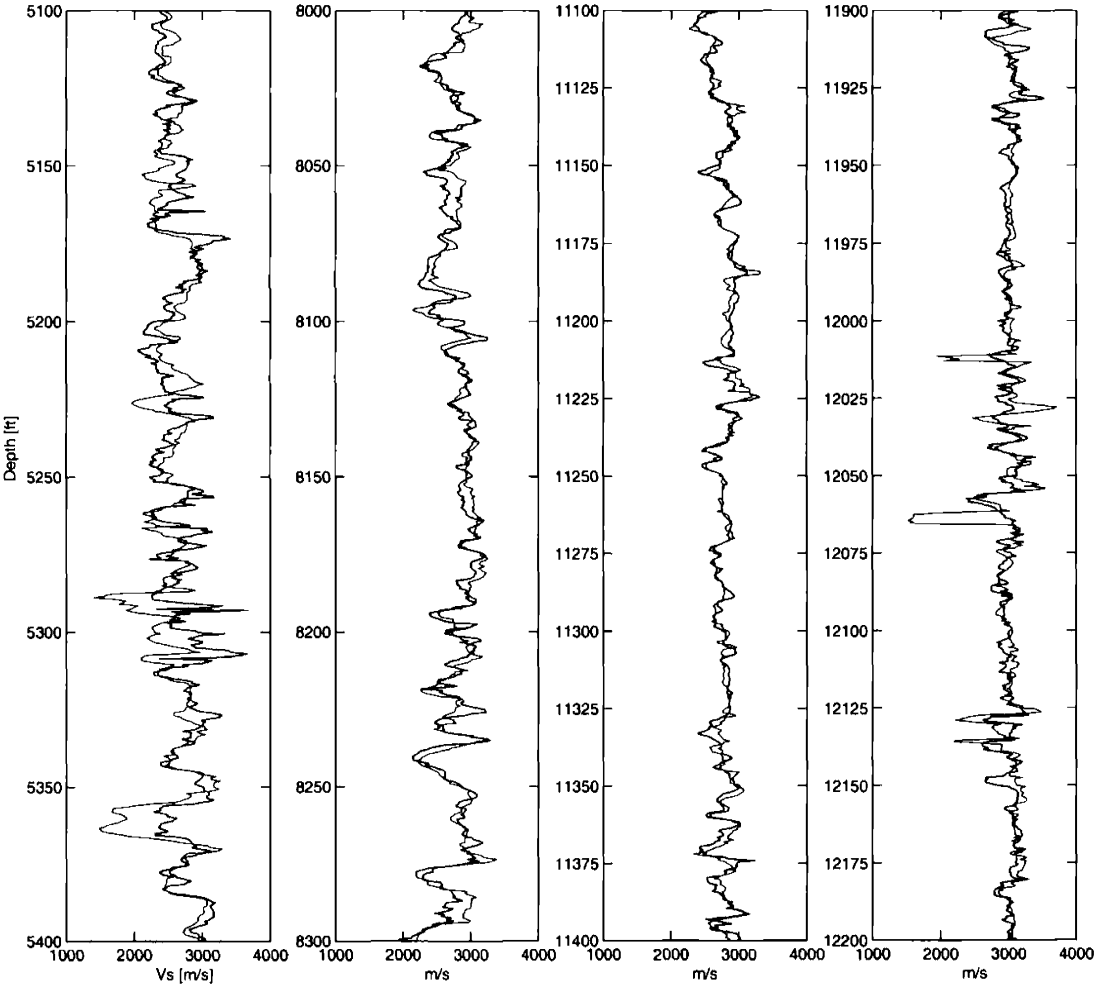

Figure 3-19: Automatic upper dipole (blue) and shear monopole velocities in four intervals. From left to right: 5100-5400 ft, 8000-8300 ft, 11100-11400 ft and 11900-12200 ft. In average dipole and monopole velocities differ by about 5%.

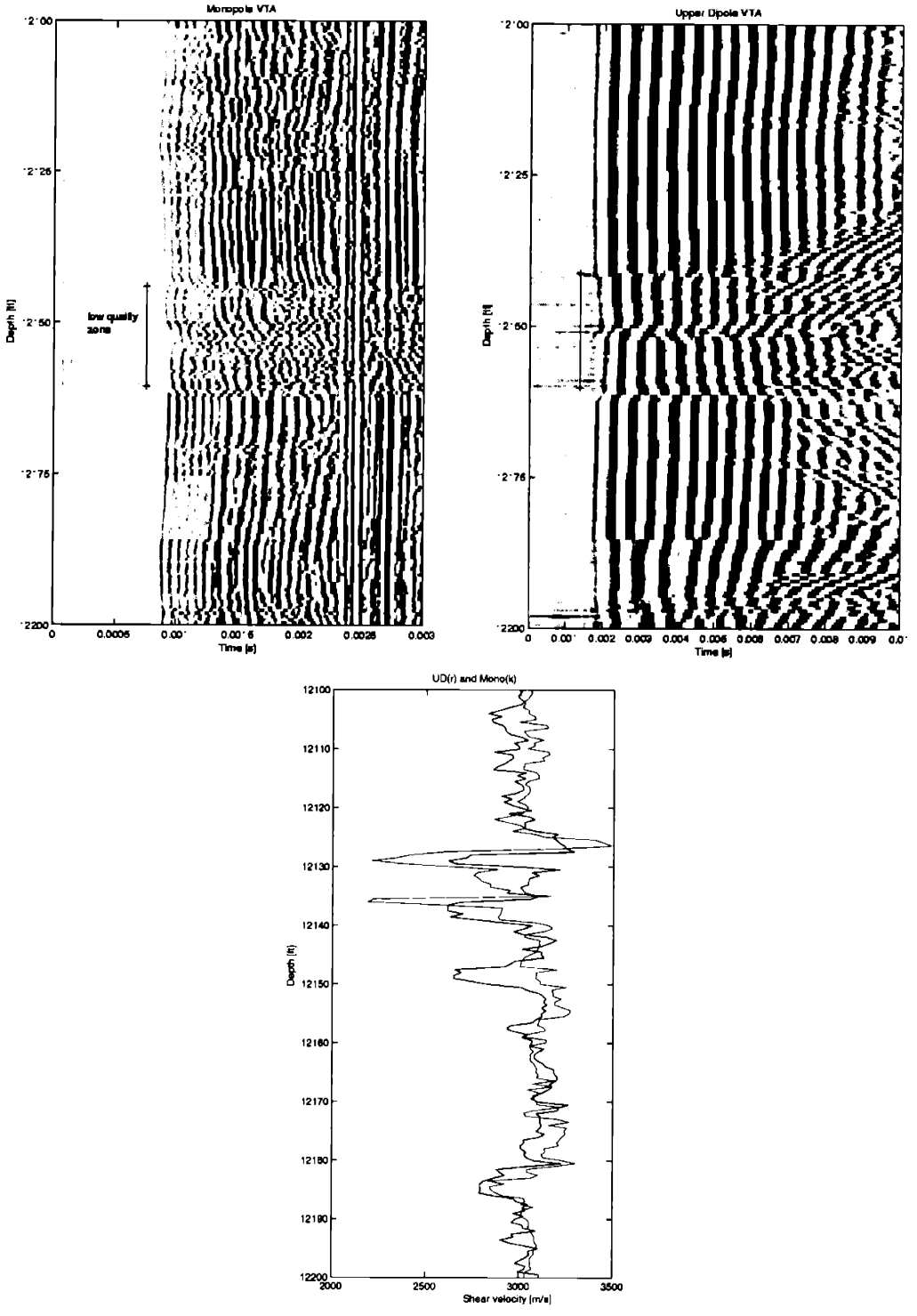

Figure 3-20: Dipole and monopole qualitative comparison for estimating shear velocity. Top figures: upper dipole (right) and monopole (left) in variable density between 12100 and 12200 ft. At the bottom figure, the upper dipole (in red) and the monopole shear velocity (in black) for the same interval. Differences around 12150 ft can be attributed to low quality of monopole data. In these cases, upper dipole velocities are more reliable.

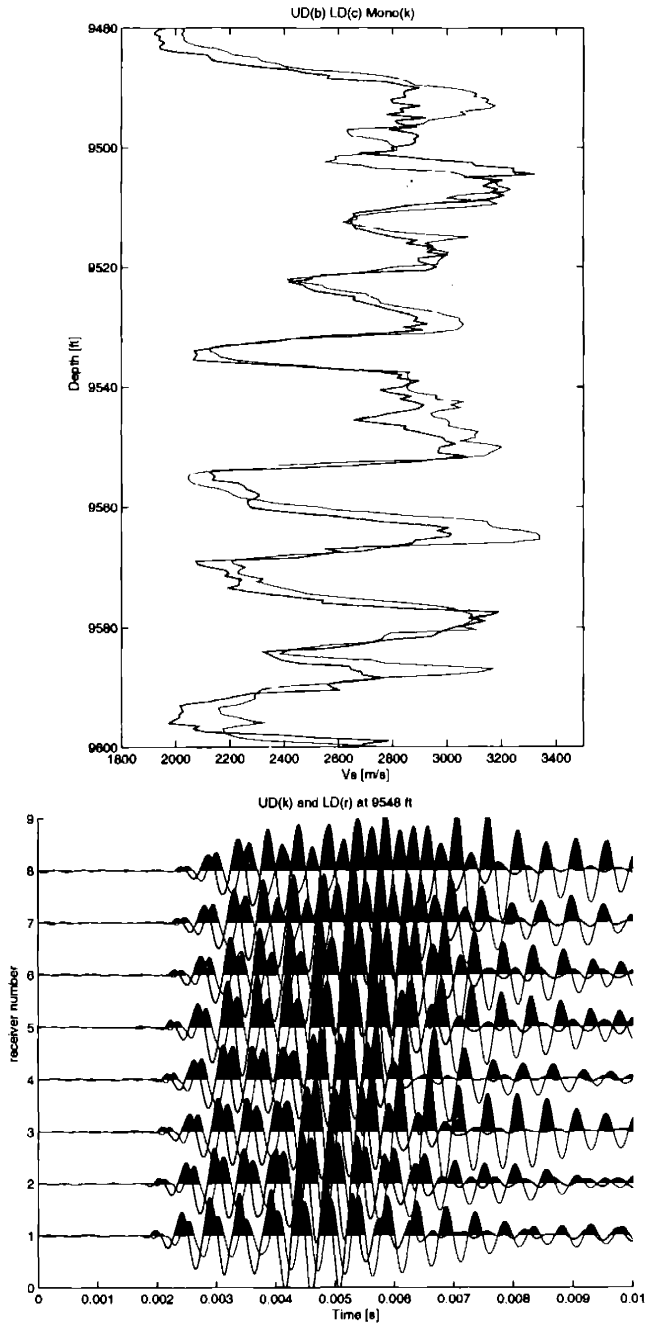

Figure 3-21: On the top, the upper (in blue), lower (in light blue) and monopole (in black) shear velocities, are plotted between 9480 and 9600 ft. At the bottom, the upper and lower dipole waveforms corresponding to the source location 9548 ft are displayed to show the delay in the first arrival indicating possibly the presence of anisotropy. In this interval, the mean anisotropy, if processed velocities are correct, is about 10% (slowness difference divided by average slowness). In average as well, the monopole velocity has an intermediate value between slow and fast velocities.

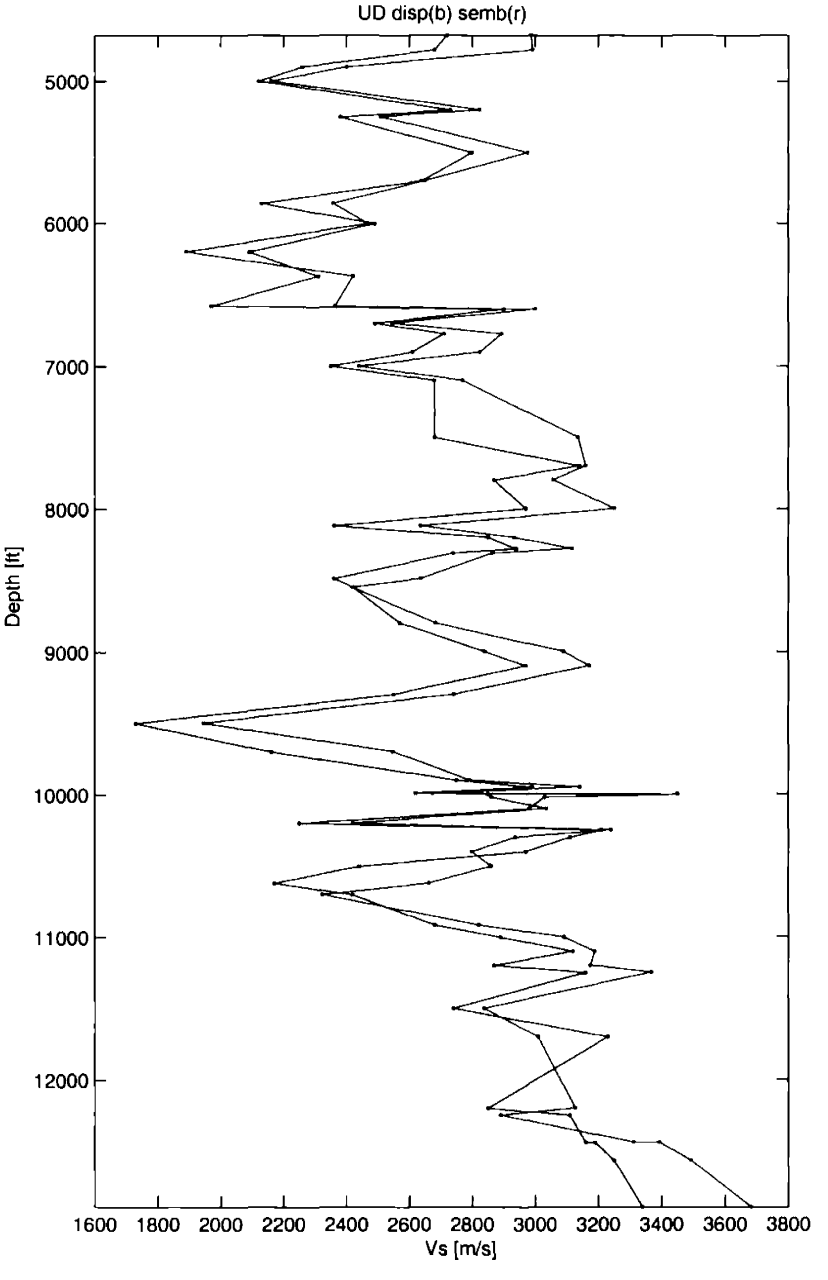

Figure 3-22: Dispersion velocities (in blue) are higher in 85% of the points processed by both methods. Standard semblance processing is shown in red.

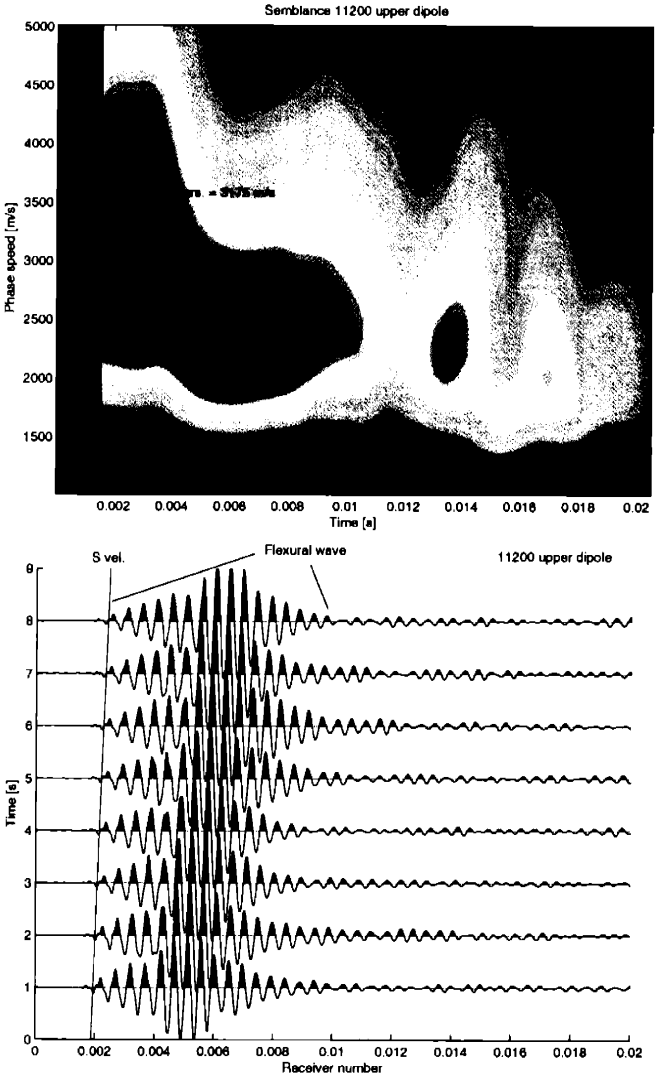

Figure 3-23: At 11200 ft the shear velocity suggested by semblance (top figure) is about 2870 m/s while the processing that takes into account the dispersion indicates that it should be 3175 m/s. Note that there is a good signal-to-noise ratio in the waveforms (bottom figure); the flexural mode is the wave indicated, where low frequencies travel faster close to the shear speed. Semblance fails not because low energy in the correlation but due to limitations in treating separately each frequency component. As a result, the energy function can show several maxima.

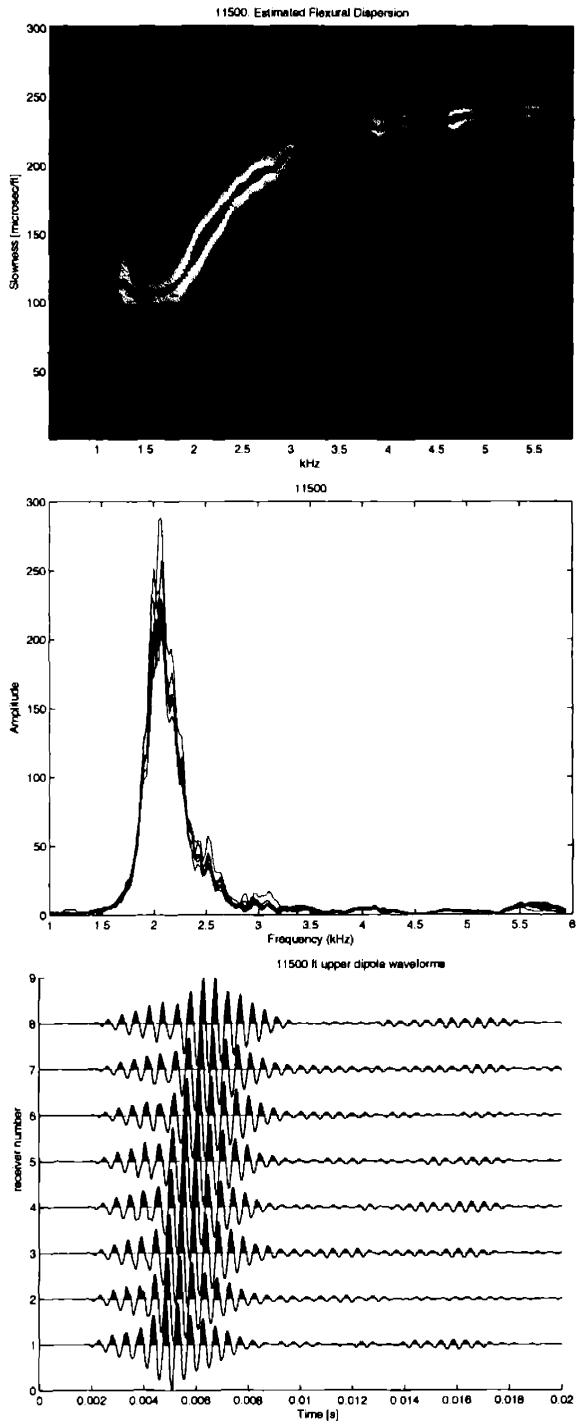

Figure 3-24: Top figure: dispersion analysis at 11500 ft upper dipole frame showing slowness vs. frequency. The black crosses follow the energy maxima. The shear velocity picked with this method is indicated at the low frequencies. At 11500 ft the dispersion method performs well since the non-dispersive part of the flexural wave is resolved. The middle figure shows the spectral amplitude confirming that non-dispersive frequencies correspond to peak ones (between 1.75 and 2.3 kHz). On the bottom, the waveforms are depicted; the flexural wave is distinctive between 2 and 9 ms. Here the borehole is circular and slightly larger (14.5 in).

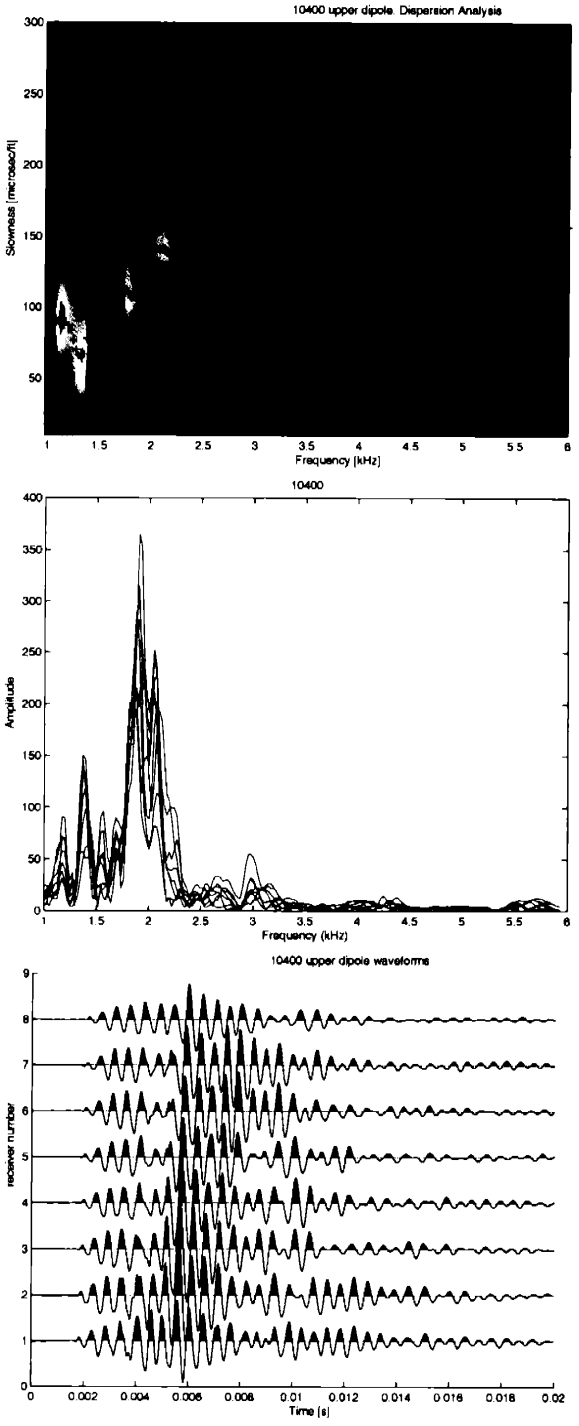

Figure 3-25: Top figure: dispersion analysis at 10400 ft. Black crosses follow energy maxima. Middle figure: spectral amplitude. Peak frequencies are shifted respect to the non dispersive part of the wave. This effect is due to the enlarged diameter of the borehole (borehole is elliptical 15 x 21.5 in) and to the fact that formation is fast (flexural wave is more dispersive). The bottom figure shows the waveforms. Signal to noise ratio is lower. This is a location where the nondispersive processing resulted in a faster velocity in comparison with the semblance value, another indication of the poor performance of the dispersive method.

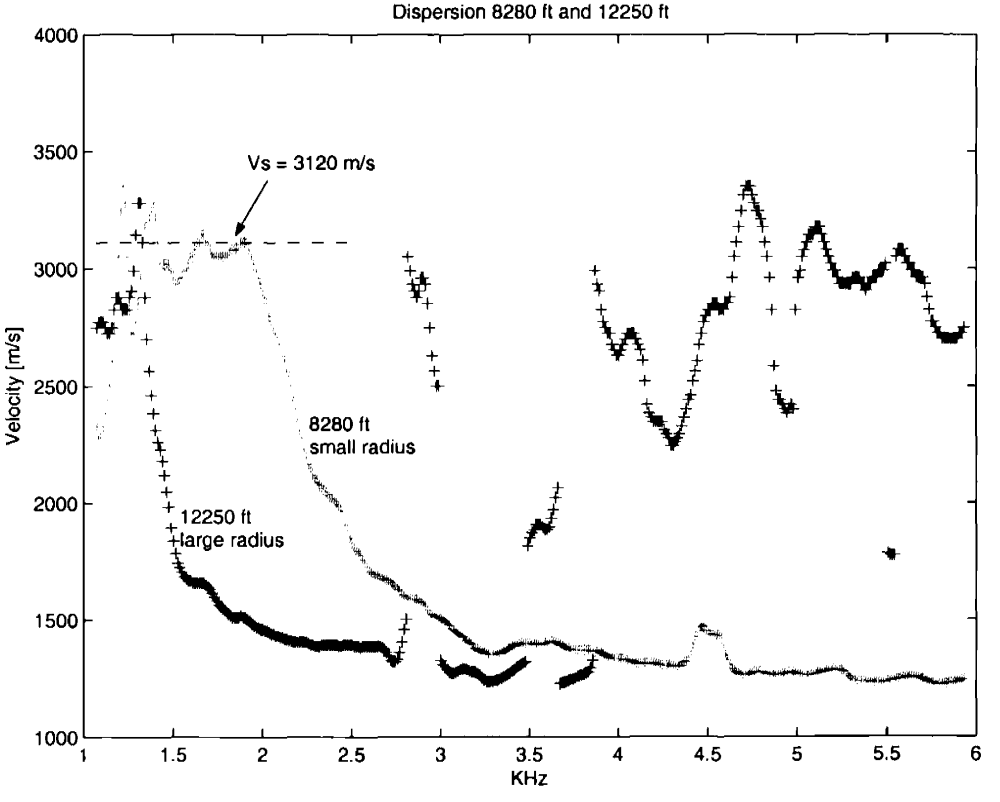

Figure 3-26: Comparison of dispersion curves (velocity vs. frequency) at two locations with different borehole geometry. The green curve corresponds to the 8280 ft frame; the pink one comes from the 12250 ft frame where the borehole cross section is elliptical (18 x 13 in). The analysis was done on the upper dipole frame whose direction coincides with the long axis in the 12250 ft case. Note the lower cutoff frequency when the borehole is larger. The shear velocity at 12250 ft is difficult to estimate with this method but from monopole data, it is about 3100 m/s, meaning it is close to the velocity at 8280 ft, therefore difference in dispersion curves should be mainly due to borehole size.

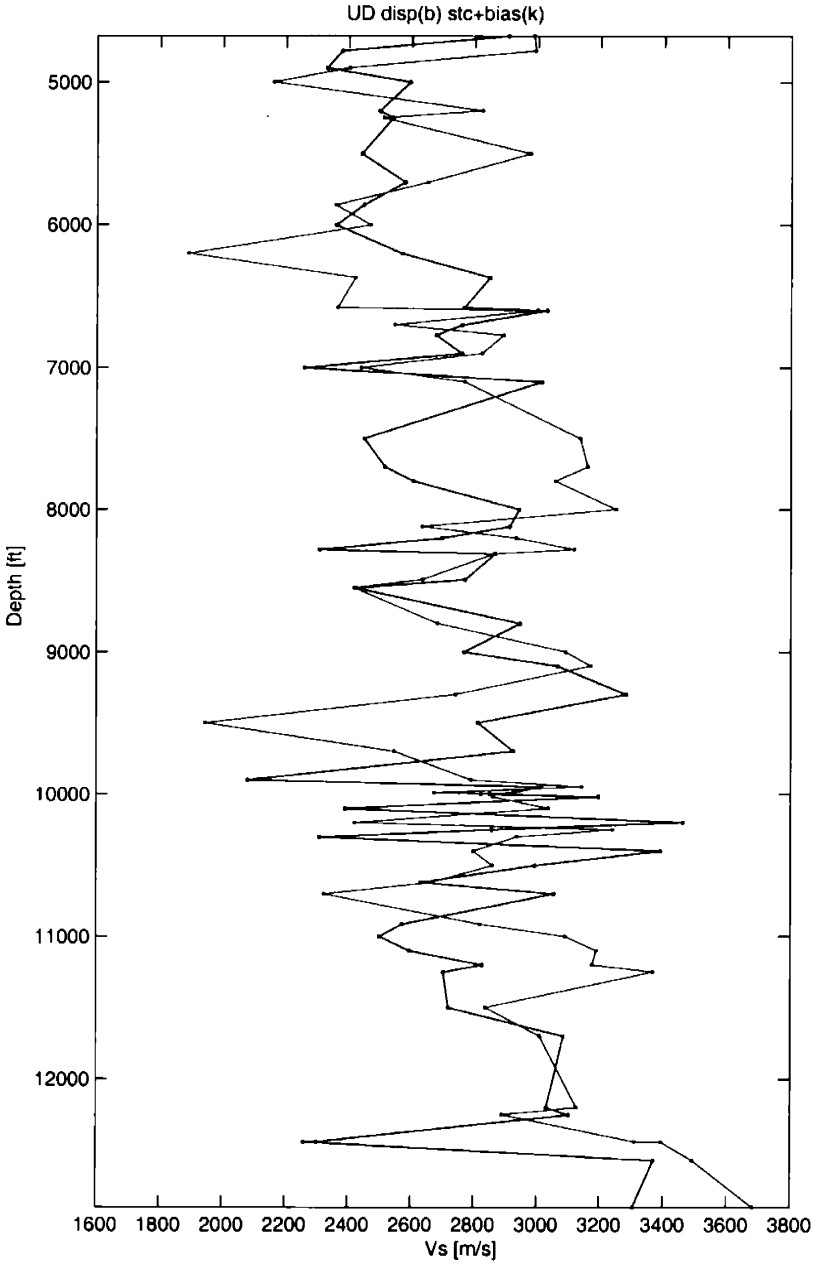

Figure 3-27: Dispersion (blue) and automatic STC plus correction velocities (black) at control points. Both correspond to the upper dipole data. The former ones are in 60% of the points faster.

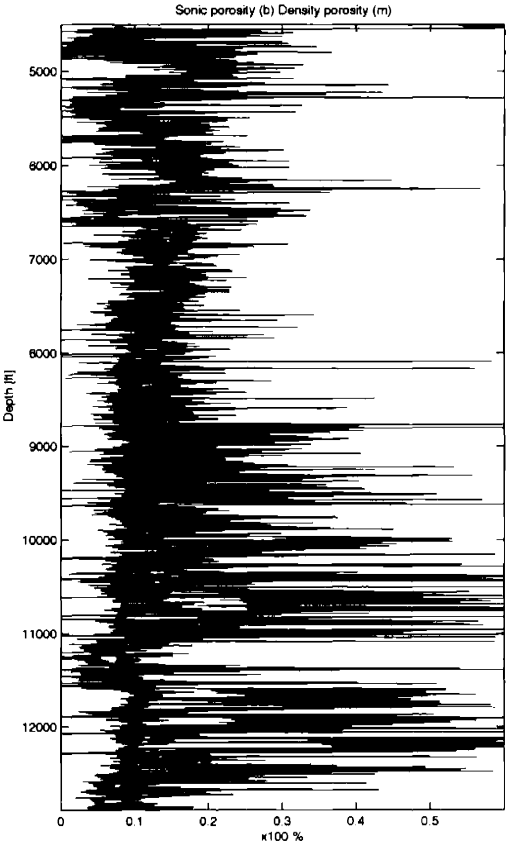

Figure 3-28: Sonic-derived porosity (black) and density-derived porosity.

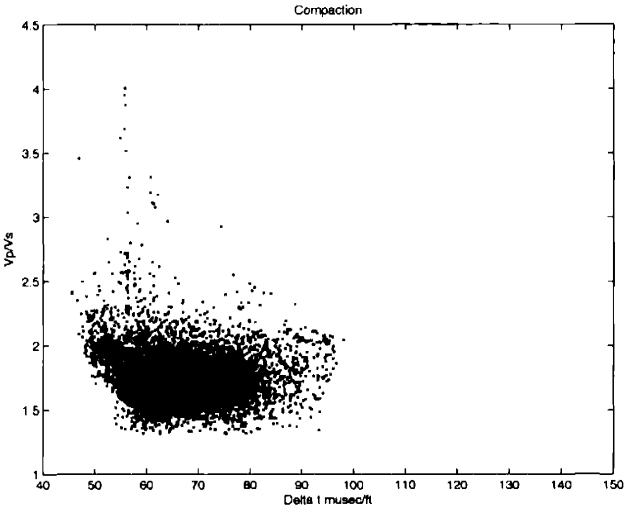

Figure 3-29: Rock consolidation through Vp/Vs vs. Δt_c. Formations in well M exhibit low values of compressional travel time and Vp/Vs ratios indicating that these rocks are well consolidated.

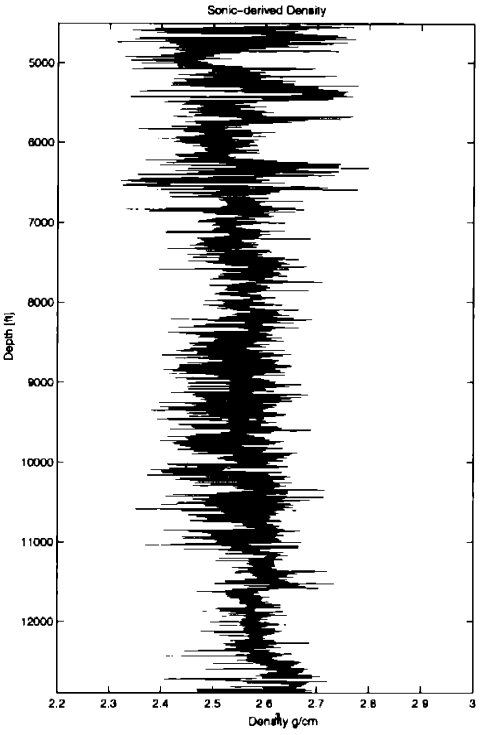

Figure 3-30: Sonic-derived density

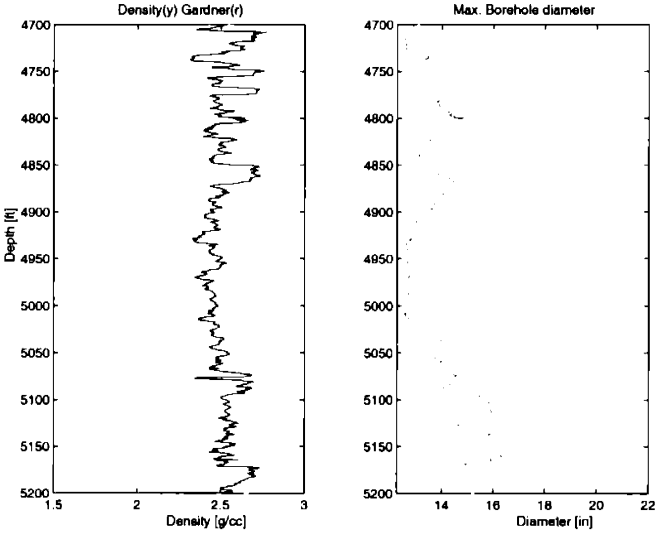

Figure 3-31: To the left density computed from velocity log, in red, and measured bulk density directly from density log tool, in yellow. To the right, the corresponding long borehole axis is plotted to indicate that where borehole is stable or slightly unstable, the quantities are similar (for example at 4950 ft). In contrast, values from density log are different from computed density where borehole is enlarged as at 5150 ft.

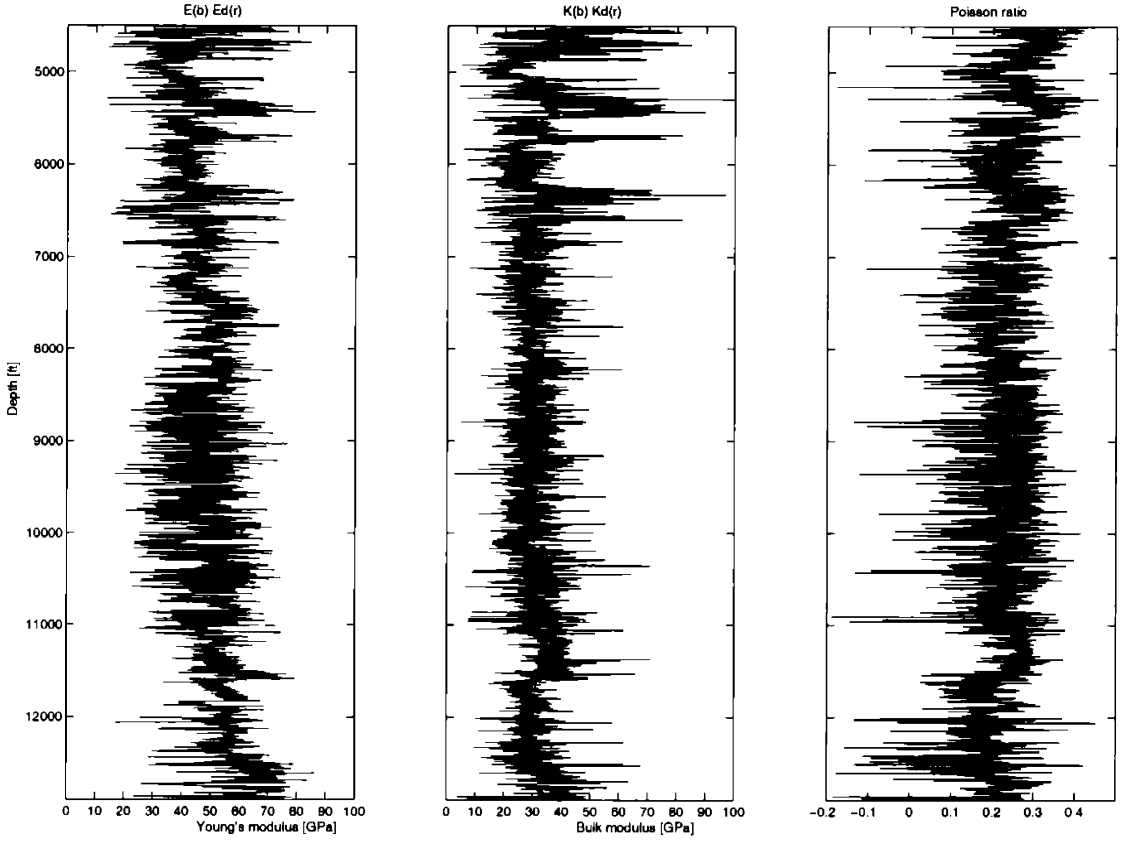

Figure 3-32: Dynamic Elastic Moduli. Young's modulus (left) and Bulk modulus (middle) have been corrected by fluid saturation (red). In the Poisson ratio (right), the errors in velocities are evidenced since rocks must exhibit positive values and typically below 0.3.

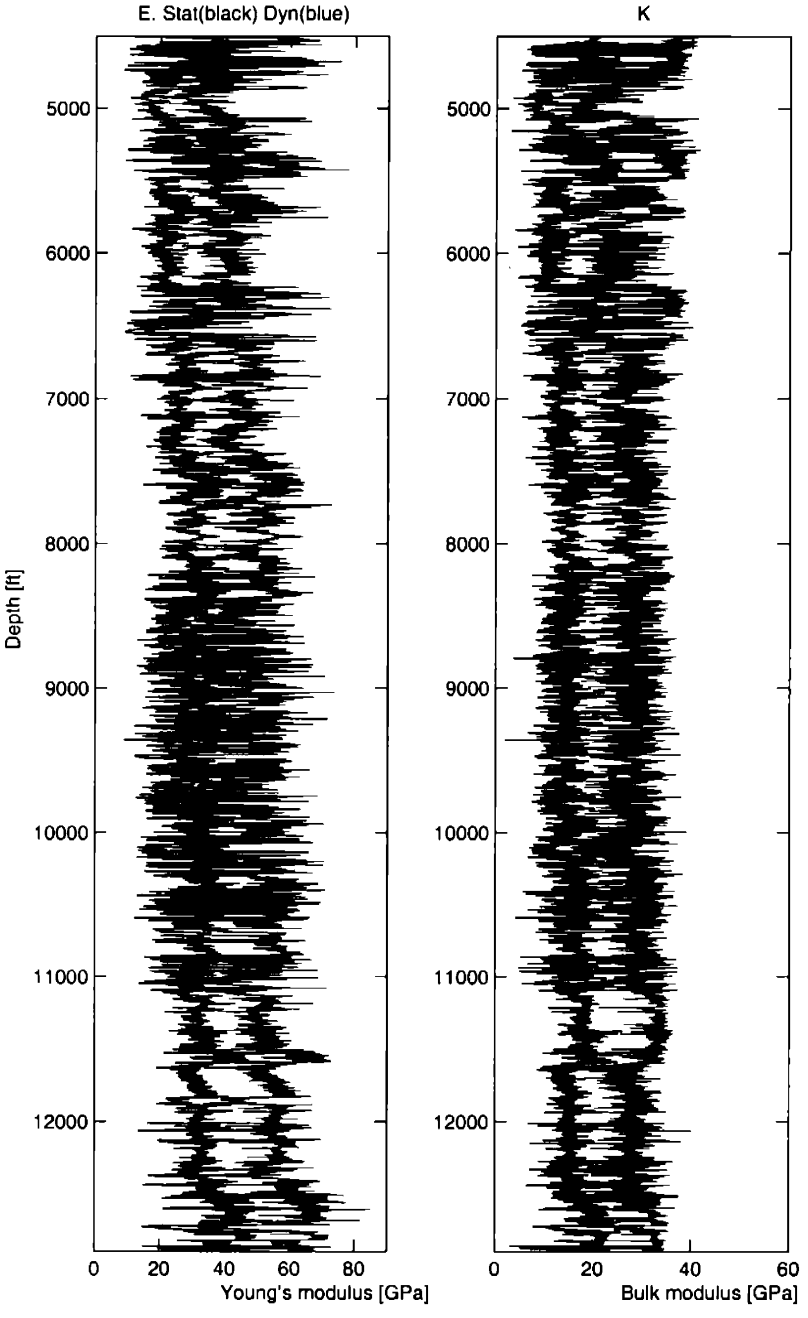

Figure 3-33: Static bulk (right) and Young's moduli (left) plotted both in black along with dynamic values in blue.

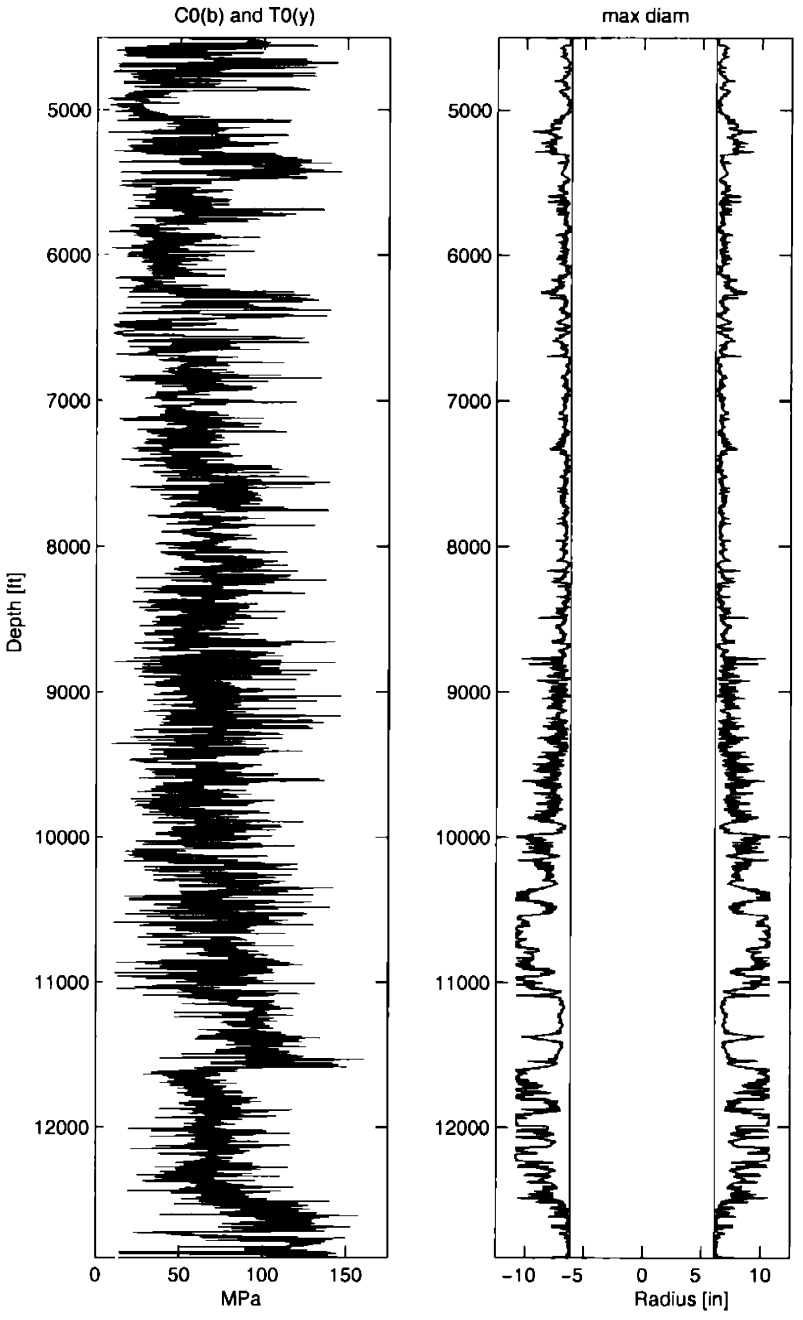

Figure 3-34: Compressive (blue) and tensile (yellow) strength on the left figure. In the right panel, the maximum diameter of the borehole is plotted in black and the nominal size in red.

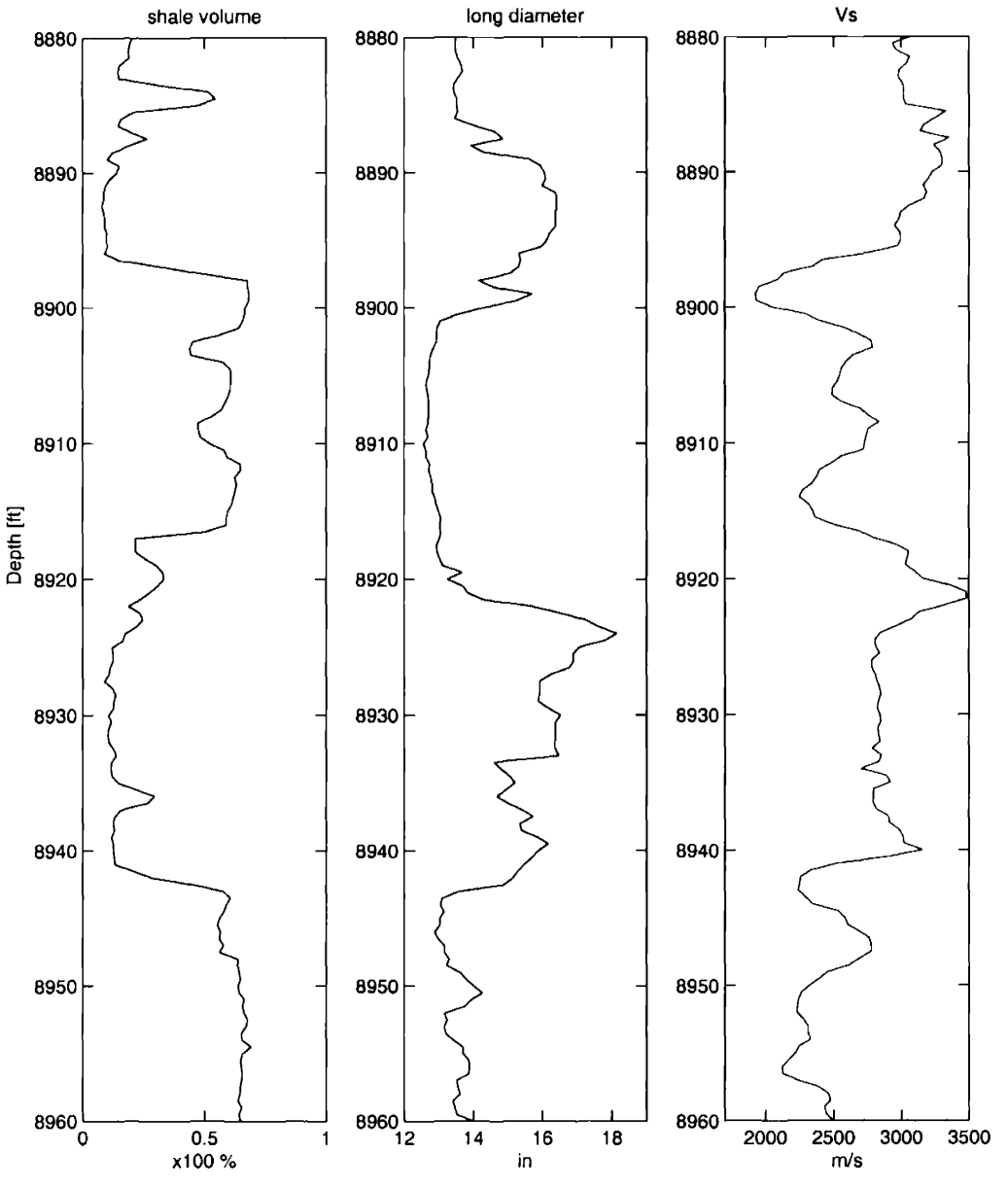

Figure 3-35: From left to right: shale volume, maximum borehole diameter and shear velocity. The borehole is unstable (middle figure) at faster formations (right), usually when the rock is a cleaner sandstones (left) as for example between 8920 and 8940 ft. In contrast, at shaley intervals (left), as in 8900-8920 ft, the borehole is stable (middle) even when the formation velocity is slow in comparison with the sandstone below (right).

Chapter 4

Summary and Conclusions

In this thesis an analysis of several logs ran on a borehole with severe instabilities was presented. Instabilities had caused borehole failures, breakouts, and irregularities. The evaluation of the effects of the borehole enlarged diameter lead to the following conclusions:

1. In lithology logs, such as standard Gamma Ray and Natural Gamma Ray Spectrometry, corrections for borehole size, tool off-centering and mud weight, seem to be effective in making the measurement usable. The formation properties derived from these logs, such as the shale volume, are reliable.

2. The rate of perforation (drilling) should be considered as an indicator of possible damage in the borehole. Utilization of denser drilling fluids helps to prevent breakouts, however this practice slows the operation and has other drawbacks.

3. The density log is unreliable. The density tool design is susceptible to departures from ideal borehole conditions and the second detector correction is insufficient under severe borehole elongation. Porosity and formation parameters derived from density measurements on unstable boreholes are also unreliable. Sonic logs provide a way of obtaining density, through Gardner's equation, however, some knowledge of saturation and lithology is required.

4. The four-arms dipmeter log is unreliable when borehole size is close or greater

than the maximum arms aperture. In well M, this limit is about 19 inches. From our own analysis of dipmeter data, we were able to infer that beds are nearly horizontal and there is some soft dip of maximum 23° to the SE. Breakout data provided reliable information on horizontal stress direction, being the minimum stress oriented ENE-WSW; possible fracture zones detected have strikes aligned with maximum stress direction as expected (N-S).

5. Presence of steep radius variations, ellipticity and small scale rugosities affect acoustic logs. Shear/ pseudo-Rayleigh and Stoneley arrivals are blurred in VTA plots (iso-offset sections) indicating that the scattering from perturbations on the borehole wall disrupts the wave paths. The diminished quality affects not only the estimation of velocity but also other applications such as permeability estimation.

6. In well M, P wave velocity obtained by commercial processors, has an average of 10% uncertainty. Locally, errors may increase to 40%. Semblance processing parameters, such as correlation window length, account for less than 4% of the differences in velocities between automatic and control points. The rest of the errors are attributed to low performance of peak-finding routines shown to be sensitive to signal-to-noise ratio. We reprocessed part of the log data to obtain P wave velocity.

7. Presence of borehole elongations in the case of monopole data does not necessarily under or overestimate velocities but they make the conventional velocity processing methods fail. For circular large holes the number of pseudo Rayleigh modes increases. Additionally, Stoneley wave amplitude is weaker in comparison with the small radii cases. Small-scale rugosities in the borehole wall reduce signal-to noise ratio and therefore accuracy of automatic velocity estimation.

8. The effects of non-circular borehole have to be investigated further. In well M data we noted that the energy of pseudo Rayleigh wave is reduced as compared to circular cases. We attribute this to the lack of axial symmetry, for the axially

symmetric monopole modes. On the other hand, P head waves and Stoneley waves are enhanced in some cases. This can be attributed to one diameter being close to nominal size.

9. Shear velocity estimated from dipole data is more reliable than from monopole data. Flexural waves generated at these low frequencies are less affected by the conditions near the borehole wall. Similarly, elliptical shapes do not seem to introduce as many complications as in the monopole case. The uncertainties in the automatic shear velocity interpreted from this analysis vary between 13 and 40%.

10. Significant ellipticity of borehole requires the incorporation of correction by the borehole shape on full-waveform acoustic logs, in order to avoid erroneous calculation of rock properties. Further modelling is indispensable in understanding the effects of irregular borehole irregularities on the propagation of waves.

11. The static to dynamic Young's modulus ratio is about 0.62, found with an empirical relationship and assuming that the total strain comes from the added contributions of elastic and non-elastic deformations and that the non-elastic part is proportional to the stress increment. Poisson ratio, Young and bulk modulus show large variations, some of which can be attributed to fine layering and clay content. However, part of it may be related to uncertainties in the velocities due to borehole conditions. Poisson ratio has to be interpreted carefully since it is directly affected by velocity errors.

12. Rock strength was computed by an empirical relation that may overestimate the dependency on shale volume. Values obtained in well M are low in comparison with experimental studies due to differences in confining pressures. Clay content adds "ductibility" to rocks, therefore, under high stresses, these rocks have less tendency to fail in spite of the lower moduli and strength.

Appendix A

Rock Deformation Phenomena

When a solid body is subjected to stress, internal forces tend to return it to its mechanical equilibrium. Stresses must then equate the sum of all forces on the volume elements of the body, $\int F\,dV$. However, for elements with shared contact surfaces, forces are cancelled by Newton's 3rd. law, and ultimately the only contributing forces to the resultant integral act on the surface of the body. Stresses can therefore be represented as the sum of forces acting on the surface, that is by an integral over the closed surface. From vector calculus, a volume integral can be transformed into a surface integral, as long as the scalar function in the volume integral, is the divergence of a vector function[1]. Since forces are vectors, they must be the divergence of tensors of rank two. Hence,

$$F_i = \frac{\partial \sigma_{ik}}{\partial x_k} \tag{A.1}$$

The volume integral can then be rewritten as a surface integral,

$$\int F_i\,dV = \int \frac{\partial \sigma_{ik}}{\partial x_k}\,dV = \oint \sigma_{ik}\,df_k \tag{A.2}$$

where df are the surface elements and σ_{ik} is the ith component of the force on a unit area acting perpendicular to the x_k axis (Landau and Lifshitz, 1986).

[1]Gauss Theorem: $\int A\,dV = \oint B\,dS$ if $A = \nabla B$

The stress tensor can be decomposed in terms of three traction vectors acting on arbitrary planes (fig. A-2). If taking an infinitesimal volume element, at the point Q (the center of the block), the stress tensor approaches:

$$T = \begin{bmatrix} \sigma_{11} & \sigma_{12} & \sigma_{13} \\ \sigma_{21} & \sigma_{22} & \sigma_{23} \\ \sigma_{31} & \sigma_{32} & \sigma_{33} \end{bmatrix} \tag{A.3}$$

where the components (second subscript), of the 3 vectors acting on each of the planes (first subscript), perpendicular to the coordinate axes have been displayed in matrix form. The state of stress at a point cannot be specified completely by a single vector with three components; it requires a second-order tensor with nine components. By symmetry considerations, only six components are independent (Malvern, 1969).

Internal forces acting on the body at a particular point O can be described independently from the direction of "observation". Let's say we are at point P, an infinitesimal distance from O, and let's look at a plane through O of area δA whose normal coincides with the OP direction (fig. A-1). We could choose a coordinate system such that the Ox axis is in the OP direction, in other words the plane is perpendicular to Ox. In this case, the stress vector components are σ_x, τ_{xy} and τ_{xz}. Similarly, we could have chosen axes such that Oy or Oz coincide with OP, or equivalently, looked at planes perpendicular to these axes. The quantity,

$$\lim_{\delta A \to \infty} \frac{\delta F}{\delta A} \tag{A.4}$$

is a vector of three components for each of the three possible plane orientations and together form the stress tensor. The stress matrix components will be hereinafter referred using the more convenient notation:

$$T = \begin{bmatrix} \sigma_x & \tau_{xy} & \tau_{zx} \\ \tau_{xy} & \sigma_y & \tau_{yz} \\ \tau_{zx} & \tau_{yz} & \sigma_z \end{bmatrix} \tag{A.5}$$

where σ_i represent the normal stresses, that is, the area element is perpendicular to axis i, and τ_{ij} represent the shear stresses, forces tending to slide or shear the material in the plane of the area element.

It is always possible to find a coordinate system where shear stresses vanish. The stress components relative to these axes are called principal stresses, σ_1, σ_2 and σ_3. The principal directions at any point may be found by solving the eigenvector-eigenvalue associated problem when the nine stress components σ_{ij} are known in some other Cartesian coordinate system (Malvern, 1969)

$$|\sigma - \lambda I| = 0 \tag{A.6}$$

λ being the values of principal stresses sought.

In 2D, the stress tensor has only 3 components, since $\tau_{xy} = \tau_{yx}$. Taking a plane inclined θ with respect to Ox we can determine the components of the stress vector corresponding to the direction OP (Jaeger and Cook, 1979) (fig. A-1):

$$\begin{aligned} p_x &= \sigma_x \cos\theta + \tau_{yx} \sin\theta \\ p_y &= \sigma_y \sin\theta + \tau_{xy} \cos\theta \end{aligned} \tag{A.7}$$

the normal and shear stresses σ and τ across the plane whose normal is in the OP direction are:

$$\begin{aligned} \sigma &= p_x \cos\theta + p_y \sin\theta \\ \tau &= p_y \cos\theta - p_x \sin\theta \end{aligned} \tag{A.8}$$

substituting A.7 in A.8 one obtains:

$$\begin{aligned} \sigma &= \sigma_x \cos^2\theta + 2\tau_{xy} \sin\theta \cos\theta + \sigma_y \sin^2\theta \\ \tau &= \tau_{xy}(\cos^2\theta - \sin^2\theta) + (\sin\theta \cos\theta)(\sigma_x - \sigma_y) \end{aligned} \tag{A.9}$$

σ, τ correspond to σ'_x and τ'_{xy} for a system of axes rotated θ from Oxy. If the plane

is at $\theta + \pi/2$, σ will correspond to σ'_y :

$$\sigma = \sigma_x \sin^2\theta - 2\tau xy \sin\theta\cos\theta + \sigma_y \cos^2\theta \tag{A.10}$$

The system where shear stresses vanish (principal axes) is found equating $\tau = 0$ in A.9. Then, the angle is

$$\tan 2\theta = \frac{2\tau_{xy}}{\sigma_x - \sigma_y} \tag{A.11}$$

and σ'_x and σ'_y correspond to σ_1 and σ_2 respectively, where

$$\begin{aligned} \sigma_1 &= \frac{1}{2}(\sigma_x + \sigma_y) + [\tau_{xy}^2 + \frac{1}{4}(\sigma_x - \sigma_y)^2]^{\frac{1}{2}} \\ \sigma_2 &= \frac{1}{2}(\sigma_x + \sigma_y) - [\tau_{xy}^2 + \frac{1}{4}(\sigma_x - \sigma_y)^2]^{\frac{1}{2}} \end{aligned} \tag{A.12}$$

If Oxy is chosen in the directions of σ_1 and σ_2,

$$\begin{aligned} \sigma &= \sigma_1 \cos^2\theta + \sigma_2 \sin^2\theta = \frac{1}{2}(\sigma_1 + \sigma_2) + \frac{1}{2}(\sigma_1 - \sigma_2)cos2\theta \\ \tau &= -\frac{1}{2}(\sigma_1 - \sigma_2)\sin 2\theta \end{aligned} \tag{A.13}$$

here again, σ and τ act across a plane inclined θ from the σ_1 direction.

From A.13, it is clear that at $\theta = 0, \pi/2, \pi$, shear stress vanishes and normal stress oscillates between σ_1 and σ_2 (fig. A-3). Shear stresses are maximum when plane is inclined 45° from principal axes.

Under the action of applied forces, solid bodies exhibit deformation to some extent, i.e. they change in shape and volume (Landau and Lifshitz, 1986). Consider two points very close where the distance between them is $dl^2 = (dx_1^2 + dx_2^2 + dx_3^2)^{\frac{1}{2}}$. After deformation takes place the distance between these points change,

$$\hat{dl}^2 = (dx_i + du_i)^2 \tag{A.14}$$

du_i refers to the displacement vector from the original position to the deformed one

and can be expressed as:

$$du_i = \frac{\partial u_i}{\partial x_k} dx_k \tag{A.15}$$

Substituting A.15 in A.14, the distance between the two points after deformation is:

$$\hat{dl}^2 = (dx_i + \frac{\partial u_i}{\partial x_k} dx_k)^2 = dx_i^2 + 2\frac{\partial u_i}{\partial x_k} dx_k dx_i + (\frac{\partial u_i}{\partial x_k} dx_k)^2 \tag{A.16}$$

where the quadratic has been expanded. After agrouping terms,

$$\begin{aligned} \hat{dl}^2 &= dl^2 + 2\epsilon_{ik} dx_i dx_k \\ \epsilon_{ik} &= \frac{1}{2}(\frac{\partial u_i}{\partial x_k} + \frac{\partial u_k}{\partial x_i} + \frac{\partial u_l}{\partial x_k}\frac{\partial u_l}{\partial x_i}) \end{aligned} \tag{A.17}$$

ϵ_{ik} is the symmetric strain tensor. If only small deformations are considered the second term in the strain definition A.17 is of 2nd. order of smallness and can be disregarded. Thus, under this assumption the strain tensor is given by

$$\epsilon_{ik} = \frac{1}{2}(\frac{\partial u_i}{\partial x_k} + \frac{\partial u_k}{\partial x_i}) \tag{A.18}$$

Just as in the case of stress, the strain tensor can be diagonalized to get the principal axes and principal strains ϵ_1, ϵ_2 and ϵ_3. On this coordinate axes and developing the definition of dl in A.17,

$$\hat{dl}^2 = (1 + 2\epsilon_1)dx_1^2 + (1 + 2\epsilon_2)dx_2^2 + (1 + 2\epsilon_3)dx_3^2 \tag{A.19}$$

or more generally,

$$\hat{dl}^2 = (\delta_{ik} + 2\epsilon_{ik})dx_i dx_k \tag{A.20}$$

From the expression A.19 the strain in any volume element may be interpreted as composed of independent strains in three mutually perpendicular directions, namely those of the principal axes of the strain tensor. Each of these strains is an extension or

compression in the corresponding direction. In here, compression is reckoned positive while tensional stresses or expansions are negatives.

Referred to the principal axes (in 2D), the elongation ϵ and shear strain Γ for a direction inclined θ to the ϵ_1-direction are:

$$\begin{aligned} \epsilon &= \epsilon_1 \cos^2\theta + \epsilon_2 \sin^2\theta \\ \Gamma &= -\frac{1}{2}(\epsilon_1 - \epsilon_2)\sin 2\theta \end{aligned} \tag{A.21}$$

A.1 Friction and failure

Rock masses are broken up by faults, joints and other planes of weakness. Relative movement and friction of these is of great importance when studying stress-strain.

In figure A-1, suppose that the inclined plane represents the contact surface between two bodies that are being pressed together. σ and τ would be interpret in this experiment as the stress normal to the plane of contact and the shear stress parallel to the surface necessary to initiate sliding on it. The ratio of these quantities is called the coefficient of friction μ, which depends on the nature of the material (Jaeger and Cook, 1979) and it is also a static property. In contrast, if sliding is in progress the coefficient of friction is called dynamic and is expected to be less than its static counterpart.

Most minerals tend to fail by brittle fracture rather than by plastic flow (Jaeger and Cook, 1979), therefore the experimental driven adaptations of the friction law to explain otherwise elastic behaviour will be disregarded here. On the other hand, Jaeger and Cook (1979) claim that the linear law:

$$\tau = S_0 + \mu\sigma \tag{A.22}$$

best fits experiments held on rocks at low stresses, where S_0 refers to the inherent shear strength or cohesion, of the contact surface. Some μ and S_0 values for rocks are reported in table A.1.

Combining equations A.13 and A.22, we can study the variation of $(\sigma_1 - \sigma_2)$ with θ, necessary to cause sliding for fixed values of σ_2 and μ,

$$\sigma_1 - \sigma_2 = \frac{2S_0 + 2\mu\sigma_2}{(1 - \mu\cot\theta)\sin 2\theta} \tag{A.23}$$

From here, the difference $(\sigma_1 - \sigma_2) \to \infty$ for $\theta \to \pi/2$, that is, as the plane moves towards the direction of σ_1. Sliding (or friction) on a plane of weakness is conveniently studied with the aid of Mohr's representation of stress.

The general behavior of rocks and other elastic materials is shown in the curve depicted in figure A-4. As the applied stress increases from zero, several features are observed: in the first two regions, OA and AB, the material is nearly linear elastic. No irreversible changes are produced and if unloading takes place, strain returns to zero although possibly by a different path (hysteresis). In the region BC_0, the slope of the stress-strain curve decreases progressively to zero with increasing stress. The material is ductile because it can sustain permanent deformation without losing ability to resist load. The point C_0 marks the transition from ductile to brittle behavior. From C_0, the stress-strain curve has negative slope and deformation is also irreversible, however the ability to resist load decreases with increasing deformation. C_0 represents the uniaxial compressive strength of the rock and it depends on internal properties of the material as well as on the confining pressure and temperature. Confining pressure has the effect of increasing the strength while higher temperature lowers the brittle-ductile transition point (Jaeger and Cook, 1979).

Following the terminology in Jaeger and Cook (1979), failure refers to a continuous process that occurs progressively throughout the brittle region C_0D. The rock steadily deteriorates in this region until complete loss of cohesion happens across a plane and the material fractures. However, due to limitations of the testing machines used in laboratory experiments, brittle fracture is observed to occur at a point very near to C_0.

Jaeger and Cook (1979) also report that typical rocks behave generally as the idealized curve of figure A-4. Moreover, experimental data indicates that the assumption

of linear elasticity up to the beggining of failure is a good one in many cases.

In tension, the former description is equivalent and the value of the stress at failure, will correspond to the uniaxial tensile strength T_0. The modulus is usually less than that in compression (table A.2) since rocks contain voids and cracks that add resistance to failure under compression but make the material more compliant under tension. In general, compressive strength is inversely related to porosity.

Care should be taken though when extrapoling laboratory measured strengths or coefficients of friction to field values, since large variations may be expected. The constants demanded by simple theory are in fact statistical functions of the properties of the discontinuities, the gradient of the applied stress field, the measuring method, and possibly other variables (Jaeger and Cook, 1979).

If triaxial stresses are considered, failure takes place when a definite relation characteristic of the material $\sigma_1 = f(\sigma_2, \sigma_3)$ is satisfied. Such a relation is called a *criterion of failure*. The uniaxial tensile strength of the rock is reached at $\sigma_3 = -T_0$, $\sigma_1 = \sigma_2 = 0$ and the uniaxial compressive strength at $\sigma_1 = C_0$, $\sigma_2 = \sigma_3 = 0$. There are several criteria of failure (the Tresca criterion, the Hoek and Brown criterion, the Drucker-Prager criterion etc). From them, the simplest but most important one is the Coulomb-Navier, Coulomb-Mohr or simply, Coulomb criterion. Its linearized version in which the stress at failure σ_1 depends only on σ_3, will be the one assumed here,

$$\begin{aligned} \sigma_1 &= q\sigma_3 + C_0 \\ q &= (\sqrt{\mu^2+1} + \mu)^2 \end{aligned} \tag{A.24}$$

The form A.24 is the same relation found experimentally for sliding friction (eqn. A.22), $\tau - \mu\sigma = S_0$, when expressions A.13 are substituted in the first term and the definition $\tan 2\theta = -1/\mu$ is developed (Jaeger and Cook, 1979). The connection between both relations is given by:

$$C_0 = 2S_0[(\mu^2+1)^{\frac{1}{2}} + \mu] \tag{A.25}$$

If we have three unequal principal stresses, the values of σ and τ can be found by Mohr construction.

A.2 Mohr's Circle

The Mohr's circle diagram is the most important graphical method of representing the variation of stress with respect to plane inclination. In the Mohr's representation, (fig. A-5), (σ, τ) are plotted as coordinates. Any point in this plane will represent the state of stress on a plane through O in the physical body.

In two dimensions (no variation in z-direction, $\sigma_3 = 0$), Mohr's circle centre is found at:

$$\sigma = \frac{1}{2}(\sigma_1 + \sigma_2) \tag{A.26}$$

One direct application of this representation is to obtain graphically the principal stresses and the directions of the principal axes knowing the stress state at other plane (Jaeger and Cook, 1979). If σ_x, σ_y and τ_{xy} are known, we use equations A.9 to get σ and τ for a plane normal to Ox, and plot them as point A (fig. A-5). Through A.10 and $-\tau_{xy}$ in A.9, the coordinates of point A' are found, which represents a plane normal to Oy. The distance between these points is the diameter of the Mohr's circle with center as before (equation A.26), and the values on the σ-axis where the circle cuts correspond to σ_2 and σ_1 with $\sigma_1 \geq \sigma_2$. The angle that forms Oσ axis, the center of the circle and point A is twice the angle between Ox and Oσ_1, that is, the direction of the principal axis.

Sliding on a plane of weakness is conveniently studied with the aid of Mohr's representation of stress. In figure A-6, the same principles of figure A-5 are reproduced along with equation A.22. The intercept of the friction law line with Oσ is given by $-S_0/\mu$. The coefficient of friction μ corresponds to the tangent of the angle that forms the friction line with the Oσ axis. The relationship between stresses and sliding is interpreted graphically in this way: when the plane is such that stresses are mapped

onto the circle arc FF', they are sufficient to cause slip, while if (σ,τ) lies on other points of the circle, it indicates that the resultant stresses are not enough to fail the rock, even though it has a plane of weakness. Alternatively, the latter could be understood as if the plane is located at an angle from the principal stress σ_1 where the difference $(\sigma_1 - \sigma_2) \rightarrow \infty$ (Jaeger and Cook, 1979).

Failure will not take place if σ,τ lie below the line A.24. Failure will take place if the circle of diameter $\sigma_1 - \sigma_3$ just touches this line, implying that the intermediate principal stress does not affect failure although the plane of shear fracture passes through the direction of this stress.

Table A.1: μ and S_0 for some rocks. Modified from Jaeger and Cook (1979)

Rock	μ	S_0(MPa)
Granite	0.64	0.31
Marble	0.75	1.1
Sandstone	0.51	0.28

Table A.2: C_0 and T_0 for some rocks. Modified from Jaeger and Cook (1979)

Rock	C_0 [MPa]	T_0[MPa]
Granite	230	20
Marble	90	7
Sandstone	50	4

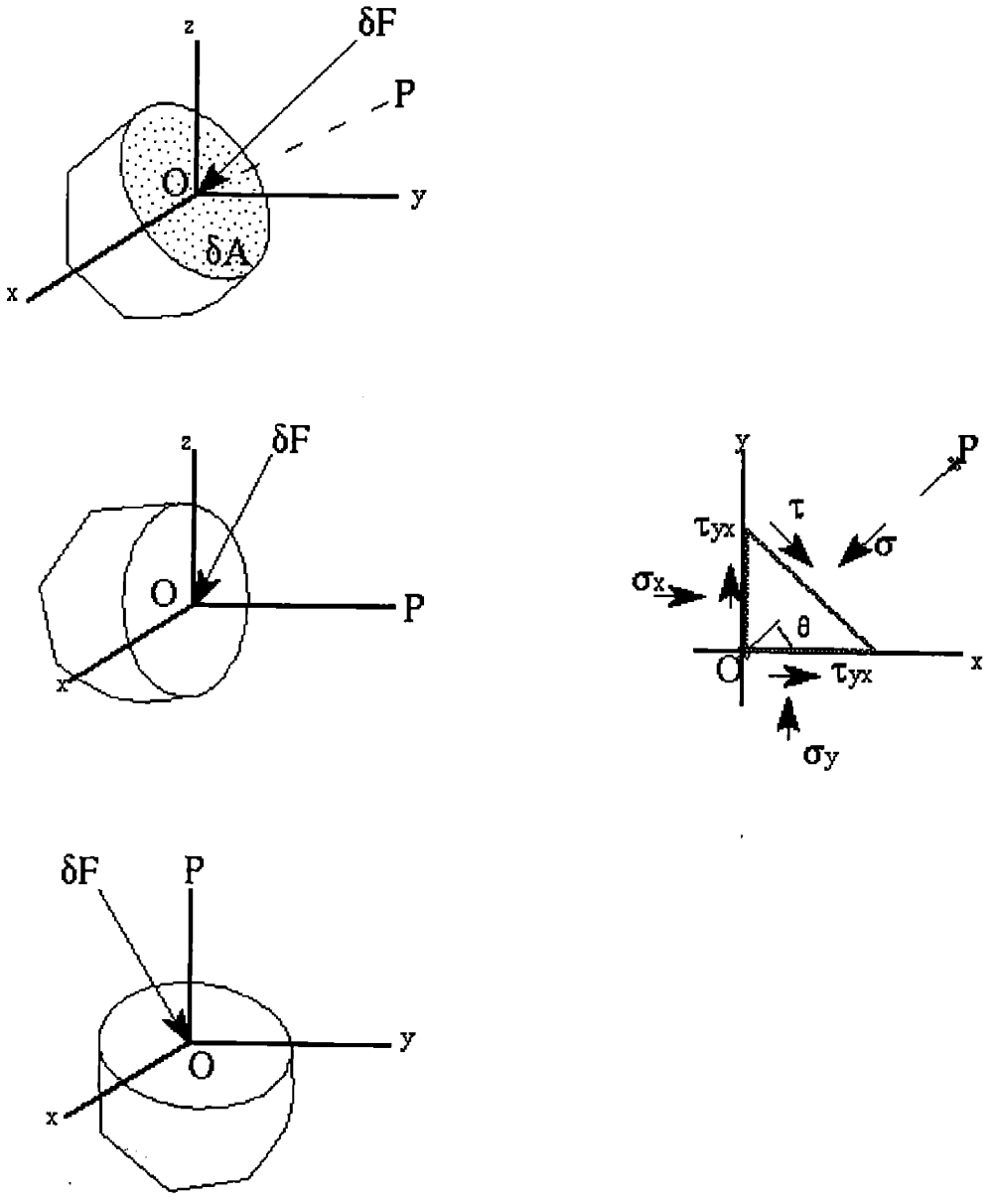

Figure A-1: On the left three possible plane inclinations corresponding to pOx pOy and pOz. On the right the stress components in 2D are shown respect to a plane inclined θ.

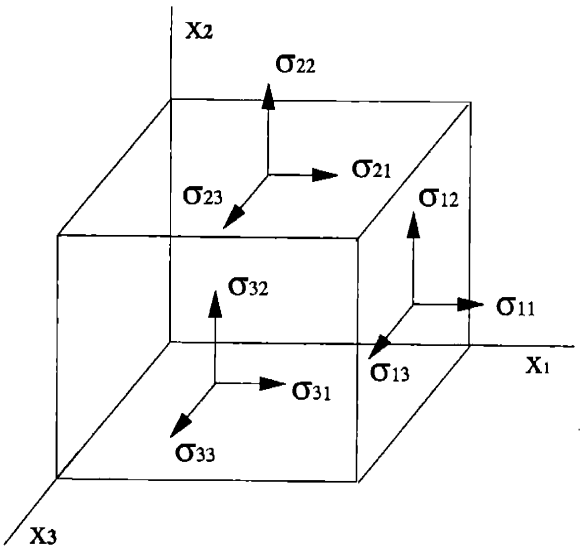

Figure A-2: Stress tensor components in matrix notation.

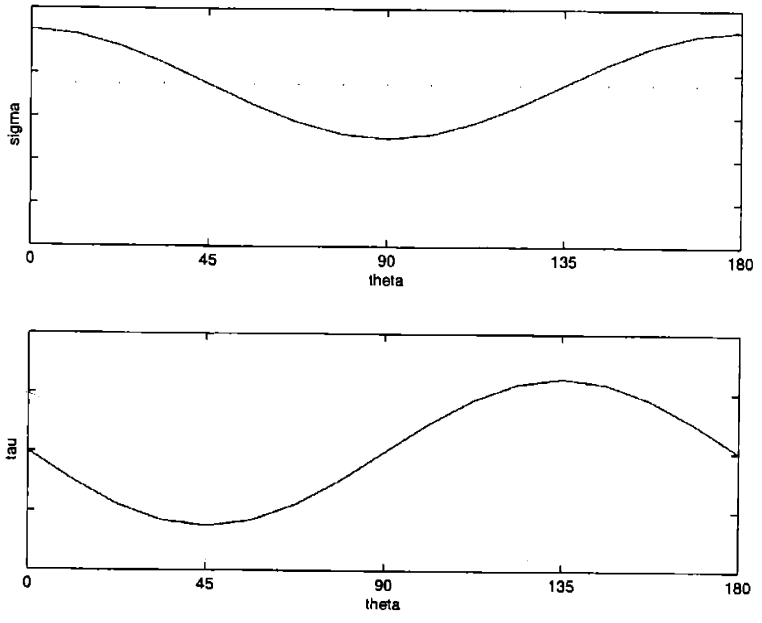

Figure A-3: Variation of σ and τ with θ.

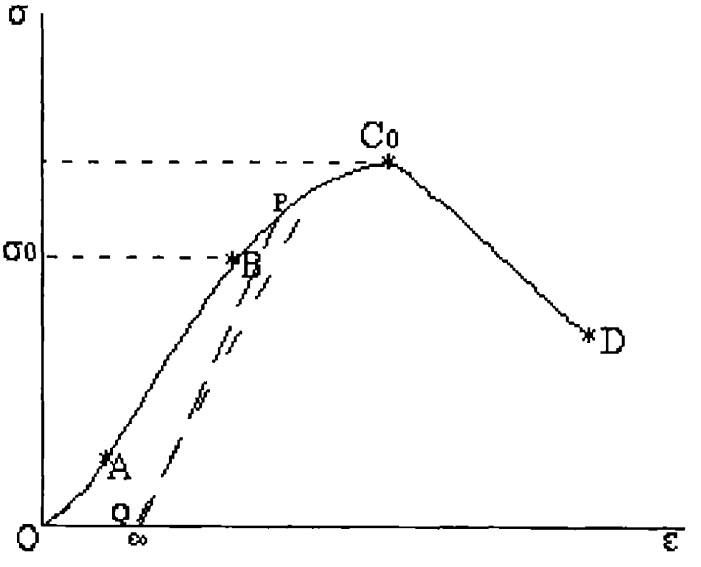

Figure A-4: Idealized stress-strain curve. C_0, the compressive strength, marks the beggining of failure. The yield stress σ_0 corresponds to the point where transition from elastic to ductile behaviour takes place. The dashed line PQ is an example of an unloading trajectory that does not return the material to zero strain (hysteresis), however, if another cycle of loading is started, the curve will ultimately join the original one. This indicates that the material preserves its ability to resist load.

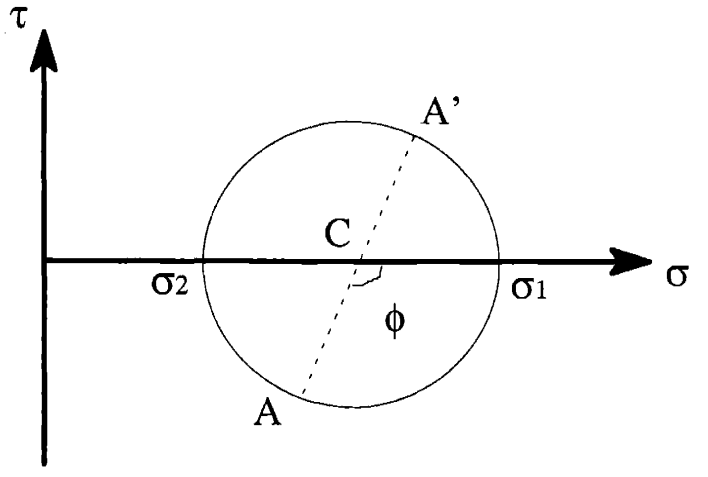

Figure A-5: Mohr's circle.

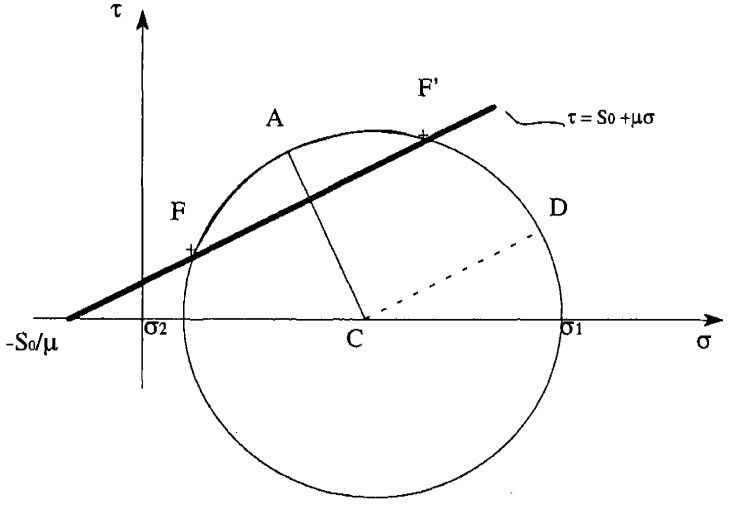

Figure A-6: Graphical description of sliding conditions.

Bibliography

Anderson, E. M. (1951). *The Dynamics of Faulting and Dyke Formation with Applications to Britain.* Ed. Oliver and Boyd, Edimburgh, 2nd edition.

Babcock, E. A. (1978). Measurement of Subsurface Fractures from Dipmeter Logs. *AAPG Bulletin*, 62(7).

Block, L. V., Cheng, C. H., and Duckworth, G. L. (1991). Velocity Analysis of Multireceiver Full-Waveform Acoustic Logging Data in Open and Cased Holes. *The Log Analyst*, pages 188–200.

Bouchon, M. and Schmitt, D. P. (1989). Full-Wave Acoustic Logging in an Irregular Borehole. *Geophysics*, 54(6):758–765.

Burns, D. R., Cheng, C. H., Schmitt, D. P., and Toksöz, M. N. (1988). Permeability Estimation from Full Waveform Acoustic Logging Data. *The Log Analyst*, pages 112–122.

Charlez, P. A. and Onaisi, A. (2001). Wellbore Stability: One of the Most Important Engineering Challenges when Drilling Smart Wells. In Lecourtier, J., editor, *Interactive Drilling for fast track Oilfield Development*, pages 77–102. TECHNIP, Rueil-Mailmaison, France.

Cheng, C. H. and Johnston, D. H. (1981). Dynamic and Static Moduli. *Geophysical Research Letters*, 8(1):39–42.

Cheng, C. H. and Toksöz, M. N. (1981). Elastic Wave Propagation in a Fluid-filled Borehole and Synthetic Acoustics Logs. *Geophysics*, 46(7):1042–1053.

Cheng, C. H., Toksöz, M. N., and Willis, M. E. (1982). Determination of In Situ Attenuation from Full Waveform Acoustic Logs. *Journal of Geophysical Research*, 87(B7):5477–5484.

Coates, G. R. and Denoo, S. (1981). Mechanical Properties Program using Borehole Analysis and Mohr's Circle. *SPWLA 22nd. Annual Logging Symposium*, pages DD 1– 16.

Cox, J. W. (1983). Long-axis Orientation in Elongated Boreholes and its Correlation with Rock Stress Data. In *24th Annual Logging Symposium*, page J, Calgary. Soc. of Prof. Well Log. Anal.

Eissa, E. A. and Kazi, A. (1988). Relation between Static and Dynamic Young's Moduli of Rocks. *International Journal of Rock Mineral Science and Geomechanical abstracts*, 25(6):479–482.

Ellefsen, K. J. (1990). *Elastic Wave Propagation Along a Borehole in an Anisotropic Medium.* PhD thesis, Massachusetts Institute of Technology.

Fjaer, E. (1999). Static and Dynamic Moduli of Weak Sandstones. *Rock Mechanics for Industry*, pages 675–681.

Frederick, J., Deitrick, G., Arguello, J., and de Rouffignac, E. (1988). Reservoir Compaction, Surface Subsidence and Casing Damage: a Geomechanics Approach to Mitigation and Reservoir Management. *SPE/ISRM EUROCK*, (47284).

Gardner, G. H. F., Gardner, L. W., and Gregory, A. R. (1974). Formation Velocity and Density- The Diagnostic Basics for Stratigraphic Traps. *Geophysics*, 39(6):770–780.

Gough, D. I. and Bell, J. S. (1982). Stress Orientation from Borehole Wall Fractures with Examples from Colorado, East Texas, and Northern Canada. *Canadian Journal of Earth Sciences*, 19:1358–1370.

Hearst, J. R., Nelson, P. H., and Paillet, F. L. (2000). *Well Logging for Physical Properties.* John Wiley and Sons, Ltd, second edition.

Jaeger, J. C. and Cook, N. G. (1979). *Fundamentals of Rock Mechanics.* Chapman and Hall, London.

Jizba, D. L. (1991). *Mechanical and Acoustical Properties of Sandstones and Shales.* PhD thesis, Stanford University.

Kimball, C. V. (1998). Shear Slowness Measurement by Dispersive Processing of the Borehole Flexural Mode. *Geophysics*, 63(2):337–344.

Kimball, C. V. and Marzetta, T. L. (1984). Semblance Processing of Borehole Acoustic Array Data. *Geophysics*, 49(3):274–281.

Landau, L. D. and Lifshitz, E. M. (1986). *Theory of Elasticity.* Pergamon Press, 3rd. edition.

Last, N. C. (2001). Achieving and Maintaining Improved Drilling Performance in the Tectonically Stressed Andean Foothills of Colombia. In Lecourtier, J., editor, *Interactive Drilling for fast track Oilfield Development*, pages 59–75. TECHNIP, Rueil-Mailmaison, France.

Malvern, L. E. (1969). *Introduction to the Mechanincs of a Continuous Medium.* Prentice-Hall.

Nicoletis, L. M., Bamberger, A., Quiblier, J. A., Joly, P., and Kern, M. (1990). Hole Geometry and Anisotropic Effects on Tube-wave Propagation: A quasi-static study. *Geophysics*, 55(2):167–175.

Nolte, B., Rao, R., and Huang, X. (1997). Dispersion Analysis of Split Flexural Waves. pages 12.1–12.25. Borehole Acoustics and Logging and Reservoir Delineation Consortia, Earth Resources Laboratory, MIT.

Paillet, F. L. and Cheng, C. H. (1991). *Acoustic Waves in Boreholes.* CRC Press, Inc.

Plumb, R. A. and Hickman, S. H. (1985). Stress-Induced Borehole Elongation: A Comparison Between the Four-Arm Dipmeter and the Borehole Televiewer in the Auburn Geothermal Well. *Journal of Geophysical Research*, 90(B7):5513–5521.

Randall, C. J. (1991). Modes of Noncircular Fluid-filled Boreholes in Elastic Formations. *Journal of Acoustical Society of America*, 89(3):1002–1016.

Report: PEP Macal- Estratigrafía (2001). Proyecto Macal: Estratigrafía. Technical report, Petróleos de Venezuela (PDVSA Exploración).

Report: PEP Macal- Geología Structural (2001). Proyecto Macal: Geología Estructural. Technical report, Petróleos de Venezuela (PDVSA Exploración).

Ruiz, F. and Graterol, J. (2002). Geomecánica y Estabilidad de Hoyo. Proyecto PEP Macal-1X. Technical report, Petróleos de Venezuela (PDVSA Exploración).

Schlumberger (2002a). *Log Interpretation Charts.* OilField Services Reference Publications.

Schlumberger (2002b). *Log Interpretation Principles/Applications: Geologic Services.* OilField Services Reference Publications.

Schlumberger (2002c). *Log Interpretation Principles/Applications: Mechanical Properties of Rocks.* OilField Services Reference Publications.

Schlumberger (2002d). *Log Interpretation Principles/Applications: Porosity Logs.* OilField Services Reference Publications.

Schlumberger (2002e). *Log Interpretation Principles/Applications: Spontaneous Potential and Natural Gamma Ray Logs.* OilField Services Reference Publications.

Serra, O. (1984a). *Fundamentals of Well-Log Interpretation*, volume 1. the adquisition of logging data of *Developments in Petroleum Science, 15A.* Elsevier Science Publishers B.V., New York.

Serra, O. (1984b). *Fundamentals of Well-Log Interpretation*, volume 2. the interpretation of logging data of *Developments in Petroleum Science, 15A*. Elsevier Science Publishers B.V., New York.

Simmons, G. and Brace, W. F. (1965). Comparison of Static and Dynamic Measurements of Compressibility of Rocks. *Journal of Geophysical Research*, 70:5649–5656.

Tang, X. M., Cheng, N. Y., and Cheng, A. C. H. (1999). Formation Stress Determination from Borehole Acoustic Logging: A theoretical foundation. *69th Ann. Internat. Mtg., Soc. Expl. Geophys., Expanded Abstracts.*

Tare, U. A. and Mody, F. K. (2002). Managing Borehole Stability. *HART's E & P.*, pages 8–11.

Toksöz, M. N. and Cheng, C. H. (1991). Wave Propagation in a Borehole. In *Shear Waves in Marine Sediments*. Kluwer Academic Publishers.

van Heerden, W. L. (1987). General Relations between Static and Dynamic Moduli of Rocks. *International Journal of Rock Mineral Science and Geomechanical abstracts*, 24(6):381–385.

Wang, Z. (2000). Dynamic versus Static Elastic Properties of Reservoir Rocks. In Nur, A., editor, *Seismic and Acoustic Velocities in Reservoir Rocks*, volume 3 of *Recent Developments Geophysics Reprint 19*, pages 531–539. SEG.

Yale, D. P. and Jamieson, W. H. (1994). Static and Dynamic Mechanical Properties of Carbonates. *Rock Mechanics*, pages 463–471.

Zemanek, J., Williams, D. M., and Schmitt, D. P. (1991). Shear-Wave Logging using Multipole Sources. *The Log Analyst*, pages 233–240.

Zoback, M. (2001). Reservoir Geomechanics. Course Notes. Stanford University.

Zoback, M. D., Daniel, M., and Mastin, L. (1985). Well Bore Breakouts and In Situ Stress. *Journal of Geophysical Research*, 90(B7):5523–5530.

Zoback, M. D., Mastin, L., and Barton, C. (1986). In-Situ Stress Measurements in Deep Boreholes using Hydraulic Fracturing, Wellbore Breakouts, and Stoneley Wave Polarization. In *Proceedings of the International Symposium on Rock Stress and Rock Stress Measurements*, pages 289–299, Stockholm.

Zoback, M. D. and Zoback, M. L. (1989). Stress in the Earth's Lithosphere. In Fairbridge, R., editor, *Encyclopedia of Earth Sciences Series*, pages 1221–1232. Van Nostrand Reinhold Co., New York.